Viscous and frictional strength of the lithospheric mantle : microstructural characterization of experimentally deformed polycrystalline Olivine

Manuel Thieme

THÈSE POUR OBTENIR LE GRADE DE DOCTEUR DE L'UNIVERSITÉ DE MONTPELLIER

En Géosciences

École doctorale GAIA

Unité de recherche UMR 5243

Viscous and frictional strength of the lithospheric mantle: Microstructural characterization of experimentally deformed polycrystalline Olivine

Présentée par Manuel THIEME
Le 08 novembre 2018

Sous la direction de Dr. Sylvie Demouchy et Dr. David Mainprice

Devant le jury composé de

Stéphane MAZZOTTI, Professeur, Géosciences Montpellier, Université de Montpellier	Président du jury
Whitney BEHR, Professor, Geological Institute, ETH Zürich	Rapportrice
Anne DAVAILLE, DR CNRS, Laboratoire FAST, Université Paris-Sud	Examinatrice
Sylvie DEMOUCHY, CR CNRS HDR, Géosciences Montpellier, Université de Montpellier	Directrice de thése
Alexandre DIMANOV, CR CNRS HDR, Lab. Mécanique des Solides, Mines ParisTech	Rapporteur
David MAINPRICE, DR CNRS, Géosciences Montpellier, Université de Montpellier	Co-directeur de thése
Maurine MONTAGNAT-RENTIER, DR CNRS, IGE, Université-Grenoble-Alpes	Examinatrice

UNIVERSITÉ DE MONTPELLIER

πάντα ῥεῖ - Everything flows.

Heraclitus of Ephesus/Platon/Simplikios

Context

The results detailed in this thesis were obtained as part of the innovative training network (ITN) complex rheologies in earth dynamics and industrial processes (CREEP, Horizon 2020, Marie Sklodowska-Curie grant agreement No. 642029). The CREEP network is a coherent platform for training and career development in Geodynamics, Mineral Physics, Seismology, Fluid Mechanics and Materials Sciences, bringing together scientists from 10 academic centers and 11 industrial partners in Europe. CREEP aims to advance our understanding of the complex rheology of Earth and industrial materials, including seismicity (induced or natural), production of fossil or renewable energy and rheology of industrial materials like glass. To this end, CREEP uses a fully multidisciplinary approach including mineral physics, petrology, seismology and geodynamics, spanning the large range of scales from the atomistic processes in crystals to global mantle dynamics. The main aim of ITN CREEP is to train 16 early stage researchers in state-of-the-art concepts and research techniques, while providing networking opportunities and courses and workshops on career-management skills. Finally, the impact and international visibility of European research is strengthened by communicating results to the public and facilitating exchange between the involved partners.

Deformation experiments for Chapter V (shear deformation of nano- and micro-crystalline olivine at seismic slip rates) were performed as part of my academic secondment with the Rock Mechanics Laboratory, Durham University, UK. I additionally spent a one-month internship at the Montpellier Technology Center (Schlumberger; https://www.slb.com/about/rd/technology/mptc.aspx) in colloboration with Frantz & Laurent Maerten as my industrial secondment.

Annex A contains the abstract of *Effect of pressure and temperature on viscosity of N-BK7 glass*, of which I am co-author. Experiments for this paper were performed in Montpellier in collaboration with the Institute of Geosciences, University of Mainz, as part of the CREEP network.

Acknowledgements

I thank my supervisors Sylvie Demouchy and David Mainprice for their insights, patience, support, and little tips and tricks. I am especially grateful to Sylvie for her determination and Zen-approach during long evenings in the lab. I believe it was the methodological problem solving, the tons of chocolate and the tea and maybe the little golden Ganesha that kept the deformation apparatus in check. Likewise, I want to thank the CREEP network, in particular Andrea Tommasi and Alida Lefter for providing me with countless opportunities to broaden my scientific horizon and develop new skills and methods, building a strong base for my future career. This included incentives and time for scientific outreach, internships, workshops and short courses.

I thank the Jury for accepting to review and judge this study.

I am grateful to Fabrice Barou, Nicolas Marino, Christophe Nevado and Dorianne Delmas for their help and tips during sample preparation and EBSD analysis. Nicolas, thank you for making me speak french and showing/teaching me some manual skills! Moreover, I thank Nicola DePaola for enabling me to perform my internship at the Rock Mechanics Laboratory, University of Durham and Giacomo Pozzi for his contribution to the experiments there and for being a perfect host. I want to express my gratitute to Frantz and Laurent Maerten for the opportunity of an internship at the Montpellier Technology Center (Schlumberger). I thoroughly enjoyed the contacts and connections I made there, the insights into industry work flows and live and the shared lunches ending in a few surprising opportunities.

I am deeply grateful for Alida Lefters support with administration during my first year in France. You made my arrival so much more smooth and effortless and showed me corners of Montpellier I would not have found by myself.

In no particular order I would like to thank Jose Alberto Padrón-Navarta, Catherine Thoraval, Anne Delplanque, Hélène Ournat and Marie Deguillon, for fruitful conversations and diverse help.

Last but certainly not the least I want to thank my family and friends who tolerated and supported me during this time and occasionally helped me to distract me from the science and bring me back down to earth. It would have been quite something else without you. You know who you are, you are the best!

Résumé en français

La déformation est un processus fondamental pour la dynamique des planètes tellurique, en particulier la tectonique des plaques sur Terre. Elle façonne la topographie actuelle, elle genère la formation de gisements de ressources ou elle est responsable des séismes superficiels et profonds. La cinématique et la géométrie de la tectonique des plaques sont directement liées à des forces motrices profondes contrôlées par le refroidissement de la Terre et par à la convection du manteau, avec en surface la formation de dorsales océaniques, de zones de subduction et de déformations localisées à l'interface entre la croûte et le manteau supérieur.

Le manteau supérieur est divisé en manteau lithosphérique solide et sous celui-ci le manteau asthénosphérique, plus chaud et donc moins visqueux. Le manteau lithosphérique est une couche de couplage partiel entre la base des plaques tectoniques rigides et l'asthénosphère convective sous-jacente. Les propriétés physiques de cette couche et l'amplitude du contraste de viscosité entres la lithosphère et l'asthénosphère, sont encore un sujet discussion en géodynamique. Entre 300 et 500 °C, les mécanismes de déformation dominants passent progressivement du glissement cassant dans les failles à du frottement, puis à des mécanismes ductiles (par exemple glissement de dislocation, processus aux joints de grains ou encore maclage). C'est la transition dite fragile-ductile. La composition chimique et minéralogique des roches va aussi concourir à la résistance aux déformations cisaillantes.

Nous avons choisi d'étudier la transition fragile-ductile par une approche expérimentale. Puisque les expériences de déformation en laboratoire sont de durée limitée, nous avons besoin d'une compréhension physique précise des mécanismes impliqués lors de la déformation permanente, cassante et ductile pour pouvoir extrapoler les résultats aux échelles de temps et d'espace caractéristiques de la Terre. La modélisation atomistique reste encore trop coûteuse en calcul pour modéliser une roche polycristalline et polyminérale dans toute sa complexité. À l'heure actuelle, l'approche la plus directe pour comprendre les mécanismes de déformation consiste à examiner les textures des roches et les niveaux de contraintes et leurs corrélations avec les données mécaniques enregistrées en laboratoire lors

d'essais mécaniques (contraintes, déformations finies, vitesses de déformation à une température et une pression données). Une fois les processus de déformation identifiés, ils peuvent ensuite être implémentés via des règles de comportement dans des modèles numériques d'interactions de dislocations et autres défauts cristallins pour pouvoir changer d'échelle de vitesse de déformation (10^{-5} s^{-1} au laboratoire, 10^{-14} s^{-1} dans la manteau).

Cette thèse a été réalisée dans le cadre d'un projet européen 'CREEP' (Marie Sklodowska-Curie Grant agreement No. 642029) dédié à la compréhension des rhéologies complexes des matériaux (géologiques ou non, http://www.creep-itn.eu). Les objectifs principaux étaient: (1) étudier la déformation de l'olivine polycristalline à des conditions pertinentes pour le manteau sommital, et donc à la transition fragile-ductile ; (2) étudier l'évolution des microstructures et des textures en fonction de la déformation finie pour ces déformations en régimes transitoires – c'est à dire, avant d'atteindre l'équilibre mécanique ; (3) évaluer l'influence des défauts cristallins de rotation (disclinaisons) sur l'écrouissage de l'olivine polycristalline, et enfin (4) étudier les mécanismes impliqués dans l'affaiblissement du coefficient de friction à des vitesses de glissement sismiques.

Suite à l'introduction et à la présentation des principales méthodes expérimentales et analytiques utilisées, le manuscrit est ensuite organisé en trois chapitres correspondant à trois articles scientifiques (un publié chez 'Physics of the Earth and Planetary Interiors', et deux en préparation), et se termine par une conclusion générale avec perspectives. Nous donnons ci-dessous une synthèse des trois études réalisées.

Déformation plastique de l'olivine polycristalline à haute température: Nous avons étudié la réponse mécanique et les microstructures associées des agrégats d'olivine à grains fins déformés en compression axiale, à des taux de déformation finie incrémentiels. Au total 10 expériences de déformation ont été effectuées avec une Presse Paterson à Géosciences Montpellier, à des températures de 1000 et 1200 °C (chauffage interne) et une pression de confinement gazeuse de 300 MPa (argon). La vitesse de déformation est quasi constante avec des valeurs entre 10^{-6} s^{-1} à 10^{-5} s^{-1}. Le volume des échantillons est d'environ 1,2 cm^3 après le frittage à froid de poudre d'olivine de San Carlos (taille de grain 1-2 microns). Les déformations finies vont de 0,1 à 8,6 % et les contraintes différentielles maximales (finales) correspondantes vont de 80 jusqu'à 1073 MPa pour les expériences de déformation à 1000 °C et de 71 jusqu'à 322 MPa pour les expériences de déformation à 1200 °C.

A 1200 °C, les échantillons se rapprochent de la déformation plastique à l'état stationnaire après environ 8 % de déformation finie. À 1000 °C, un écrouissage important entraîne des contraintes supérieures d'un facteur 3,5 à la pression de confinement après 3% de déformation finie. Les échantillons déformés ont ensuite été caractérisés par diffraction aux électrons rétrodiffusés (EBSD) et microscopie électronique en transmission (MET). Pour la première fois des cartes EBSD avec des pas de mesure de 0.06 □m ont été acquises sur l'olivine polycristaline sans introduire d'artefacts analytiques. La taille des grains moyenne des échantillons déformés varie de 2,1 à 2,6 µm. Malgré un durcissement mécanique important, la texture ou la microstructure ne changent pas en fonction du niveau de contrainte ou de déformation finie. Cette observation est appuyée par l'orientation préférentielle de réseaux de l'olivine avec des indices de texture 'J' quasi constants et une symétrie (indice de texture 'BA') faible, un rapport d'aspect constants des grains, une densité constante des dislocations géométriquement nécessaires (GND en anglais), et des niveaux de désorientations intragranulaire faibles. L'imagerie par MET montre que tous les échantillons présentent des dislocations actives, distribuées de manière très hétérogène de grain à grain. Les grains d'olivine présentent des glissements selon les directions [100] et [001], mais il n'y a aucune preuve d'interactions entre les dislocations des différents systèmes de glissement (pas de 'cross-slip'). Certains joints de grains agissant comme des sources de dislocations (e.g., source de type Frank-Read) ont été observés, mais nous ne trouvons aucune confirmation de l'augmentation des densités de dislocation (i.e., 'la forêt') comme cause du durcissement lors du fluage transitoire. Cela suggère donc qu'il y a d'autres mécanismes affectant la résistance de l'olivine. Ces mécanismes pourraient éventuellement impliquer des joints de grains, par glissement ou migration. De tels mécanismes seraient pertinents pour la déformation des roches du manteau supérieur, où les processus de restauration (i.e., diffusion ionique du silicium) sont trop lents aux températures du manteau sommital et où le glissement de dislocations doit donc être compensé d'une manière ou d'une autre pour satisfaire les critères de von Mises (e.g., olivine paradoxe).

Défauts rotationnels (disclinaisons) dans l'olivine polycristalline : Les échantillons produits dans le premier projet ont fait l'objet d'une étude plus poussée sur les défauts rotationnels en utilisant le logiciel ATOM dans un premier temps, puis ATEX (collaboration avec Benoit Beausir, LEM3, METZ). Ce logiciel permet d'obtenir des valeurs quantitatives pour les densités de dislocations et disclinaison, que qui n'est pas encore possible avec le

logiciel MTEX (plus largement utilisé dans la communauté). Les premiers traitements des cartes EBSD montrent que plus le pas de mesure est petit, plus la densité de disclinaisons calculée augmente, les cartes ont donc été traitées avec un pas de mesure constant de 0.1 □m. Les résultats n'ont pas révélé de corrélation (positive ou négative) entre densité de dislocations GND et densité de disclinaisons, entre densité de disclinaisons et contraintes différentielles (ou température), ou entre densité de disclinaisons et déformation finie. Quoi qu'il en soit, la présence de défauts rotationnels est avérée le long de joints de grains, sous forme de dipôle, ou de disclinaison isolée, et ce dans la totalité des cartes EBSD étudiées, mais nous n'observons pas de disclinaisons le long des sous-joints formés par les GND.

Déformation de l'olivine polycristalline à des vitesses de déformation typiques des séismes (collaboration ITN 'CREEP' avec N. De Paola et G. Pozzi, Université de Durham, UK): La réduction du coefficient de friction des roches lors de glissements sismiques (~ 1 ms^{-1}) est un paramètre primordial contrôlant la mécanique des séismes via la quantité de glissement, la géométrie des failles, l'énergie sismique relâchée et le flux thermique le long des failles. Plusieurs mécanismes ont été proposé pour expliquer la diminution du coefficient de friction, par exemple : la fusion de la roche par frottement suite à un échauffement visqueux, la déstabilisation (thermique) de certaines phases minérales, des réactions quasi métamorphiques entres les phases minérales ou encore la présence de phases minérales de très faible viscosité (e.g., talc et autres produits d'altération).

Dans ce dernier projet, nous rapportons des données mécaniques et caractérisons des microstructures d'agrégats d'olivine déformés en torsion à des vitesses de glissement de 10^{-2} ms^{-1} à 1 ms^{-1}, à pression et température ambiante. Une contrainte axiales initiale de 20 MPa est appliquée à l'échantillon. Deux types de poudre de forsterite ont été utilisés, l'une avec une taille de grain de 0,7 μm (nanoforsterite synthétique) et l'autre avec une taille de grain de 70 ± 2 μm (olivine de San Carlos ou de San Bernadino). Un total de 33 expériences ont été effectuées à l'université de Durham, avec un appareil de déformation en torsion (e.g., rotary shear frictional testing machine, Model MIS-233-1-77). Les échantillons récupérés ont été caractérisés par microscopie électronique à balayage (MEB) et diffraction aux électrons rétrodiffusés (EBSD). Les coefficients de friction diminuent indépendamment de la taille de grains ou de la composition chimique, avec des valeurs allant de 0.6-0.55 à 0,4-0,1 après seulement 0,1 m de glissement total. La déformation permanente à lieu à la fois par écoulement cataclastique et par fluage de dislocation. L'écoulement cataclastique entraîne une

réduction rapide de la taille des grains et déclenche une localisation de la déformation par cisaillement à proximité de la zone d'échantillonnage où la contrainte était la plus élevée. Bien que le mécanisme de déformation dominant semble être l'affaiblissement par augmentation de la température, nous ne trouvons aucun signe de fusion par frottement ou décomposition thermique. Les résultats de cette étude confirment donc les résultats mécaniques précédemment obtenus sur d'autres types de roches (e.g., quartzite, peridotites, serpentinites, gabbros, dolomites, argiles) avec la même approche expérimentale. Ces nouveaux résultats confirment également l'effet négligeable de la taille de grains et de la composition chimique et minérale sur la réduction drastique du coefficient de friction. Par contre, nos expériences n'ont pas permis de proposer un modèle physique responsable de l'affaiblissement drastique du coefficient de friction.

En conclusion, cette thèse a permis de mieux caractériser la transition fragile-ductile d'une roche de type dunite à grains fins, soumise à une déformation permanente aux températures du manteau sommital. Le premier projet a permis de montrer que le durcissement mécanique ne peut pas provenir d'une simple augmentation de densité de dislocation et que d'autres mécanismes doivent compenser les limitations dues aux glissements et aux montées des dislocations. Pour la première fois, les densités de GND et de disclinaisons sont quantifiées sur une série de roches déformées à différentes températures, déformations finies et niveaux de contraintes, mais aucune corrélation n'a été identifiée. Le Le rôle des disclinaisons se limiterai donc à de la migration aux joint de grain, qui pourrait être suffisante pour débloquer le glissement de certaines dislocations dans l'agrégat polycristallin d'olivine. Les expériences de déformation en torsion rapide ont confirmé l'effet négligeable de la taille de grain (olivine de 0.7 à 70 μm) sur la diminution drastique du coefficient de friction, mais la caractérisation des échantillons n'a pas permit d'élucider le mécanisme physique qui en est responsable. Les résultats de cette thèse lancent des nouveaux challenges expérimentaux et analytiques, comme l'analyse de poudres fines faiblement compactées en EBSD, la réalisation d'expériences de déformation sur des durées plus longues pour que les processus de restauration puissent modifier la microstructure des roches à grains fins, même à des températures du manteau sommital, ou encore le rôle des disclinaisons sur la déformation finie d'un agrégat polycristallin d'olivine.

Glossary

EBSD – Electron backscatter diffraction.

SEM – Scanning electron microscopy.

TEM – Transmission electron microscopy.

LHVS – Low to high velocity rotary shear apparatus.

Elastic deformation – Time independent and fully recoverable.

Anelastic deformation – Time dependent recoverable.

Viscous deformation – Time dependent irrecoverable.

Brittle deformation – Irreversible and loss of cohesion.

Ductile deformation – Without loss of cohesion, sum of elastic, anelastic and viscous deformation, requires no yield stress.

Plastic deformation – Time independent irrecoverable, requires a yield stress, loss of cohesion not necessary.

Microstructure – The grain and sub-grain scale structure of a prepared sample surface revealed by a microscopic method.

Chapter I – Introduction

This chapter presents a short introduction to the rheology of the uppermost mantle and the state of the art of experimental deformation of olivine.

I-1 Rheology of the Crust and upper Mantle

The term rheology was coined in 1929 by E.C. Bingham and Markus Reiner as the "study of the flow and deformation of all forms of matter" (Reiner 1964). While rheology is especially concerned with fluids, it equally deals with the flow of rock forming, crystalline solids – how they react to an imposed stress in terms of deformation (strain) rate. As such, rheology is fundamental to planetary dynamics, notably plate tectonics. Plate tectonics has a direct impact on humans, by forming the current topography, aiding in resource deposit formation or directly expressed as earthquakes. The kinematics and geometry of plate tectonics are directly related to its driving forces, mantle convection, ridge push and slab pull, and therefore to the rheology of both the mantle and the crust.

The upper mantle of the Earth is divided into the upper mostly rigid lithospheric mantle and the ductile asthenosphere. The lithospheric mantle forms an important interface layer between the rigid tectonic plates and the convecting asthenosphere. Localized and often episodic deformation within plates is contrasted to a viscous flow in the asthenosphere. The interface properties and strength of the rheologic layers, especially at their boundary (i.e. lithosphere-asthenosphere boundary, Fischer et al., 2010), is still under discussion. Due to active faulting, the crust is thought to be in a frictional equilibrium. With increasing depth, the frictional strength of rocks increases (as a function of pressure), while simultaneously thermally activated processes become more active and reduce the viscous strength as a function of temperature and pressure (e.g., Brace & Kohlstedt 1980). In between temperatures of 300 to 500 °C (Bürgmann & Dresen 2008), the dominant deformation mechanisms gradually change from faulting and frictional sliding to ductile mechanisms (e.g. dislocation glide, grain boundary processes or twinning). This is the so-called brittle-ductile transition. Additionally, the mineral content of the rocks determines strength. Mafic rocks and rocks with a high melting temperature (T_m) have higher viscosities at a given temperature and pressure (e.g. Sharple 1914; Karato, 2012).

Classic strength profiles show a strong upper crust and even stronger mantle lithosphere enclosing a weak mid- to lower crust. In this case, the mantle lithosphere primarily influences the strength of tectonic plates. Chopra & Paterson (1984) and Mackwell et al. (1985) proposed that the lithospheric mantle is weakened by high temperature and water content, leading to a brittle crust governing the strength of the lithosphere. Zoback et al. (1987) argue

that thermal, fluid and strain rate weakening processes produce regional rheologic weaknesses at plate boundaries and mature fault zones, reducing the friction coefficient to below 0.2. An analogous weakening in ductile shear zones might be achieved by shear heating, grain-size reduction, dynamic recrystallization and phase- or chemistry changes (e.g. Tullis & Yund 1985; Kronenberg et al. 1990; Chester et al. 1993; Ruttner 1999; Hirose & Shimamoto 2005; De Bresser et al. 2000).

A strength envelope diagram is shown in Figure I-1, presenting the colloquially called "jelly sandwich" model (e.g. Burov & Watts 2006) with a strong upper and lower crust and strongly varying estimates for the strength of upper mantle rocks. The biggest discrepancy in flow laws for the upper mantle stems from extrapolating data obtained at high temperatures (≥ 1100 °C) or low temperature (≤ 1100 °C).

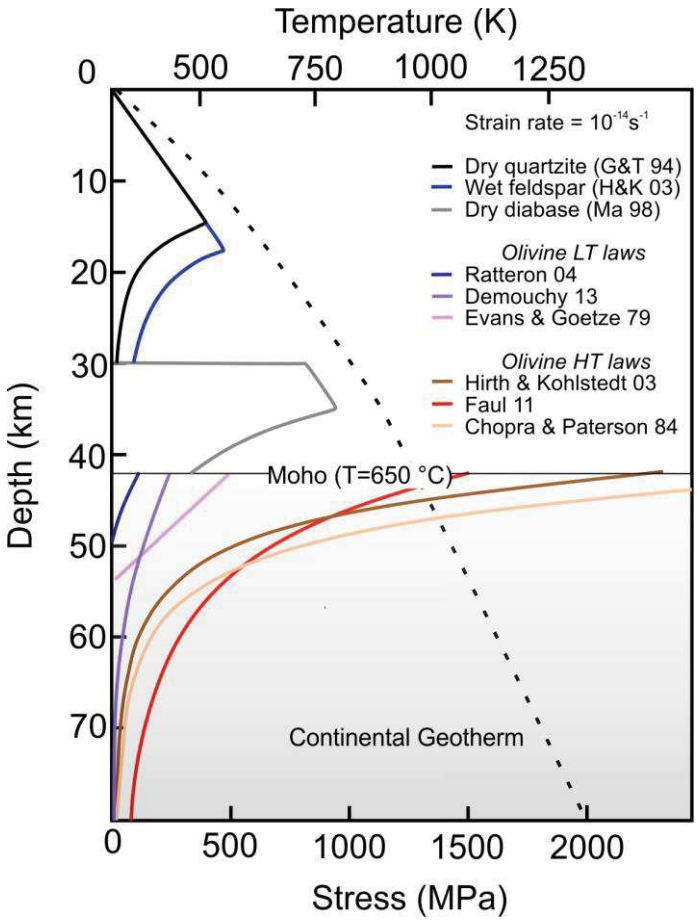

Fig. I.1 Strength envelope model for continental lithosphere and a strain rate of 10^{-14} s^{-1}. Solid lines show viscous strength of lithospheric and upper mantle rocks, the dashed line shows the continental geotherm. Flow laws are from Evans & Goetze (1979), Chopra & Paterson (1984), Gleason & Tullis

(1994), Mackwell (1998), Hirth & Kohlstedt (2003), Ratteron et al. (2004), Faul et al. (2011) and Demouchy et al. (2013). All olivine flow laws are for dry olivine.

I-2 Olivine

Olivine is a solid solution series of magnesium-iron silicates with the endmembers forsterite (Mg_2SiO_4) and fayalite (Fe_2SiO_4) and the general formula $(M1,M2)_2SiO_4$. Olivine is classified as orthosilicate/nesosilicate crystallizing in the orthorhombic – dipyramidal space group Pbnm (Deer et al 1997). Table I.1 gives the cell dimensions, cell volume and calculated density for olivine endmembers and average mantle olivine.

Table I.1 Olivine end-member and average mantle olivine crystallography (data from Birle et al. 1968; Deer et al., 1997).

		Fayalite	Average mantle olivine	Forsterite
Formula		Fe_2SiO_4	$(Mg_{0.9}Fe_{0.1})_2SiO_4$	Mg_2SiO_4
Cell dimensions (Å)	a	4.82	4.76	4.75
	b	10.48	10.21	10.20
	c	6.09	8.96	5.98
Cell volume (Å^3)		290	309	290
Density (calc; gcm^{-3})		4.40	~ 3.4	3.22

The major element chemistry of olivine is often given as the percentage of magnesium or forsterite content (Fo_0 – Fo_{100}). Common minor elements are Mg^{2+}, Ni^{2+}, Mn^{2+}, Cr^{3+}, B^{3+} and Ti^{2+} (Frey & Prinz 1976; Sykes 1994; Deer 1997). The major element composition strongly influences the melting temperatures. While pure fayalite melts at ~ 1200 °C, pure forsterite melts at ~ 1900 °C under atmospheric pressure (Klein & Hurlburt 1985). Figure I-2 shows a projection of the olivine structure. Divalent metallic cations (M1, M2) are linked to independent SiO_4 tetrahedra. Each tetrahedron is bound to three metal ions. Alternatively, olivine can be described as a hexagonal, close-packed array of three distinct oxygen sites where 1/8 of the tedrahedral sited are occupied by Si ions and 1/2 of the octahedral sites are occupied by metal ions (Klein & Hurlburt 1985). Since the ionic radius of bivalent Mg is slightly larger than the one of Fe, Mg prefers the likewise larger M2 site (Shannon 1976). Yet, there is apparently no perfect ordering of metal ions between M1 and M2.

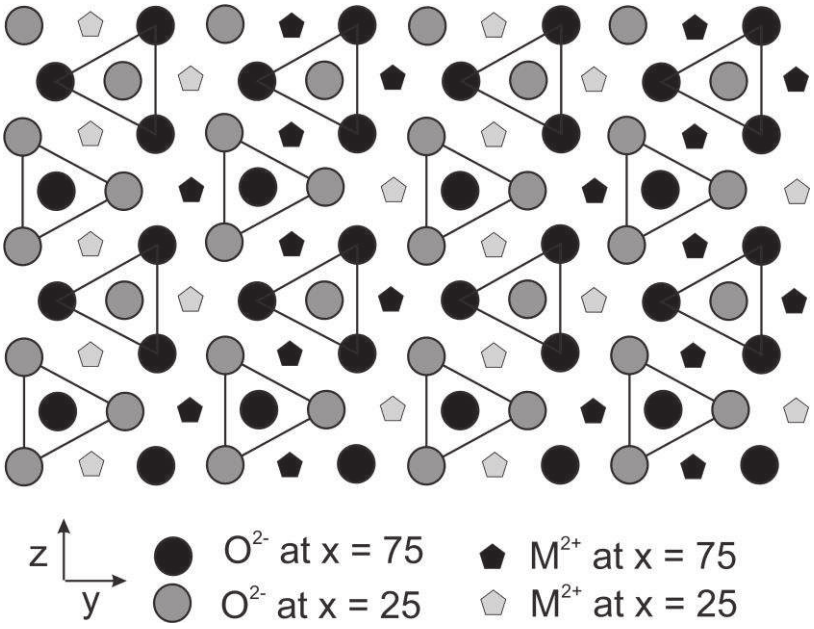

Fig. 1.2 Olivine structure projected along the [100] axis. Si atoms at the center of the oxygen tetrahedrons are not shown.

At depths of 410 km, olivine transforms into its high-pressure polymorph wadsleyite and following, at 520 km depth, to ringwoodite. Ringwoodite decomposes into perovskite Mg,Fe)SiO_3 and ferropericlase (Mg,Fe)O at about 660 km of depth. Olivine is stable at atmospheric pressures but weathers in the presence of meteoric water into iddingsite, a mixture of clay minerals, iron oxides and ferrihydrites with the formula $MgFe_2Si_3O_{10}\times4(H_2O)$ (Ross 1925; Gay & Maitre 1961) or serpentinite ($Mg_3Si_2O_5(OH)_4$).

I-3 Deformation of crystalline solids

As known, silicates are ionic crystals composed of ions arranged in an ordered crystal lattice (Ashcroft & Mermin, 1976). These lattices are never perfect in nature and always contain point defects (vacancies, interstitials, 1-dimensional defects) or line defects (dislocations, disclinations, sub-grain boundaries, 2-dimensional defects) or inclusion (fluid or solid, 3-dimensional defects). Point defects are always present, since the crystal entropy decreases nonlinearly with the addition of vacancies or self-interstitials (e.g., Nakamura & Schmalzried, 1983)). The enthalpy increases linearly, which results in the free energy (Gibbs energy) being minimized when a finite concentration of vacancies or self-interstitials is present (Devereux, 1983). The concentration of point defects in turn is determined by temperature, pressure through the Gibbs free energies of formation (Schmalzried, 1981), with the condition to maintain electroneutrality.

Apart from point defects, line defects are highly important for the deformation of geo-material under lower crustal and mantle conditions. Unlike point defects, they introduce a small change in entropy compared to the change in enthalpy. Hence, they should not exist under equilibrium conditions (Devereux, 1983). The most common type of line defects are dislocations, topological defects behaving as stable particles which can move while maintaining their identity (Taylor, 1934). Dislocation can be conceptualized as additional half-planes in the crystal lattice. Dislocations are described by the line vector L defining the direction of the dislocation line at each point along its length and the Burgers vector $\vec{b}$ that describes the magnitude and direction of the lattice distortion (Kittel, 1996). Figure I-3 shows a schematic of a dislocation with its Burgers and line vector.

While the Burgers vector is the same at every point, L changes alongside the dislocation and depending on the dislocation type. Regions where $\vec{b}$ and L are perpendicular are called edge segments and regions where b and L are parallel are called screw segments (Hirth & Lothe, 1992; Kohlstedt & Hansen, 2015). Additionally, mixed segments are possible. Dislocations can either glide perpendicular to their line vector in a certain lattice plane or climb by diffusion such that the dislocation line moves normal to its glide plane. The glide of an edge dislocation results in a displacement parallel to the direction of glide, while screw dislocations result in a displacement perpendicular to its direction of movement. The combination of a unit vector normal to the slip plane and the Burgers vector results in the slip system of a given dislocation (e.g. ([100](010), [100](001), [001](010) or [100](010),

[001](010) and [001](100) in Olivine; Hutchinson, 1977). Screw dislocations are not bound to a certain glide plane since $\vec{b}$ and L are parallel and can switch planes by cross-slip (Hirth & Kohlstedt, 2015).

Similarly, disclinations are rotational topological defects described by the line vector L and Frank vector W. Disclinations were first described by Friedel (1922; see also Frank, 1958) in liquid crystals, but thought to be too energetically costly to exist in crystalline solids (Loth and Hirth, page 4). Recent observations in copper and olivine propose that the arrangement of disclinations in dipoles might reduce the energy cost and investigate their participation in deformation (Beausir & Fressengeas, 2013; Cordier et al., 2014). An overview over possible defects and deformation mechanisms is given in Table I.2

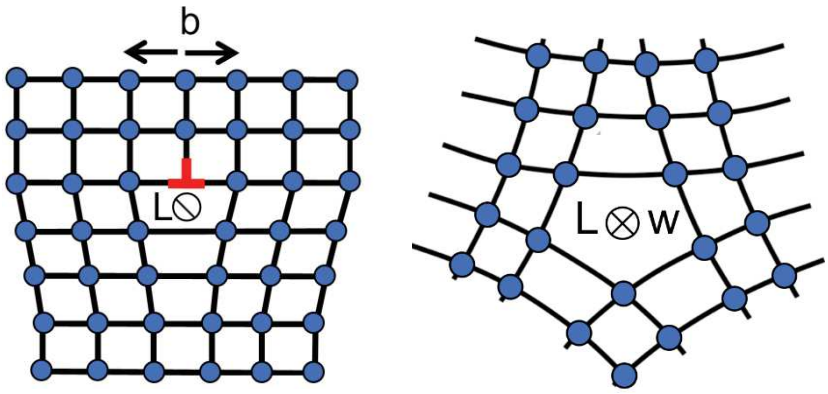

Fig. I.3 Atomistic model of a dislocation (left) and disclination (right). Blue circles represent lattice atoms. b is the Burgers vector, L the line vector and W the Frank vector.

Table I.2 Overview and classification of deformation mechanisms.

Deformation											
Elastic - Time independent recoverable	**Viscous** - Irreversible on short time scales or without externally applied stress - Very low or no threshold stress							**Brittle** - Irreversible, loss of cohesion - Requires threshold stress		**Chemical-Ductile** - Reversible on return to initial conditions
	0-D defects		**1-D defects**			**2-D mechanisms**		**Volumetric mechanisms at nanoscale**		
	Boundary diffusion (Coble Creep)	Bulk diffusion (Nabarro-Herring creep)	Dislocation glide (translation)	Dislocation climb (Harper Dorner creep)	Disclinations (rotation)	Grain boundary sliding	Twinning	Rigid body grain rotation	Cataclastic flow	Phase transformation

I-4 Aim of this Thesis

As outlined in section 1.1, the rheologic strength of upper mantle rocks and the degree of shear localization are still debated. Geodynamic models, seismic stress inversion and slip tendency analysis on natural fault zones (Nakagawa & Tackley, 2015; Crameri & Tackley, 2015; Crameri et al., 2012; Maerten et al., 2016a,b; Bolognesi & Bistacchi, 2018) require low coefficients of friction (≤ 0.2) and low viscosities to model earth like behaviors. Yet, sliding experiments at sub-seismic velocities with natural rocks have shown universal friction coefficients of 0.6 – 1.0 (Byerlee 1978) and strongly varying viscosities. In line with the uncertainty in viscosity of lower crust and upper mantle rocks, it is unclear if deep earthquakes are rooted in either distributed viscous flow or frictional aseismic faulting (Thatcher 1983; Tse & Rice 1986).

Many of those open questions can be attributed to a key problem of experimental rock deformation: the lowest strain rates achievable in the lab, while still allowing for sufficiently large strains and sample volumes, are in the order of 10^{-5} s^{-1} to 10^{-7} s^{-1}. In contrast, strain rates in the upper mantle are on the order of 10^{-15} s^{-1} (e.g. Nakada 1984). It remains disputed if apparently required low values of viscosity and friction are due to weakening mechanisms (melting, texture, water content) or due to problems in extrapolating flow laws over 10 orders of magnitude in strain rate (from commonly $10^{-5}s^{-1}$ in the lab to $10^{-15}s^{-1}$ in nature). In the past, attempts have been made to address this problem (e.g. by comparison of natural to laboratory textures and microstructures; Nicolas 1986; Nicolas & Poirier 1976; Gueguen & Nicolas 1980; Tommasi et al. 1999, 2016). Yet, there remain three major challenges: (1) Olivine can support stresses of almost 1 GPa at 1000 °C and strain rates of 10^{-5} s^{-1} (Demouchy et al., 2014). Deformation of olivine is therefore difficult to investigate at low temperatures (≤ 900 °C) without risking brittle failure of the sample (2) Previous experiments were commonly run to a common and fixed value of finite strain and fixed applied force (i.e., so called creep test) or until so called mechanical steady state, where stress becomes independent of finite strain. The early stages of deformation are therefore poorly understood. (3) The so called von Mises criterion (Mises, 1928; Hutchinson, 1977) states that in dislocation creep regime four independent dislocation slip systems must be active in the case of inhomogeneous flow (i.e., flow in polycrystals) to allow an arbitrary deformation. In olivine, there are only three independent slip systems ([100](010), [100](001), [001](010) or [100](010), [001](010), [001](100)). Therefore, dislocation creep cannot act alone and there must exist an additional - plastic - deformation mechanism.

Due to the limitations imposed by laboratory experiments, we need an accurate physical understanding of the mechanisms involved during permanent deformation. Atomistic modeling remains too computational intensive to model a full polycrystalline and polymineralic rock, since simulations would require >> than 10^{10} atoms (Sills et al. 2016). Although new modeling approaches promise to reduce computation time exponentially (discrete dislocation dynamics; e.g. Benzerga et al. 2004; Boioli 2015; Sills 2016), the most direct approach to better understand deformation mechanisms is to look at microstructures developed during deformation under known conditions and to correlate them with recorded mechanical data (stress, strain, strain-rate at a given temperature and pressure).

In the scope of this thesis, I have

(1) Investigated deformation of the most common upper mantle mineral olivine at conditions relevant for the uppermost lithospheric mantle.

(2) Studied the evolution of microstructures as a function of finite strain for so called transient deformation – before reaching mechanical steady state.

(3) Investigated mechanisms involved in frictional weakening at seismic slip rates.

(4) Assessed the influence of rotational topological defects (disclinations) on strain hardening and deformation in polycrystalline olivine.

Chapter II – Methods

This chapter gives an overview over the two deformation apparatus, explains how orientation and microstructural data were obtained and details the preparation steps necessary to obtain polished sections for analyses (electron backscatter diffraction and transmission electron microscopy).

II-1 Experimental Deformation

II-1.1 Deformation apparatus of Paterson

In the scope of this thesis, I used (1) an internally heated, gas pressure medium, in-situ deformation apparatus (later called *Paterson Press)* at Geosciences Montpellier, (University of Montpellier, France) and (2) a low to high velocity rotary shear apparatus (LHVS) at the Rock Mechanics Laboratory (University of Durham, UK) in the following, operating at room temperature and without a dedicated pressure medium.

An overview of deformation apparatus is given in Figure II-1. The Paterson Press routinely reaches maximum confining pressures of ~ 0.3 ± 0.002 MPa GPa, maximum differential stresses of ~ 1.5 ± 0.01 GPa and a maximum temperature of ~ 1250 ± 2 °C. These values are at the lower end compared to modern multi-anvil or diamond anvil cell presses. Yet, the use of a gas pressure medium allows for precise measurements of confining pressure (± 2 MPa) and the comparatively low differential stresses allow sample sizes of up to 1 cm³. The zone of constant temperature (hot-zone) extends over 20 mm and is calibrated to ± 2 °C.

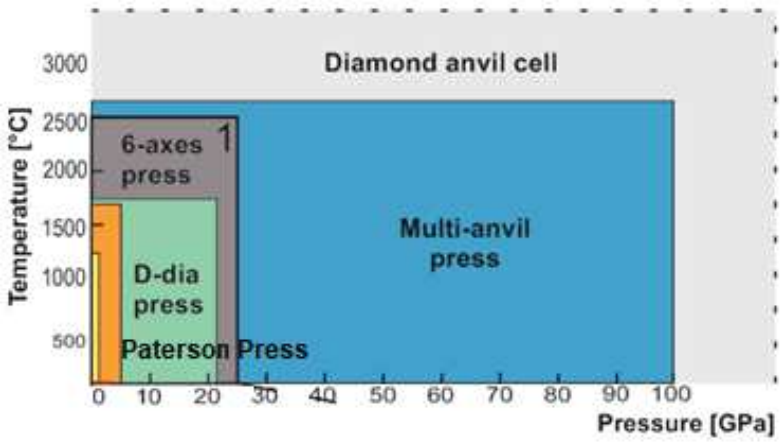

Fig. II-1 Overview of the pressure and temperature field of work for various high pressure, high temperature apparatus. The Paterson Press is in yellow on the left.

Chapter III investigates the deformation of polycrystalline olivine for application to the uppermost layer of the Earth's mantle, the lithospheric mantle. Pressures in this layer just below the Mohorovičić discontinuity typically range from 1 GPa to 3 GPa and temperatures from 500 °C to 1000 °C. Figure II-2 shows the average temperature and pressure path in the

crust and mantle as a function of depth. The red rectangle gives the temperature and pressure range achievable in the Paterson Press for deformation of olivine at strain rates of $10^{-5}s^{-1}$. The temperature during Paterson Press deformation is higher by 200 – 500 °C and the pressure is 1.2 GPa lower than in the uppermost mantle. Still, experiments in praxis have to be performed at temperatures ≥ 1000 °C to avoid brittle failure and hence alteration of the microstructure of the samples.

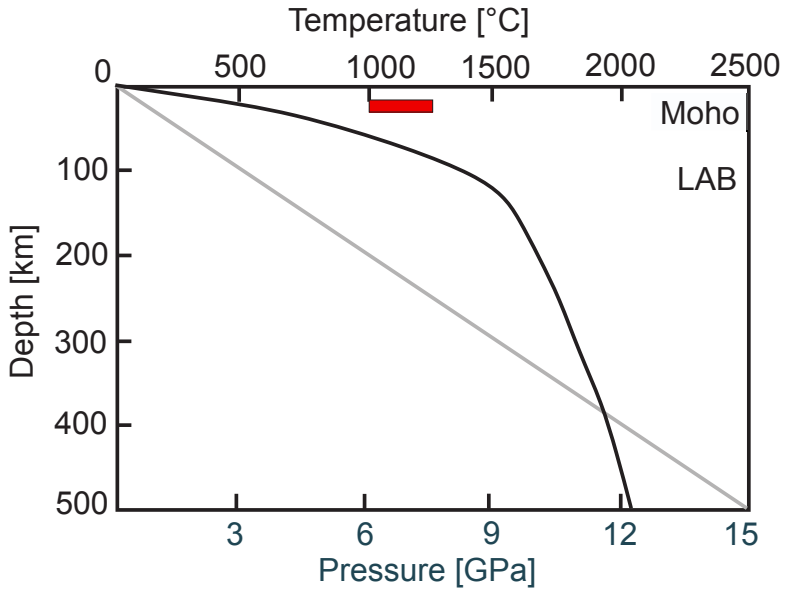

Fig. II-2 Temperature (black line) and pressure (grey line) curves for common crustal and mantle rocks. Areas shaded in grey show the position of the Mohorovičić discontinuity and Lithosphere-Asthenosphere boundary. The red rectangle shows conditions in the Paterson Press for deformation of olivine at strain rates of 10^{-5} s^{-1}. Geotherm after Earle (2016).

Figure II-3 shows a schematic drawing of the Paterson Press. The Paterson Press is a pressure vessel with a cental water-cooled system that surrounds an internal furnace. The furnace is a dense alumina tube isolated with alumina inserts and manually compacted with alumina fibres. Heating is achieved by three sets of molybdenum wires coiled around the top, center and bottom of the furnace. Argon fills the complete inside of the pressure vessel, including the furnace. Pressure is held by two O-rings, mitre rings on top of the pressure vessel and several O-rings on the bottom close to the internal load cell. Deformation is controlled by a hydraulic system driving a movable steel piston from the bottom. In Montpellier, only uniaxial compression can be performed, while with the right additions, the Paterson Press can also be used for torsion experiments (Paterson & Olgaard, 1990).

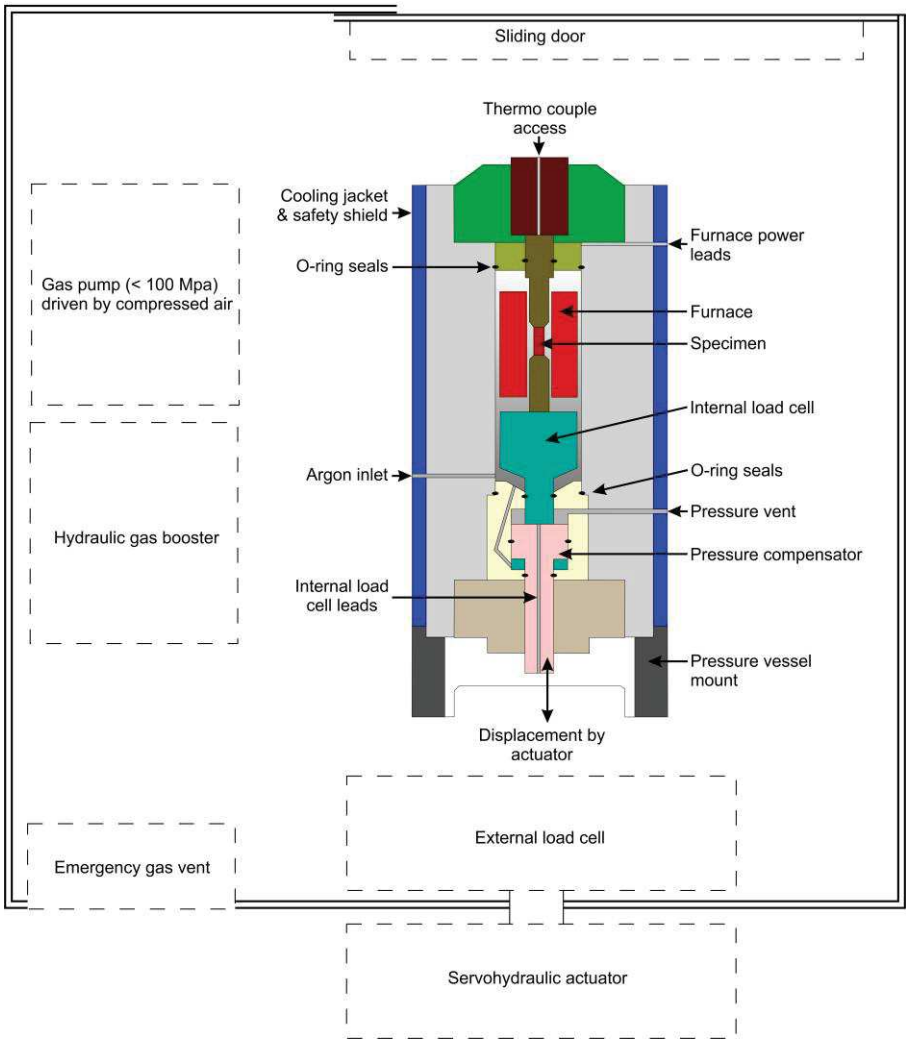

Fig. II-3 Schematic drawing of a Paterson Press deformation apparatus and peripheries.

The sample is surrounded by a Ni capsule as well as Ni discs and alumina and zirconia pistons on both ends. Tapered Alumina pistons and Zirconia pistons translate the force from the bottom steel pistons onto the sample while the top is fixed. Alumina is used close to the hot-zone due to its thermo-isolating properties and zirconia in contract to the steel pistons due to its higher hardness (truthful stress transmission) and resistance to chipping. The pistons and all top spacers (except the one in contact with the Ni capsule) have central holes to allow insertion of a thermocouple for temperature logging during experiments. The whole assembly of sample, Ni capsule, spacers and pistons is surrounded by a soft Fe jacket, which ensures pressure isolation towards the Argon pressure medium. An example of a typical sample assembly is given in Figure II-4.

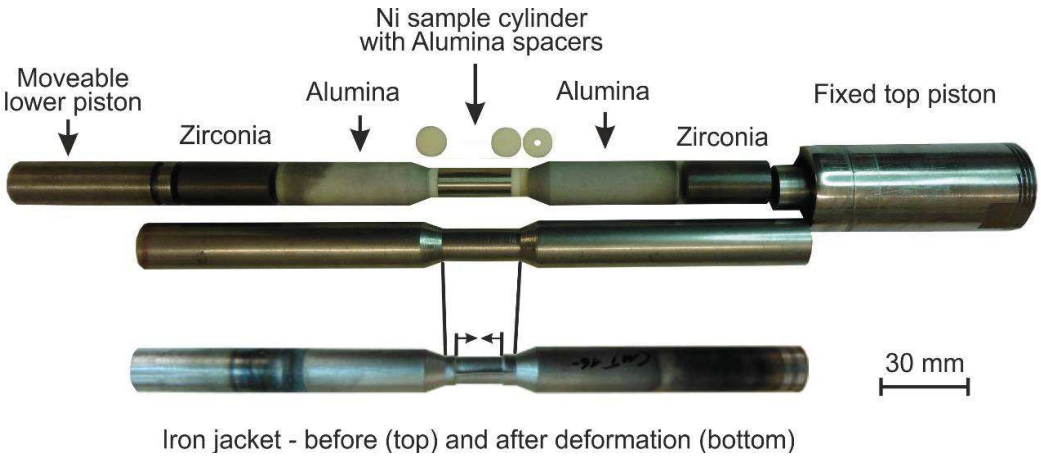

Fig. II-4 Image of a typical sample assembly. The bottom assembly experienced a deformation at 1200 °C to 8 % of strain. Note the lighter colors of the post-deformation Fe jacket towards the center and bottom, corresponding to the centered hot-zone.

The hot-zone is calibrated in separate furnace calibration experiments. Figure II-5 shows an example calibration for Furnace 19, used in the deformation experiments of Chapter III. The current of the three furnace wirings (top, center and bottom) is adjusted till the length of the hot-zone is maximized (20 mm) and the temperature deviation minimized (± 2 °C). Adjustments are unique to each furnace and repeated for the different temperature ranges used in experiments.

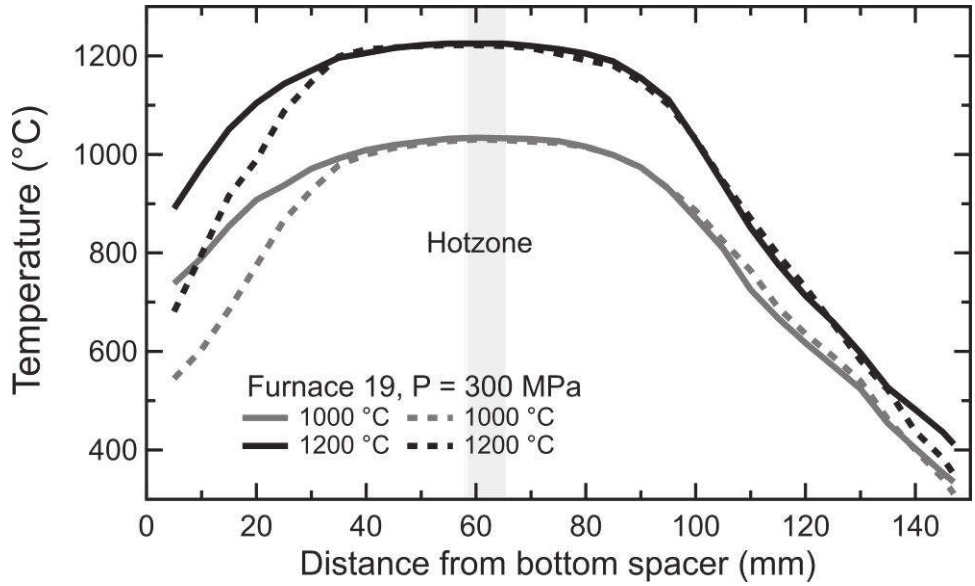

Fig. II-5 Temperature calibration curves for Furnace 19 used in Chapter III. Grey solid lines show final calibration curves at 1000 °C, black solid lines final curves at 1200 °C, dashed lines show initial calibration curves.

II-1.2 Rotary Shear Deformation Apparatus

High-velocity shear deformation started by modifying frictional welding machines (Spray 1987, 1988, 1993, 1995, 2005), successfully reproducing texture and chemistry of pseudotachylites. Compared to the Paterson Press's uni-axial deformation at low strain rates (10^{-5} s^{-1}), rotary shear deformation takes a different approach. Samples are deformed to high values of strain (up to several 10.000) at high slip velocities up to > 1 ms^{-1}. The strain rate is a function of the sample radius, decreasing towards zero at the center since deformation is achieved by rotation around the deformation axis. This large gradient in strain rate and hence strain can be both an advantage or disadvantage. While it allows to investigate microstructures at different strains in one sample, later analyses must be done at known radii.

In Chapter V of this thesis, I employ the low to high velocity rotary shear apparatus (*LHVS*) at the Rock Mechanics Laboratory, Durham University (UK; Model MIS-233-1-77; Ma et al. 2014; De Paola et al. 2015). A schematic of the LHVS is given in Figure II-6. A servo motor with 140 Nm of torque is coupled to a gear and belt system that provides three ranges of slip rates (1.4×10^{-3} to 2.1 ms^{-1}; 1.4×10^{-6} to 2.1×10^{-3} ms^{-1} and 1.4×10^{-9} to 2.1×10^{-6} ms^{-1}; Ma et al. 2014). An axial force of up to 10 kN is applied by a compressed air actuator (Bellofram type cylinder) with a 92 mm stroke. Fluctuations during loading are compensated by a high-precision air regulator. The revolution rate, cumulative revolutions and rotation angle are recorded by a rotary encoder (Omron E6C3-5GH, 3600 pulses/revolution) and potentiometer (Midori Precisions, CPP-60). The applied torque is measured by a cantilever-type gauge (max 1 kN, resolution $\pm 5 \times 10^{-4}$ kN in combination with a torque bar fixed to the lower main shaft. Axial displacement is recorded by a strain-gauge type displacement transducer (TSK CDP-10S2) with a capacity of 10 mm and a resolution of $\pm 2 \times 10^{-3}$ mm and axial force by a compressive load cell with a capacity of 10 kN and a resolution of ± 0.005 kN. The loading column is supported by a thrust bearing (friction coefficient < 0.003), allowing free rotation and thus applying nearly all torque to the torque gauge.

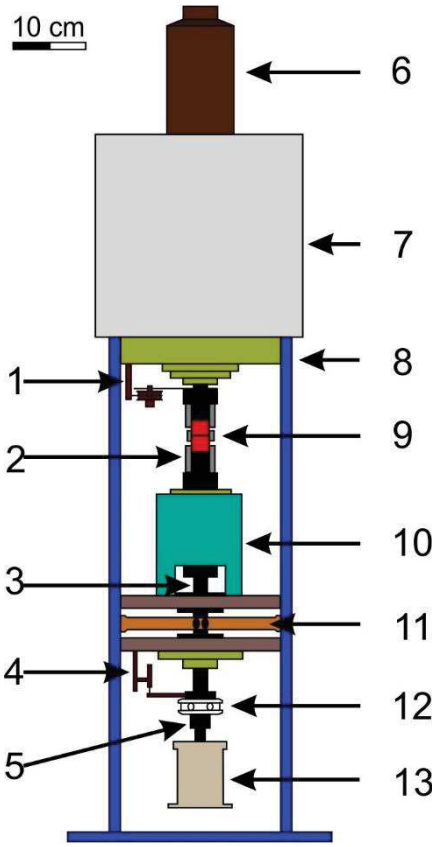

Fig. II-6 Schematic drawing of the low to high velocity rotary shear apparatus (LHVS) at the Rock Mechanics Laboratory, Durham University (UK; Model MIS-233-1-77; Ma et al. 2014; De Paola et al. 2015). The numbered main units are (1) Rotary encoder, (2) Specimen locking devices, (3) Axial loading column, (4) Axial displacement transducer, (5) Axial load cell, (6) Servomotor, (7) Gear/belt box, (8) Frame, (9) Specimen assembly, (10) Lower frame, (11) Torque gauge, (12) Thrust bearing, (13) Pneumatic actuator.

Sample material is layered between Ti cylinders with radii of up to 25 mm and enclosed by PTFE sleeves, allowing to deform an average of 0.5 – 2.5 g of material in layers of a few mm thickness. The surfaces of the Ti cylinders in contact with the sample are machined with 500 µm deep pyramidal grooves to simulate slip surface roughness and facilitate shear. A hydraulic mechanical lock assures alignment to the deformation axis.

II-2 Analytical procedures

II-2.1 Electron backscatter diffraction

Electron **b**ack**s**catter **d**iffraction (EBSD) is a Scanning electron microscope (SEM) based technique used to study the microstructure and crystallography of crystalline solids, namely metals, minerals, semiconductors and ceramics. EBSD provides quantitative information about phase identity, grain size, grain orientation, grain boundary features, and texture. A schematic drawing of the CamScan X500FE Crystal Probe at Geosciences Montpellier is given in Figure II-7.

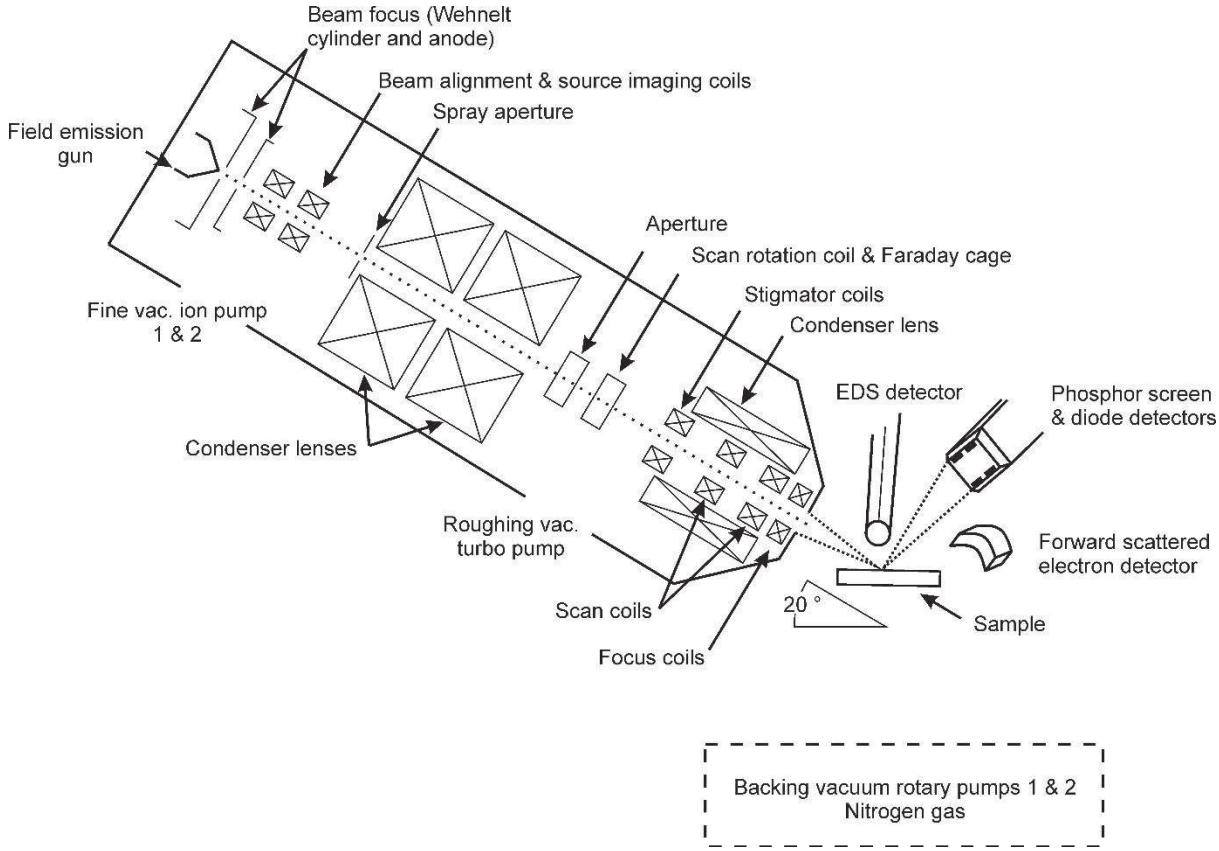

Fig II-7 Schematic drawing of the CamScan X500FE Crystal Probe EBSD main unit at Geosciences Montpellier.

Different to a common SEM, samples in the EBSD are oriented at 20 ° to the incident electron beam (Figure II-7). The electron beam is rastered over the sample surface, where it diffracts and yields a conical emanating diffraction pattern. The diffracted rays hit a phosphor screen, where constructive and destructive interference create a collection of bands called *Kikuchi bands* (Kikuchi, 1928), which are representative both of the unit cells of the crystal lattice and the orientation of the crystal planes. The Kikuchi bands are detected by a charge-

coupled device (CDD), digitalized, indexed and compared to a database of known phases. In this way, both the phase at each data point in the SEM raster and its orientation can be determined. Figure II-8 shows a schematic of the electron ray-sample interaction and Figure II-9 an exemplary Kikuchi pattern for Fosterite.

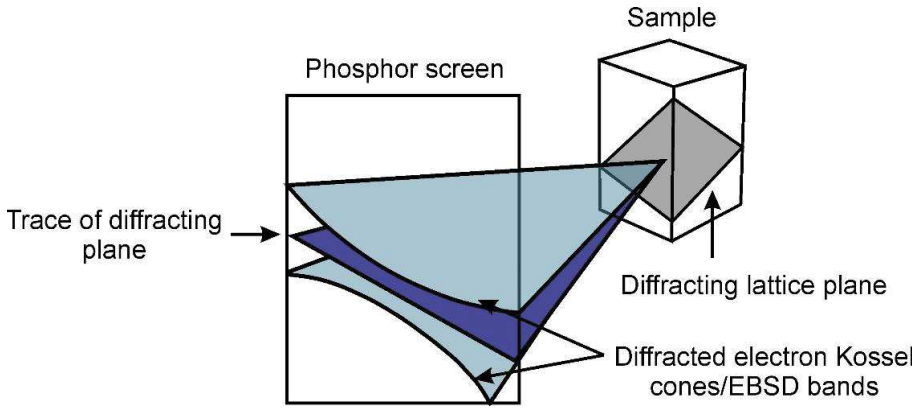

Fig II-8 Schematic drawing of electron beams diffracted off a sample creating Kikuchi bands on the detector plane.

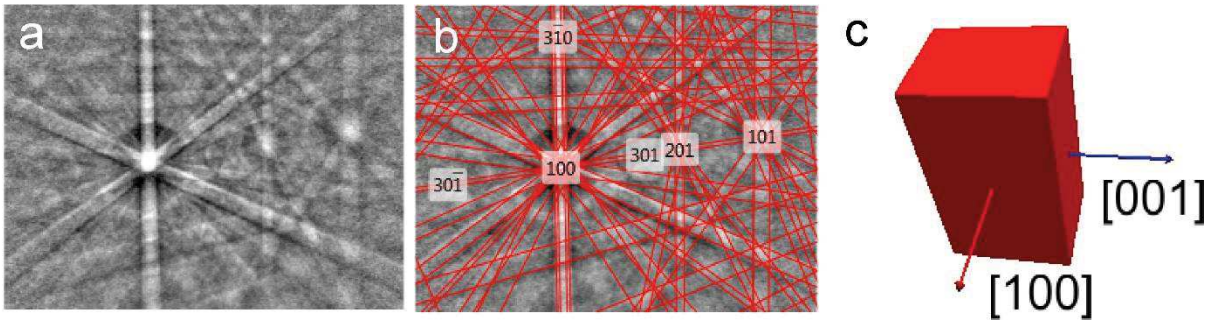

Fig II-9 (a) Exemplary Kikuchi pattern of forsterite (b) indexed bands representing certain crystal planes and the calculated crystal orientation (c) box model of the forsterite with lattice crystallographic orientation scaled to the unit cell dimensions.

The nominal angular resolution for EBSD is ~ 0.5 ° (Maitland and Siltzman, 2007) and the spatial resolution both related to the resolution of the SEM and limited by electrostatic charge building up in non- and semiconductors. In case of the semiconductor olivine, the maximum spatial resolution with well prepared samples is in the order of 50 nm. This is strongly influenced by the quality of the sample polishing, the sintering of the grains and the application of carbon coating. Samples embedded in non-conductive epoxide resin tend to produce imaging artifacts at pores and plug-outs or when epoxy is exposed, therefore

interrupting the electric circuit. Apart from artifacts in orientation maps, charging can be detected during measurement as a visible burn on already imaged sample surfaces and an image shift during rastering. An example of an electron burn is shown in Figure II-10.

Fig. II-10 Example of the effects of electrostatic chargeup during EBSD. Previously analyzed areas appear brighter. Higher levels of charging will lead to skipped rows, warping and other artifacts.

Apart from the sample and polishing quality, the angular resolution and percentage of non-indexed points are influenced by both the time over which the signal of the CCD is averaged (so called frame averaging) and the presence of a sample coating. A higher frame averaging improves the signal to noise ratio and therefore allows better indexing and higher angular resolution while the presence of a coating reduces the energy and depth of interaction of the incident electron beam and hence the quality of the signal. Figure II-11 illustrates the influence of both frame averaging and a thin carbon coating (10-20 nm) on a sample of olivine polished to a finish using colloidal silica (0.04 µm particles). Figure II-12 shows the surface of a similar olivine sample where the left half is coated and the right half uncoated, as well as the influence on the contrast of the Kikuchi bands to the noise background.

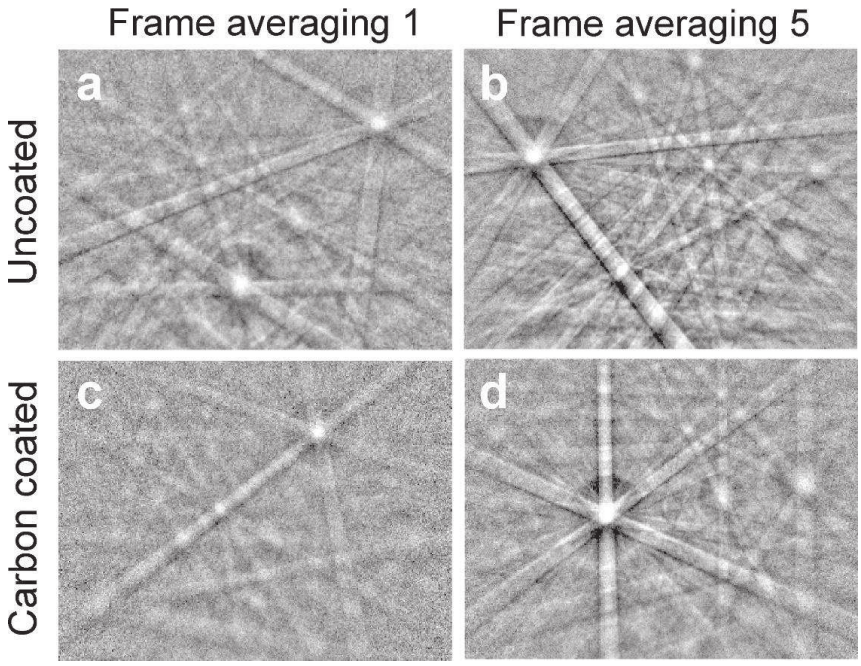

Fig. II-11 Contrast of Kikuchi bands as a function of frame averaging and cabon coating.

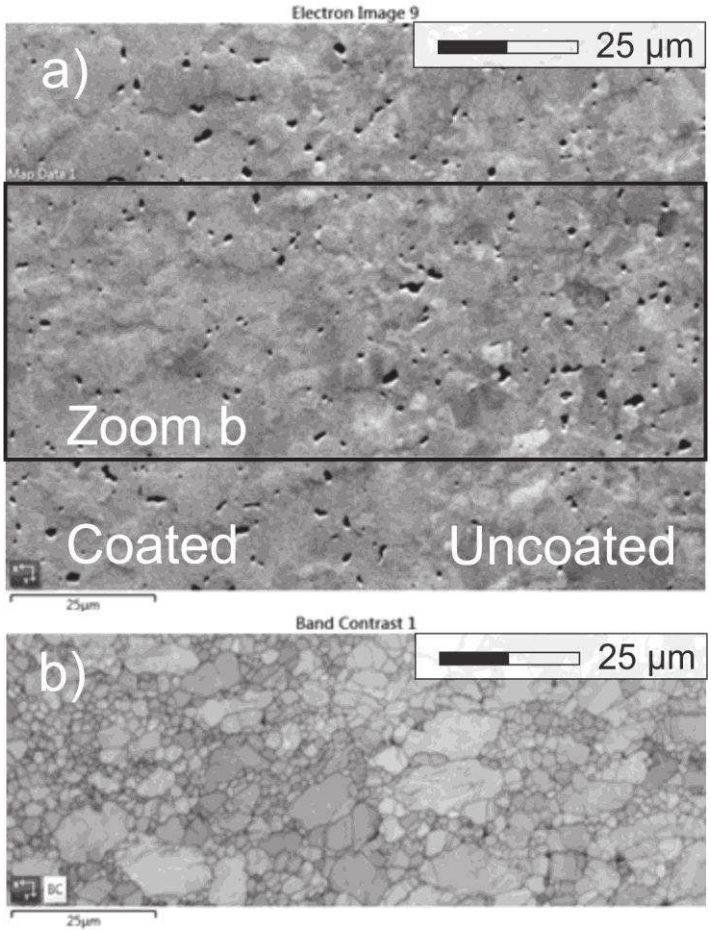

Fig. II-12 Forward scattered electron image (a) and band contrast (b) of sample CMT 16-9, showing the influence of carbon coating. The left half of both images is carbon coated, while the right remains uncoated.

II-2.2 Transmission electron microscopy

Opposed to SEM, transmission electron microscopy (SEM) utilizes an electron beam transmitted through the sample. Imaging is achieved either based on contrast or diffraction. Imaging by contrast depends on the electron density in the sample plane. Since the incident electron beam passes through the sample, its amplitude and phase are changed due to absorption or high-angle scattering. Imaging by phase contrast is also called high-resolution (HR) TEM and utilizes the interference of the electron beam with itself in the image plane. Diffraction imaging indexes diffraction patterns generated on the imaging apparatus by focusing the back focal plane instead of the imaging plane. The resulting pattern carries information about the space group symmetries (structure) and orientation of the sample. By tilting the sample in-between imaging, typically in increments of 1°, can a three-dimensional image be created.

II-3 Starting material and sample preparation

The main sample material used in this study is derived from iron bearing, gem quality olivine from San Carlos, Arizona, USA. San Carlos olivine has a consistent chemical composition of $(Mg_{0.91}Fe_{0.09}Ni_{0.003})_2SiO_4$ (Buening & Buseck, 1973; Frey & Prinz, 1978), a naturally low water content (< 1 wt ppm; Mackwell et al. 1985; Mei & Kohlstedt 2000; Demouchy 2010) and a low concentration of inclusions or line defects. Crystals of San Carlos olivine were crushed by attrition and impact in a gas stream in a fluid energy mill. The resulting powder with grain sizes of around 2 µm is cleaned of ferrous metals in a magnetic seperator. To fabricate dense polycrystalline samples resembling mantle rocks, the powder is first cold-pressed in Ni capsules (8 mm diameter, 16 mm long) at room temperature and 2.8 MPa. The Ni capsules are closed with Ni discs and externally applied cyanoacrylate. The olivine sinters and densifies in a final hot press step for 3 h at 1200 °C and 300 MPa hydrostatic confining pressure in the Paterson Press. These steps allow comparison to the literature by following a well established procedure (e.g. Mackwell & Kohlstedt 1990; Bai et al. 1991; Mei & Kohlstedt 2000; Chen et al. 2006; Demouchy et al. 2009; Hansen et al. 2011; 2012). After deformation, Ni capsules were dissolved in a 1:1 mixture of HNO_3 and HCl and the recovered samples cut parallel to the deformation axis. Embedding the samples in epoxy and polishing of thick sections, as well as carbon coating (10 – 20 nm coat thickness) for

SEM and EBSD analyses were performed by C. Nevado, D. Delmas and F. Barou, respectively, at Geosciences Montpellier.

Crushed powders of San Carlos olivine analyzed by EBSD in Montpellier already show a non-zero density of dislocations and an axial [010] texture where crystal [100] and [001] axes are aligned in a girdle perpendicular to the compression axis, and [010] axes are parallel to the compression axis. Since single crystals of San Carlos olivine show a naturally low defect density, crushing must already introduce significant local stresses and dislocations. The axial [010] can be observed even before cold-pressing and can most likely be linked to cleavage on (010) during crushing and later sedimentation, as also indicated by aspect ratios of 1.4 – 1.5.

For friction experiments in torsion, to achieve samples free of initial microstructure and texture, we employ synthetic olivine synthesized by vacuum sintering (Sanosh et al. 2010, Koizumi et al. 2010). Colloidal silica and highly dispersed $Mg(OH)_2$ and $Fe(CO_2CH_3)_2$ with particle sizes below 50 nm serve as sources for MgO, FeO and SiO_2. These powders are calcinated at 960 °C for 3 h to achieve aggregate sizes of ~ 80 nm. The large contrast in grain size compared to the 2-27 μm of crushed San Carlos olivine helps to identify grain size sensitive deformation mechanisms.

Chapter III – Stress evolution and associated microstructure during transient creep of olivine at 1000-1200 °C

This chapter presents a fully characterized set of deformation experiments, correlating the mechanical data with the microstructure of deformed polycrystalline olivine. The data presented here was published in Physics of the Earth and Planetary Interiors in 2018, under the title *Stress evolution and associated microstructure during transient creep of olivine at 1000-1200 °C*. It is reshaped here due to copyright issues (as the copy available at hal.archives-ouvertes.fr).

Stress evolution and associated microstructure during transient creep of olivine at 1000-1200 °C

M. Thieme[1*], S. Demouchy[1], D. Mainprice[1], F. Barou[1], P. Cordier[2]

[1] Geosciences Montpellier, CNRS & Université de Montpellier, UMR5243, 34095 Montpellier, France

[2] Univ. Lille, CNRS, INRA, ENSCL, UMR 8207 - UMET - Unité Matériaux et Transformations, F-59000 Lille, France

* corresponding author

The published version of this article can be cited as:

Thieme, M.*, Demouchy, S., Mainprice, D., Barou, F., Cordier, P. (2018) Stress evolution and associated microstructure during transient creep of olivine at 1000-1200 °C, Phys. Earth Planet. Int., doi: 10.1016/j.pepi.2018.03.002

Abstract

We study the mechanical response and correlated microstructure of axial deformed fine-grained olivine aggregates as a function of incremental finite strains. Deformation experiments were conducted in uniaxial compression in an internally heated gas-medium deformation apparatus at temperatures of 1000 and 1200 °C, at strain rates of 10^{-6} s^{-1} to 10^{-5} s^{-1} and at confining pressure of 300 MPa. Sample volumes are around 1.2 cm^3. Finite strains range from 0.1 to 8.6 % and corresponding maximal (final) differential stresses range from 80 to 1073 MPa for deformation at 1000 °C and from 71 to 322 MPa for deformation at 1200 °C. At 1200 °C, samples approach steady state deformation after about 8 % of strain. At 1000 °C, significant strain hardening leads to stresses exceeding the confining pressure by a factor of 3.5 with brittle deformation after 3 % of strain. Deformed samples were characterized by electron backscatter diffraction (EBSD) and transmission electron microscopy (TEM). EBSD maps with step sizes as low as 50 nm were acquired without introducing analytical artifacts for the first time. The grain size of deformed samples ranges from 2.1 to 2.6 µm. Despite clear strain hardening, texture or microstructure do not change as a function of stress or finite strain. This observation is supported by a constant texture strength (J-index) and symmetry (BA-index), constant grain shape and aspect ratio, constant density of geometrically necessary dislocations, grain orientation spread, and constant subgrain boundary spacing and misorientation in between samples. TEM shows that all samples exhibit unambiguous dislocation activity but with a highly heterogeneous dislocation distribution. Olivine grains display evidence of [100] and [001] slip activity, but there is no evidence of interaction between the dislocations from the different slip systems. Several observations of grain boundaries acting as dislocation sources have been found. We find no confirmation of increasing dislocation densities as the cause for strain hardening during transient creep. This suggests other, yet not fully understood mechanisms affecting the strength of deformed olivine. These mechanisms could possibly involve grain boundaries. Such mechanisms are relevant for the deformation of uppermost mantle rocks, where the Si diffusion rate is too slow and dislocation glide must be accommodated in another way to fulfill the von Mises criterion.

Keywords: plastic deformation; olivine; creep; dislocations; Earth lithosphere.

III-1 Introduction

Olivine is the most abundant (> 60%$_{vol}$) and the weakest mineral phase of Earth's upper mantle. As such, it largely controls the rheology of the upper mantle and in turn the contribution of mantle convection to the formation and motion of tectonic plates. Since the upper mantle encompasses rocks within a wide range of temperatures, its rheology has to be studied in an equally broad thermal range.

Early flow laws quantifying the rheology of olivine were mostly obtained from experiments at temperatures above 1200 °C (*e.g.* Chopra & Paterson, 1984; Karato et al., 1986; Bai et al., 1991; Hirth & Kohlstedt, 1995; Mei & Kohlstedt, 2000a, 2000b; Faul et al. 2011; Keefner et al., 2011; Tielke et al., 2017) to avoid to reach the brittle field. Experiments performed at temperatures relevant to the uppermost lithospheric mantle (≤ 1000 °C, *e.g.* Evans & Goetze, 1979; Raterron et al., 2004; Demouchy et al. 2009, 2013, 2014; Mei et al., 2010; Idrissi et al., 2016; Tielke et al., 2016) report a lower strength of olivine than was expected from extrapolation of high-temperature flow laws. The low temperature plasticity is a key to understanding deformation of the shallow upper mantle (Hirth & Kohlstedt, 1995) but also in subducting slabs (Goetze & Evans, 1979; Kirby, 1980; Karato et al., 2001), where it governs the stress storage capacity and therefore the maximal stress release of deep earthquakes (*e.g.*, Proietti, 2016).

Until recently, the deformation and microstructure of olivine were characterized under a so-called mechanical *steady state*, when stress becomes constant and independent of plastic strain. Therefore, the mechanical response and evolution of microstructure before reaching steady state (*i.e.*, transient creep) is largely not understood. The initial rapid increase in stress is traditionally attributed to an increase in the dislocation density, which is reported to become constant in single crystals after about 2 % of strain (*e.g.*, Durham et al., 1977). Even under constant dislocation densities, the dislocation structures continue to evolve and reaching a constant dislocation structure requires a finite amount of strain. Transient creep at temperatures and pressures relevant for the lithospheric mantle might prove crucial to understanding the initiation and localization of deformation processes that impact lithospheric plate generation and motion.

The main deformation mechanisms of olivine are 1) glide and climb of dislocations in the crystal lattice, typically called dislocation creep 2) diffusion of atoms and vacancies at temperatures above approximately 1200 °C, which is grain size sensitive (*i.e.*, diffusion creep) and 3) grain boundary controlled mechanisms, such as grain boundary migration or grain boundary sliding. The dominant deformation mechanism depends on the stress, temperature, grain size, strain rate, the crystal chemistry, the oxygen fugacity, partial melt content and even the trace amount of hydrogen (*e.g.* Carter & Lallemand, 1970; Chopra & Paterson, 1981, 1984; Mackwell et al., 1985; Cooper & Kohlstedt, 1984, 1986; Bai et al., 1991; Bai & Kohlstedt, 1992; Mei & Kohlstedt, 2000 a,b; Hirth & Kohlstedt, 1995, 2003; Warren & Hirth, 2006; Mackwell, 2008; Faul et al., 2011, 2016; Keefner et al., 2011; Demouchy et al., 2012; Tielke et al., 2016, 2017). Dislocation glide is thought to be the dominant deformation mechanism at low temperatures (< 1200 °C in Fo$_{90}$) and for grain sizes > 1 mm prevalent in mantle olivine, since Si is the slowest diffusing species in silicates and its diffusivity is highly dependent on temperature (Chakraborty, 2010). Yet, dislocations in olivine can only glide in three independent slip systems ([100](010), [100](001), [001](010) or [100](010), [001](010), [001](100)). In the case of inhomogeneous flow (*i.e.*, flow in polycrystals), at least four independent slip systems must operate to satisfy the von Mises criterion (Mises, 1928; Hutchinson, 1977). Therefore, the currently known dislocation slip systems in olivine are not enough, and additional degrees of freedom must be provided by *e.g.* dislocation climb, grain boundary sliding or grain boundary migration triggered by disclinations. Disclinations (rotational topological defects) were known to exist in liquid crystals (Friedel, 1922; Frank, 1958) but were thought to be too energetically costly in crystalline solids. Nevertheless, they were recently described along the grain boundaries of copper and olivine (Beausir & Fressengeas, 2013; Cordier et al. 2014).

The slip systems in which dislocations glide in olivine are well documented, and Turner (1942) already anticipated the principal glide system in naturally occurring olivine to be [100](010). Most of the early deformation experiments at high temperature targeting slip systems were conducted by Raleigh (1965, 1967, 1968), who concluded that the dominant slip system is dependent on the temperature and the strain rate: at 10^{-5} s^{-1}, glide on [001](100) dominates at < 300 °C, [001]{110} between 300 to 1000 °C and finally [100]{0kl} at temperatures of > 1000 °C (see also Young, 1969). A comparison of microstructures in naturally and experimentally deformed peridotites by Nicolas (1986) confirmed that the same slip systems are active. Such a comparison holds true for mantle rock textures (*e.g.*, Nicolas & Poirier, 1976; Gueguen & Nicolas, 1980; Tommasi et al., 1999, 2016).

First olivine flow laws were provided by Carter & Avé-Lallemant (1970) for wet and dry dunites and lherzolites, also observing dislocation climb controlled processes (polygonization) and recrystallization at temperatures of 1000 °C and 1050 °C respectively.

Carter and Avé-Lallemant attributed a weakening effect to the presence of hydrogen in the structure of olivine, expressed by a reduced activation energy of dislocation

creep (335 instead of 502 kJ.mol^{-1}). Hirth & Kohlstedt (1996), Mei & Kohlstedt (2000 a,b), Demouchy et al. (2012, 2014), Fei et al. (2013), Girard et al. (2013) and Tielke et al. (2017) confirm a weakening effect by water, although the most recent results highlight that it might induce a relatively limited effect (*i.e.*, viscosity diminution by only a factor of 10 for hydrous olivine viscosity at mantle strain rates, Tielke et al., 2017) for hydrogen concentrations reported in spinel-bearing peridotite typical of the lithospheric mantle (Demouchy and Bolfan-Casanova, 2016).

Based on high pressure deformation experiments, Karato and co-workers have proposed a classification in five types of olivine fabrics developing as a function of the applied stress and water content (Jung and Karato, 2001), but until now, the physical mechanism which could explain the crystallographic preferred orientations (CPO) variations is still lacking. Other studies recognized an effect of grain size on the strength of olivine (Goetze, 1978; Karato et al., 1986; Karato and Wu, 1993; Katayama et al., 2004). At smaller grain sizes (sub µm), dislocations are increasingly captured by grain boundaries, resulting in only few organized sub grain boundaries. In such small grains, the rate-limiting factor is dislocation glide or ionic diffusion rates, as opposed to dislocation climb in larger grains and for higher finite strains (*e.g.*, Hiraga et al., 2011 ; Miyazaki et al., 2013).

In this study, we perform a series of deformation experiments at high pressure and high temperature on fine-grained polycrystalline olivine aggregates at temperatures of 1000 °C and 1200 °C. Experiments are stopped at increasing higher finite strains (0 to 8.6 %, representing all stages of the stress-strain curve. The starting material and deformed samples are characterized by scanning electron microscopy (SEM), electron backscattered diffraction (EBSD) and transmission electron microscopy (TEM).

III-2 Methods

III-2.1 Starting material and experimental method

Olivine crystals from San Carlos (Arizona) with the following composition $(Mg_{0.91}Fe_{0.09}Ni_{0.003})_2SiO_4$ (e.g., Buening & Buseck, 1973; Frey & Prinz, 1978) are used for the deformation experiments. The fine powder was obtained by grinding olivine crystals in a fluid energy mill (Gribb & Cooper, 1998). San Carlos olivine naturally has extremely low water content of less than 1 ppm wt H_2O (Mackwell et al., 1985; Mei & Kohlstedt, 2000a; Demouchy, 2010). Fine-grained powder of San Carlos olivine was cold-pressed and subsequently hot-pressed in Ni sleeves at 1200 °C and 300 MPa for 3 hours, producing dense polycrystalline samples ~ 8 mm in diameter and ~ 16 mm long. The Ni sleeves were closed prior to hot-pressing with fitted Ni disks (200 µm thick), held in place by ~2 µl of externally applied superglue. The glue is dried out before insertion into the apparatus, volatized during hot-pressing and does not induce hydrogen incorporation into the sample. Hot-pressing, as well as axial deformation was performed in a high-pressure high-temperature internally heated, *in situ* deformation apparatus (also called the Paterson Press; see Paterson, 1990) using Argon as pressure medium. This deformation apparatus allows a high resolution of the applied stress (± 10 MPa) and minimal thermal gradient (± 2 °C) along a hot zone of approximately 20 mm length (Paterson, 1990). Sample volumes of ~1 cm^3 and diameter to length ratio of 1:2 reduce boundary effects on the texture evolution and stress distribution. Samples were deformed in axial compression at 300 ± 2 MPa confining pressure, for constant displacement rates (1.25 to 1.70×10^{-4} mm s^{-1}). Part of the displacement is taken up by elastic deformation of the apparatus. Consequently, the instantaneous strain rate of the sample changes as stress evolves during the experiment, reaching 10^{-5} s^{-1} at mechanical steady state conditions. Temperatures were kept constant during deformation. The Ni capsules containing the olivine samples were mounted with alumina and zirconia pistons inside an iron jacket (*e.g.*, Paterson, 1990; Mei & Kohlstedt, 2000a). The oxygen fugacity was theoretically controlled by the nickel capsule. However, in a recent experimental study, the fO_2 in large sample volumes has been shown to decrease towards the sample center, resulting in a linear $Log(fO_2) \approx -10$, at a distance > 0.5 mm from the capsule interface (Faul et al., 2017, their fig 5.), which remains in line with common mantle rocks (Frost & McCammon, 2008). Temperature was manually increased at a rate of approximately 10 °C/min before using the automatic temperature controller. Quenching of the samples is achieved by a manually controled decrease of furnace power, reducing temperature by 100 °C/min. Faster cooling might induce severe damage to the furnace. A total of ten samples were deformed at temperatures of 1000 °C and 1180-1200 °C. Experimental

Table III-1 Experimental conditions for deformation under 300 MPa of confining pressure and mechanical results. The strain rate is given as the instantaneous strain rate at the end of each respective deformation experiment.

	Deformation at 1000 °C						Deformation at 1200 °C				
	CMT16-6	CMT16-2	CMT16-4	CMT16-8	CMT17-4	CMT17-2	CMT17-1	CMT16-12	CMT16-15	CMT16-13	CMT16-9
Temperature [°C]	1000	1000	1000	1000	1000	1000	1200	1200	1200	1200	1200
Duration [min]	11	24	42	79	87	218	8	25	40	84	174
Initial length L_0 [mm]	13.50	16.45	16.10	12.53	17.15	13.75	16.95	16.90	16.94	15.82	16.96
Strain rate $\dot{\varepsilon}$ [s^{-1}]	1.9×10^{-6}	2.8×10^{-6}	3.4×10^{-6}	3.3×10^{-6}	5.8×10^{-6}	1.1×10^{-5}	4.0×10^{-6}	7.2×10^{-6}	7.8×10^{-6}	1.0×10^{-5}	1.0×10^{-5}
Finite strain ε [%]	0.11	0.30	0.42	1.07	1.6	7.33	0.19	0.88	1.50	3.68	8.59
Diff stress σ_{max} [MPa]	80	258	440	684	787	1073	71	150	232	313	322

conditions are listed in Table III-1.

To account for the load supported by the iron jacket and nickel sleeve, the flow laws reported by Frost and Ashby (Deformation mechanism maps: the plasticity and creep of metals and ceramics. 1982) were used, following a well-established procedure (Mei & Kohlstedt, 2000a; Chen et al., 2006; Demouchy et al., 2009; Hansen et al., 2011, 2012). The calculated stress was corrected for (1) the instantaneous change in cross-sectional area due to sample shortening, assuming that samples kept their cylindrical shape and constant volume and (2) apparatus stiffness. The stiffness of the deformation apparatus is determined in a separate experiment to be 82.5 kN/mm.

Deformed olivine samples were recovered by cutting the assembly with a low speed saw. Thin sections of the deformed olivine and the hot-pressed samples were cut parallel to the deformation axis (long axis of the cylinder) after removal of 2 mm from the lower- and topmost parts, where stresses are expected to be heterogeneously distributed (Griggs *et al*., 1960). The heterogeneous stress distribution at the sample ends is caused by friction at the alumina spacer-sample interface, leading to a lower increase in sample radius during shortening compared to the center of the sample (*i.e.*, barreling effect, see Moosbrugger, 2002). Thus the lower- and topmost parts were not mapped by EBSD. For some of the cold-pressed and hot-pressed samples (CMT16-1, CMT16-5, CMT16-7), sections were cut perpendicular to the long axis from the ends of the sample cylinders, to preserve parts of the sample for later deformation.

III-2.2 Scanning electron microscope based electron backscatter diffraction

Grain size distributions, shapes and orientations, as well as the microstructure were analyzed by indexation of electron backscatter diffraction patterns in a scanning electron microscope (CamScan X500FE CrystalProbe) at Geosciences Montpellier. Sample sections and a small amount of the olivine powder were embedded in epoxy and polished, including a final chemo-mechanical polish using colloidal silica (0.04 µm particles, average polishing times of 1 hour). Exposed sample surfaces were carbon coated with a coating thickness of 10-20 nm, leaving a non-coated window in the center of the sample for EBSD analyses. Working distance was 24 – 25.1 mm, acceleration voltage was 17 to 17.5 V and the beam current was 10 nA for EBSD map acquisition, down to 5 nA for backscattered electron (BSE) imaging. In all cases, the acquired phases were olivine ($(Mg, Fe)_2SiO_4$), diopside ($CaMgSi_2O_6$), enstatite ($(Mg,Fe)SiO_3$) and chromite ($(Fe,Mg)Cr_2SiO_4$). EBSD data was obtained with the Oxford instruments HKL Aztec2 software and treated with the MTEX toolbox (Hielscher & Schaeben 2008, Bachmann et al. 2010). Data treatment removed wild spikes and filled non-indexed pixels when 7 neighbors with identical orientations were present. Grain boundaries were identified where the misorientation to the next pixel is higher than 10°. Only grains with more than 5 pixels (corresponding to a minimum grain diameter of 0.6 µm) were considered for further calculations. The density of the orientation distribution function was calculated using an axially symmetric de la Vallee Poussin kernel, with half-width of 10° (band-width of 28 in spherical harmonic coefficients). Crystal preferred orientations (CPO) and the texture J-index (Bunge, 1982) were calculated. The texture J-index is a measurement of the texture strength calculated as the integral of the square of the orientation distribution function. Contrary to some past studies, here the J-index is calculated as area weighting to not overestimate the contribution of numerous small grains. Densities of pole figures of the CPO were normalized to a uniform distribution and contoured at intervals of 0.5 × uniform. The BA-index was introduced by Mainprice et al. (2014) to characterize the symmetry of olivine pole figures [100] and [010].

A total of 121 EBSD maps from 16 samples were aquired. Out of 121 maps, 33 large scale maps (> 20000 µm²) free of charging and drifting artifacts with step sizes of 0.2 µm (hot-pressed and deformed samples) or 1 µm (olivine powder and cold-press) were used to calculate microstructure and texture characteristics as the arithmetic mean of all suitable maps of a given sample. Consequently, the number of map pixels and grains used for calculation is high (*e.g.*, 2416 to 38675 grains per sample). For local and grain scale maps (< 2400 µm²), step sizes as low as 0.05 µm were sucessully applied for the first time on olivine agregates without electrostatic charging and drifting. The full set of EBSD parameters is given in supplementary Table S1 and a relevant selection is reported in Table III-2.

Table 2
Statistical parameters obtained from EBSD maps using MTEX. All values derived from data treatment are given as means, except for max aspect ratio and max grain size. No. EBSD maps gives the number of large scale (global) maps free of artifacts used for the parameter calculation.

	Powder	Cold-press	Hot-press				Deformation at 1000 °C					Deformation at 1200 °C				
			CMT16-1	CMT16-5	CMT16-7	CMT17-3	CMT16-6	CMT16-2	CMT16-4	CMT16-8	CMT17-2	CMT17-1	CMT16-12	CMT16-15	CMT16-13	CMT16-9
No. of EBSD maps	3	3	1	1	3	1	1	1	1	5	3	1	1	1	1	6
Step size [μm]	1	1	0.2	0.2	0.2	0.2	0.2	0.2	0.2	0.2	0.2	0.2	0.2	0.2	0.2	0.2
No. grains	13,240	45,918	2483	5431	10,125	1856	2885	13,433	4093	20,218	9668	3619	8463	8220	4077	31,846
Indexation rate [%]	28	41.3	97.6	93.8	96.5	98.37	92.2	97.1	96.2	95.9	92.3	96	96.7	96.8	96.3	96.7
Angular deviation [°]	0.85	0.71	0.42	0.46	0.47	0.46	0.55	0.42	0.42	0.41	0.56	0.53	0.4	0.37	0.4	0.43
Angular deviation (1σ)	(0.38)	(0.34)	(0.14)	(0.19)	(0.16)	(0.13)	(0.19)	(0.15)	(0.15)	(0.16)	(0.19)	(0.20)	(0.15)	(0.15)	(0.16)	(0.14)
Grain size[a] [μm]	2.1	2.3	1.8	1.4	1.7	2.8	1.4	1.7	1.6	1.6	1.6	1.6	1.5	1.6	1.6	1.6
Grain size (1σ)	(1.9)	(1.9)	(2.0)	(2.0)	(2.0)	(2.1)	(2.0)	(2.0)	(2.0)	(2.0)	(2.0)	(2.0)	(2.0)	(1.9)	(2.0)	(1.9)
Max grain size	21.9	23.3	19.8	19	21.9	22.3	16	21.1	16.7	26.9	17.2	17.6	15.4	18.1	18.4	16
Area norm. grain size	7.4	7.6	7.8	7	7.1	9.2	6.4	6.5	6.3	6.4	6.3	6.8	6	6.2	6.6	6.1
Kernel av. Mis.[b] [°]	0.81	0.62	0.27	0.37	0.26	0.21	0.35	0.28	0.3	0.29	0.43	0.31	0.28	0.27	0.29	0.28
Kernel av. Mis. (1σ)	(2.3)	(2.3)	(2.2)	(2.1)	(2.2)	(1.9)	(2.1)	(2.1)	(2.1)	(2.1)	(1.8)	(2.0)	(2.2)	(2.2)	(2.2)	(2.1)
GOS[c] [°]	0.69	0.65	0.49	0.76	0.49	0.44	0.71	0.52	0.55	0.58	0.83	0.55	0.54	0.53	0.59	0.48
GOS (1σ)	(3.3)	(2.6)	(3.5)	(3.0)	(3.5)	(3.1)	(3.1)	(3.3)	(3.3)	(3.1)	(2.5)	(3.1)	(3.5)	(3.5)	(3.3)	(3.4)
PARIS[d]	19	21	42	35	41	16	35	41	40	39	49	46	39	39	39	40
PARIS (1σ)	(27)	(35)	(19)	(17)	(18)	(17)	(17)	(17)	(17)	(17)	(27)	(25)	(17)	(17)	(16)	(17)
Sub GB mis.[e] [°]	2.4	2.4	3.2	3	3.1	3.1	2.9	3	3.1	3	3	3	3	3	3	3
Sub GB mis. (1σ)	(1.2)	(1.2)	(1.5)	(1.4)	(1.4)	(1.4)	(1.4)	(1.4)	(1.4)	(1.4)	(1.4)	(1.4)	(1.4)	(1.4)	(1.4)	(1.4)
J-index 1ppp[f]	1.6	1.6	1.8	1.6	1.6	1.7	1.7	1.2	1.2	1.5	1.7	1.5	1.4	1.4	1.5	1.6
J-index 1ppg	1.1	1.2	1.2	1.1	1.1	1.2	1.2	1.1	1.1	1.2	1.2	1.1	1.1	1.1	1.1	1.2
BA-index 1ppp[f]	0.2	0.2	0.1	0.5	0.2	0.2	0.2	0.2	0.3	0.2	0.2	0.4	0.2	0.2	0.3	0.3
Mis2Mean[g]	1	1	3.2	2.7	2.7	2	2.5	2.6	2.8	2.5	2.6	2.7	2.5	2.5	2.5	2.6
Mis2Mean (1σ)	(0.9)	(1.2)	(3.1)	(2.6)	(2.7)	(2.1)	(2.4)	(2.6)	(2.8)	(2.5)	(2.4)	(2.7)	(2.5)	(2.5)	(2.4)	(2.5)
Aspect ratio	1.4	1.4	1.5	1.5	1.4	1.5	1.5	1.4	1.5	1.5	1.5	1.5	1.5	1.5	1.5	1.5
Aspect ratio (1σ)	(0.4)	(0.3)	(0.3)	(0.4)	(0.4)	(0.4)	(0.4)	(0.3)	(0.4)	(0.4)	(0.4)	(0.4)	(0.4)	(0.3)	(0.3)	(0.4)
Max. aspect ratio	4.2	7.7	5.3	5.9	7.1	5.3	4.4	5.8	6.5	8.1	5.2	4.8	9.3	5.9	3.9	4.8

[a] The grain size reported is the geometric mean of the log-normal distribution of the grain equivalent diameter (diameter of a sphere with equivalent area of the respective grain).
[b] Geometric mean of the log-normal distribution of the Kernel Average Misorientation (proxy for density of Geometrically Necessary Dislocations), 2nd order, threshold of 5°.
[c] The grain orientation spread (GOS) is the average deviation in orientation between each point in a grain and the average orientation of the respective grain.
[d] Percentile average relative indented surface boundary, measure of the curvature of grain boundaries. A high PARIS indicates highly curved or indented boundaries.
[e] Subgrain boundaries are defined as 2°–10° misorientation. Subgrain boundary angles increase with polygonization and decrease with subgrain growth.
[f] One point per pixel (1ppp) uses every map pixel with an olivine orientation for the calculation of the texture j-index or BA-index. One point per grain (1ppg) uses the mean orientation of each grain.
[g] Mis2mean gives the misorientation angles from the mean within each respective grain. The given value is the mean over the whole EBSD map.

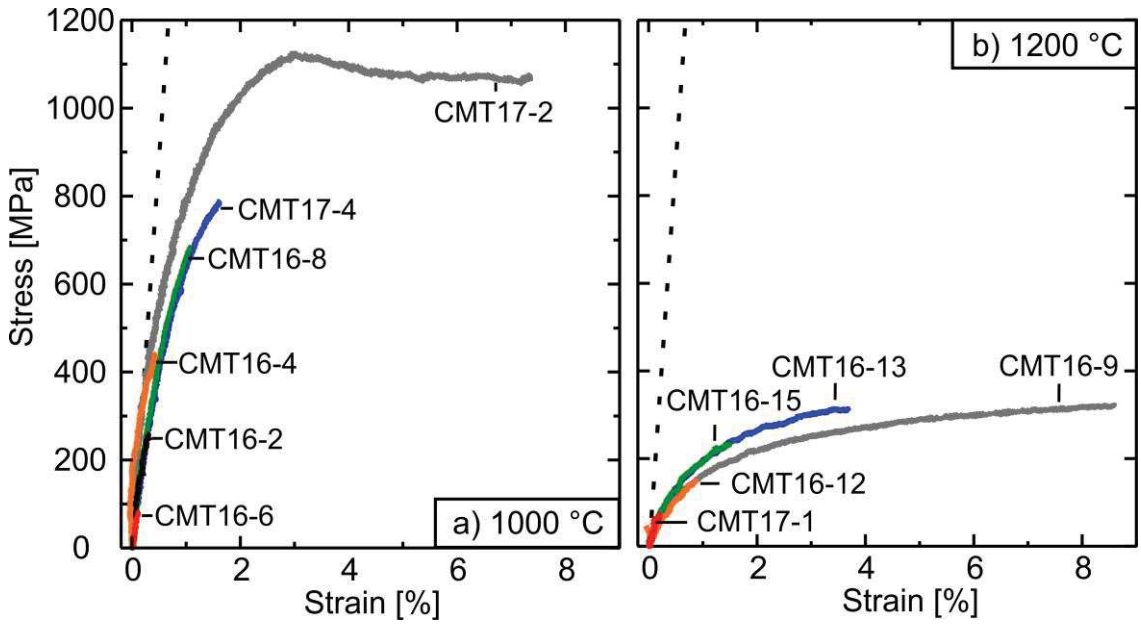

Fig. III-1 Differential stress versus strain curves for experiments at constant displacement rate, 300 MPa of confining pressure, (a) 1000 °C and (b) 1200 °C. Pure elastic deformation of polycrystalline San Carlos olivine is shown with dashed lines, based on a Young's modulus of (a) 152 GPa and (b) 146 GPa (Liu et al., 2005).

III-2.3 Transmission electron microscopy (TEM)

Transmission electron microscopy (TEM) was used to characterize the microstructures after the deformation experiments. Doubly polished thin sections (30 µm thick) of all deformed samples and hot-pressed sample CMT16-7 were prepared. The sample sections were cut parallel to the deformation axis. They were glued on a grid (Cu or Mo) and ion milled at 5 kV under a low beam angle of 15° until electron transparency was reached. The foils were subsequently covered with a thin layer of carbon. TEM observations were carried out at the University of Lille (France) using a Philips CM30 microscope operating at 300 kV and a FEI® Tecnai G2-20 twin microscope operating at 200 kV.

III-3. Results

III-3.1 Mechanical results

The results of the deformation experiments are reported in III-1 and all stress-strain curves are shown in III. 1. Optical microscopy of sample thin sections shows cracks that are sub-parallel to the long axis of the sample cylinder (the compression axis). There is no relative displacement along the cracks or shearing visible on the iron-jacket. The permanent finite strains range from 0.1 to 8.6 % and the strain rates range from 1.8×10^{-6} s^{-1} for low finite strain (< 0.5 % of strain) to 1×10^{-5} s^{-1} at high finite strain (> 4 % of strain). At 1000 °C, the stress-strain curve departs systematically from linear (elastic) behavior, even for strains below 0.5 %. The stress reaches a maximum of 1127 MPa at 3 % of finite strain (sample CMT17-2), at which point it drops by 60 MPa and becomes apparently independent of finite strain. At 1180-1200 °C, stress increases at a lower rate, reaching a maximum of 322 MPa at 8.6 % of finite strain (CMT16-9). No perfect steady state is reached; stress continues to increase at a very slow rate of 4 MPa per percent of strain. From the mechanical data, there is no evidence of stick-and-slip or brittle failure of the samples. At the same temperature and very similar displacement rates, the stress-strain curves differ slightly. As an example, samples CMT17-2 and CMT17-4, both deformed at 1000 °C, reach 954 and 787 MPa of stress respectively at 1.6 % of strain. Samples CMT16-9 and CMT16-13, both deformed at 1180 °C, reach 265 and 313 MPa of stress respectively at 3.7 % of finite strain.

The Young's modulus E of San Carlos olivine was calculated assuming the isotropic relation

$$E = 2G(1+\nu) \quad (1)$$

where G is the shear modulus and ν is Poisson's ratio. The shear modulus G was calculated for the respective temperatures and pressures using an initial shear modulus G_0 of 77.4 GPa, a pressure dependence G'_0 of 1.61 and a temperature dependence $\delta G_0/\delta T$ of -0.0130 GPa/K (Liu et al., 2005). By comparison with the deformation curves, neither at 1000 °C, nor at 1200 °C do the curves exhibit a linear segment indicating pure elastic

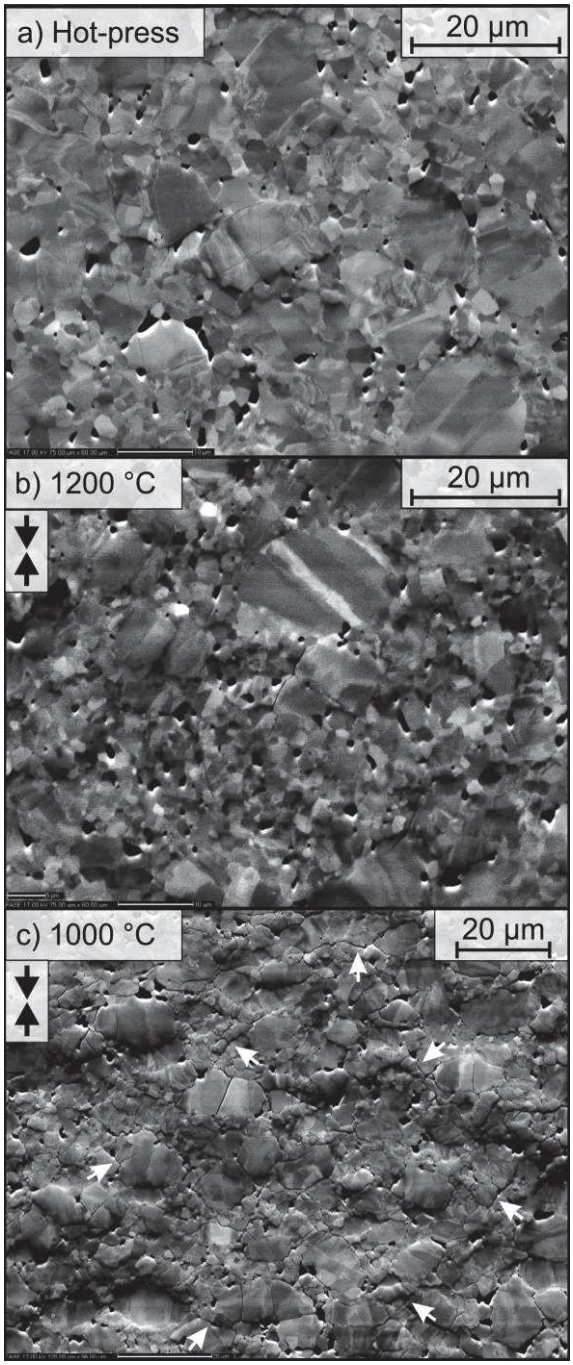

Fig. III-1 Forward scattered electron image from SEM. (a) prior to deformation (hot-press CMT16-7); (b) after deformation at 1200 °C and for 8.6 % of finite strain (CMT16-9); (c) after deformation at 1000 °C and for 7.3 % of finite strain (CMT17-2). Dark areas are plug outs from polishing and pores. White arrows show cracks developed by brittle deformation.

deformation. To determine if the deformation is mostly the result of anelasticity (stress and time dependence of elastic strain), we have subjected an already deformed sample (CMT17-4, 1000 °C, 1.6 % strain) to axial deformation. The pre-deformed sample reaches significantly higher stresses for the same values of finite strain, as displayed in Supplementary Figure S2. This suggests, that even at low values of finite strain, there is significant plastic deformation and hence hardening.

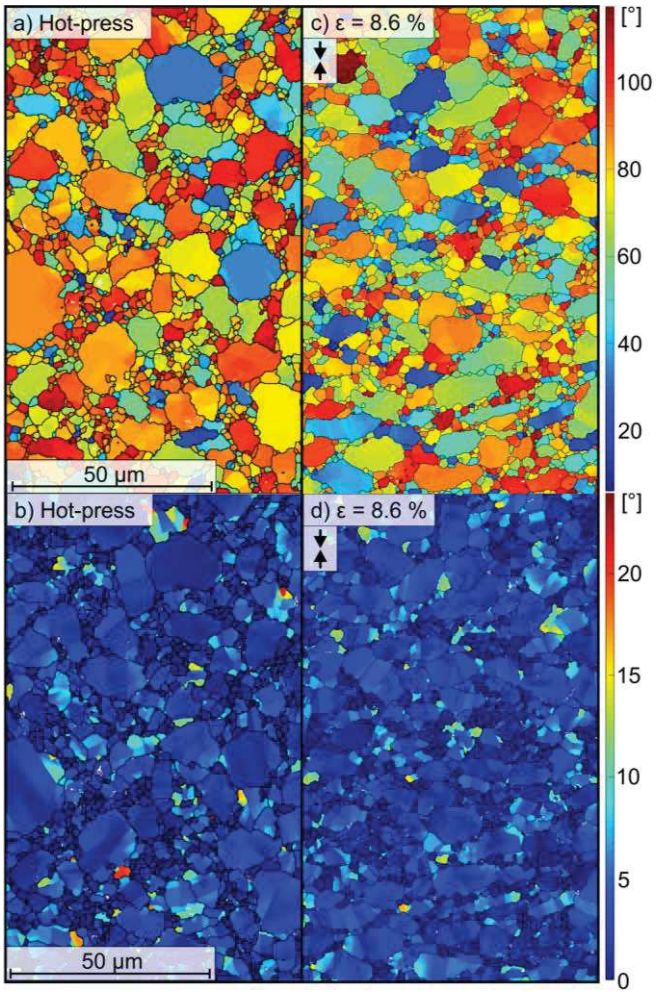

Fig. III-2 EBSD maps prior to deformation (a and b, hot-press CMT16-7) and post deformation (c and d, CMT16-9, 1200 °C), showing the misorientation to a central reference point (a, c) and the misorientation to the mean orientation within each respective grain (b, d) of the same sample areas. Grain boundaries are defined as 10° misorientation, and are drawn as black lines.

III-3.2 Microstructure results

Forward scattered electron images of the starting material and representative deformed samples are shown in III.2 and representative maps of the misorientation to a reference point and to the mean of each respective grain are shown in Figure III-3. Data for samples not shown can be given upon request. Olivine comprises > 99.8 $\%_{area}$ of all samples, with diopside, enstatite and chromite as secondary phases (< 0.1 $\%_{area}$). Indexation rates range from 93.3 % to 98.7 % in the hot-pressed or deformed samples and 27.9 % to 41.3 % in the cold-pressed and powder samples. Grains in all samples are tabular, shorter in the compression direction, with a mean aspect ratio of 1.4 - 1.5 (d_{max}/d_{min}) and a maximum aspect ratio of 3.0 (Table III-1, Figure III-4a). The long axis of the grain is preferentially oriented at 180° to the compression axis (or vertical axis in case of the olivine powder) in all samples, as shown in Figure III-5. Grain boundaries, and part of the sub-grain boundaries, are curved or

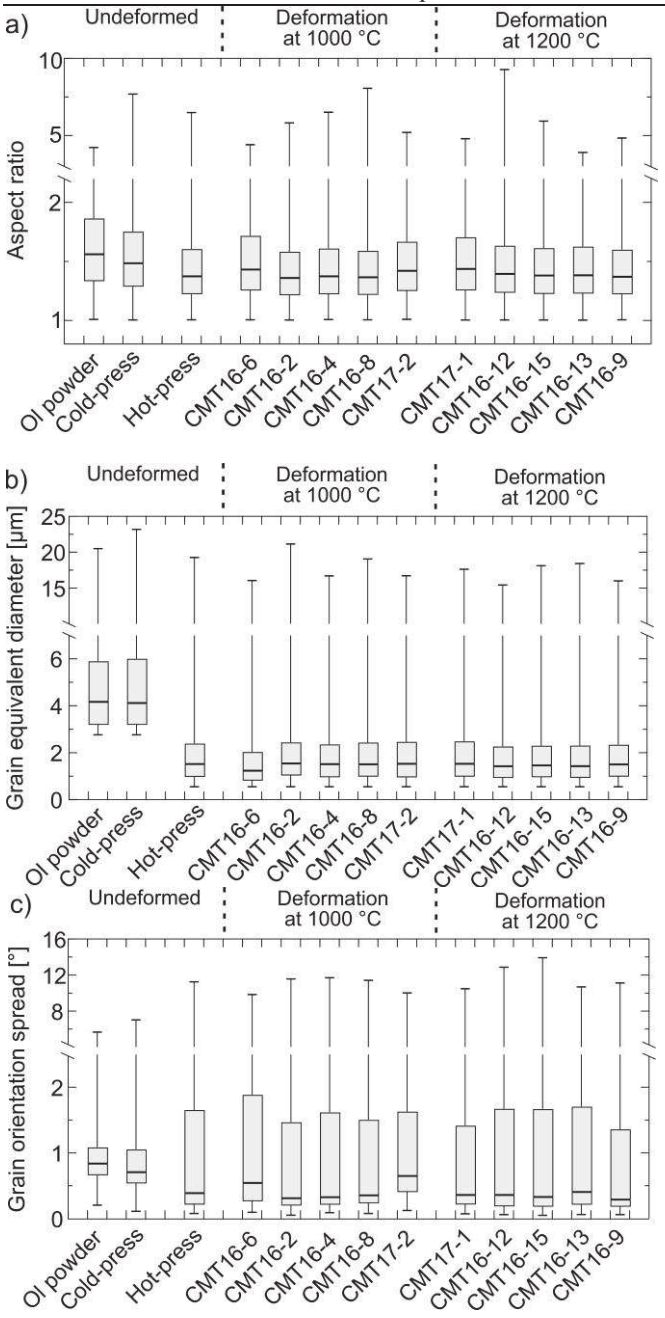

Fig. III-3 Distribution of the (a) equivalent grain diameter, (b) grain aspect ratio (d_{max}/d_{min}) and (c) grain orientation spread for each experiment. The whiskers represent the minimum and maximum values. The olivine powder and cold-press samples show apparent higher values due to higher EBSD step sized used for data acquisition (1 µm instead of 0.2 µm).

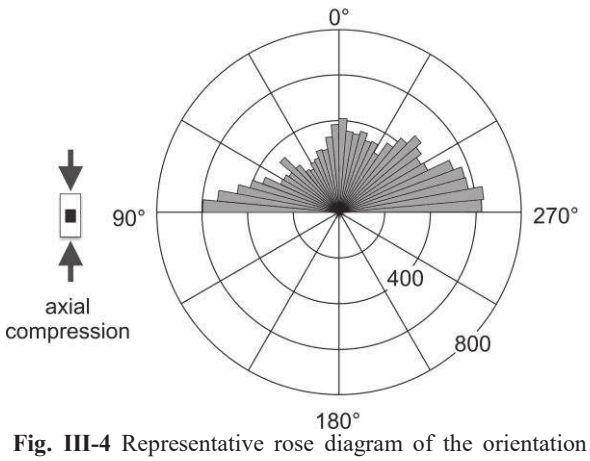

Fig. III-4 Representative rose diagram of the orientation of the longest axis of the olivine grains relative to the compression axis (sample CMT16-9). Olivine long axes are preferentially aligned perpendicular to the compression axis. The radius of the rose diagram gives counts, bins are 5°.

serrated. Grain internal misorientation occurs in all stages from gradual misorientation to well developed polygonization. Triple junctions are dominant, but apparent 4-grain junctions can be seen in several EBSD maps as well. BSE images reveal occasional cracks inside the grains that are oriented at 60° to each other. These rare cracks are already present in the olivine powder and there is no sign of displacement or sliding along them. Sample CMT17-2, deformed at 1000 °C to a finite strain of 7.3 % exhibits a higher density of cracks crossing several grains or on grain boundaries, indicating that CMT17-2 deformed by micro-cracking after reaching a peak stress of 1073 MPa. See Supplementary Figure S3 for SEM images of sample CMT17-2 showing grain-interior cracks and pairs of cracks at an angle of ~ 45 % to the compression axis. Porosity from plucking during sample polishing is higher in samples with shorter hot-press durations or lower hot-press temperatures (e.g. CMT16-5 and corresponding deformed sample CMT16-6). Excluding plug outs, porosity makes up less than 3 $\%_{area}$ as observed for similar experiments (Beeman & Kohlstedt, 1993; Hirth & Kohlstedt, 1995; Hansen et al., 2012).

Representative grain size distributions obtained using MTEX as the diameter of a circle with an area equivalent to the respective grain are shown in Figure III-6. The grain size distribution is similar for all samples, there is no significant change as a function of finite strain or temperature as shown by Figure III-4b. The mean equivalent diameter calculated from the log-normal distribution ranges from 1.4 ± 2.0 µm to 1.7 ± 2.0 µm (geometric mean, 1 σ) for the deformed samples and their respective hot-presses. The high geometric standard deviation reflects the broad distribution of grain sizes. The microstructure of the hot-pressed and deformed samples are identical to the one of the powder and cold-press samples, taking into account measurement errors and higher EBSD step sizes in the powder and cold-press. It is likely inherited from the original powder and shape preferred orientation due to sedimentation effects while loading the capsule. The grain shape is likely related to perfect cleavage of olivine on (010) (Deer et al, 1997; Hawkes, 1946; Velinskiy & Pinus, 1969; Kuroda & Shimoda, 1967; Kuijper, 1979) during pulverization.

Accounting for sectioning bias (factor of 1.5 for nonspherical olivine grains; Underwood, 1970), this equals a true mean grain diameter of 2.1-2.6 µm.

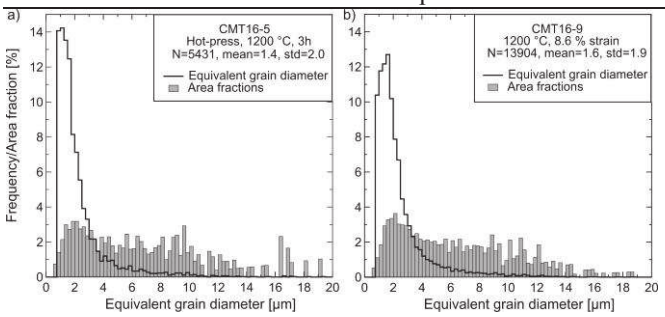

Fig. III-6 Representative grain size distribution of (a) a hot-pressed sample (CMT16-5), and (b) a sample deformed at 1200 °C to 8.6 % of strain. Grain sizes are calculated as the diameter of a circle with an equivalent area to the grain. N gives the number of grains used for the grain size calculation. The mean is calculated as the geometric mean.

Normalized by area, the distribution broadens with grains up to 27 µm in equivalent diameter taking up a sizeable fraction of the sample area. Due to the calculation method (i.e., only considering grains consisting of more than 5 pixels), the smallest grains have a equivalent diameter of 0.6 µm. For the cold-press and powder samples, a higher EBSD step size of 1 µm was used. Consequently, the average grain size appears to be higher, with 2.1 ± 1.9 µm for the olivine powder and 2.3 ± 1.9 µm for the cold-press (Table III-1).

All samples, including the undeformed olivine powder, show an axial [010] pattern of the texture, as shown in Figure 7. Crystal [100] and [001] axes are aligned in a girdle perpendicular to the compression axis, and [010] axes are parallel to the compression axis. The J-index (area weighted) ranges from 1.2 to 1.8, and is not changing significantly in between samples. Calculated for one mean orientation per grain, the J-index is slightly lower, ranging from 1.1 to 1.2.

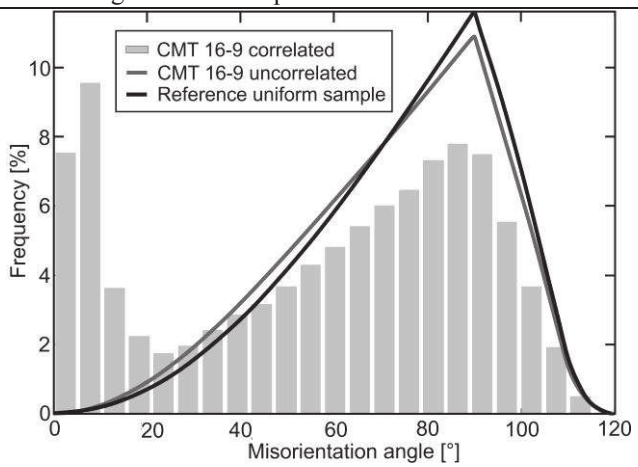

Fig. III-8 Representative histogram of the correlated, uncorrelated and uniform misorientation angles using a lower bound of 2°. Grey bars show boundaries in CMT 16-9. The black line is calculated for a uniform, randomly oriented sample. The grey line is calculated from uncorrelated measurement pixels (spaced apart) and can be compared to the uniform sample to estimate the texture influence, which is small here.

The frequency of grain boundaries as a function of their misorientation angle is displayed in Figure III-8. The given histogram (CMT16-9) is representative of all samples. We show the correlated misorientation angles (*i.e.*, from neighboring pixels). In MTEX, the uncorrelated misorientation angle distibution is calculated using the orientation distribution function (ODF) harmonic coefficients and only reflects the influence of the CPO and nothing else. The uniform misorientation angle distribution is calculated using the analytical method of Morawiec (2004). Note that a deviation of the uncorrelated angles from the uniform distribution therefore shows the influence of texture, while the distribution of the correlated angles depends on the occurence of deformation-related (sub)grain boundaries. The most commonly occuring low angle boundaries have

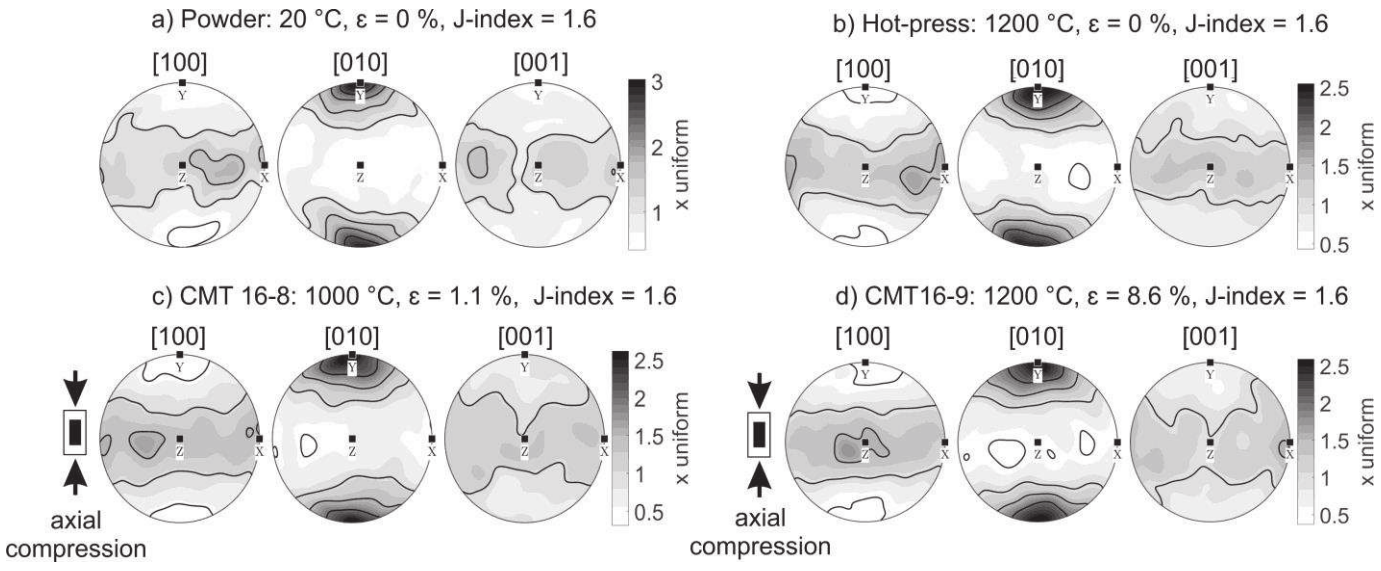

Fig. III-5 Lower hemisphere pole figures of the crystal preferred orientation for (a) the olivine powder; (b) a representative hot-pressed olivine sample; (c) the olivine sample deformed at 1000 °C (CMT16-8) and (d) the olivine sample with the highest finite strain deformed at 1200 °C (CMT16-9). The pole figures were calculated using one point per pixel.

misorientations of up to 20°, with a strong maximum at 10° (10 % frequency).

High angle boundaries increase in frequency towards a maximum at 90° (8 % frequency), resulting in a negatively skewed distribution. The uncorrelated misorientation angles match the uniform distribution, with only a higher frequency of angles below ~70° than in the random distribution. The misorientation from the mean within each grain is log-normal distributed with angles up to 15° as plotted in Figure III-9. The misorientation axis of these low-angle boundaries of up to 15° can be plotted in crystallographic coordinates. The resulting inverse pole figure, representative for the hot-pressed and deformed samples, is displayed in Figure III-10. Most misorientation axes are close to the crystallographic [001] direction with a strong maximum of 8 × uniform. There is a weak secondary concentration around the [010] direction. The distribution of the misorientation axes does not change significantly between samples deformed at 1000 °C and 1200 °C or as a function of finite strain.

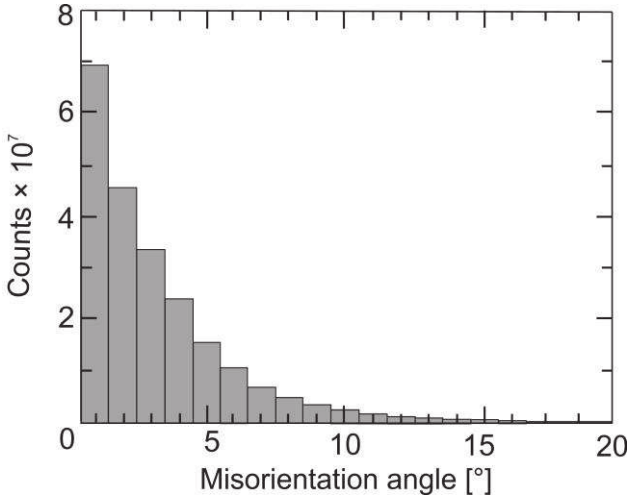

Figure III-9 Histogram of the misorientation to the mean within each respective olivine grain (CMT16-9). This distribution is representative of all samples. The misorientation is log-normal distributed with angles up to 16°.

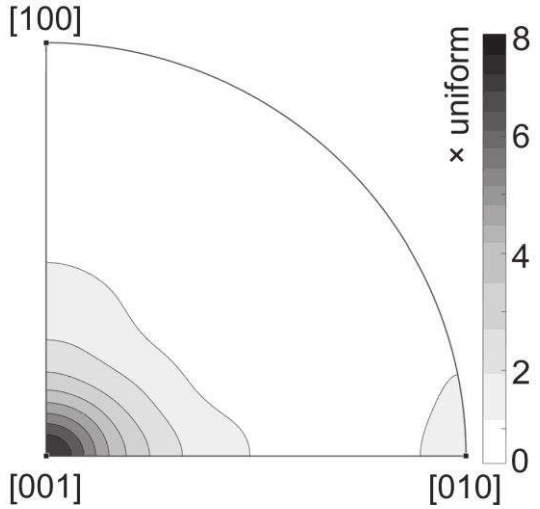

Figure III-10 Representative inverse pole figure of the misorientation axes of olivine grain boundaries in crystal coordinates for misorientation angles between 2 and 15°.

III-3.3 Transmission Electron Microscopy

Typical weak-beam dark-field TEM images of the dislocation microstructures are given in Figure III-11. All samples exhibit unambiguous dislocation activity. The most striking feature is the rather strong heterogeneity of the microstructures in all samples which does not allow a simple trend to be found among them. Even at the lowest temperatures considered (1000-1030 °C) both [100] and [001] dislocations activity is found (Fig. 11a, b) from quite small finite strains (1.41% in case of CMT16-2). Dislocation line shapes suggest high lattice friction, but dislocations already organize into subgrain boundaries. Even at the highest temperature considered (1200 °C) deformation is very heterogenous with some grains almost or completely pristine (Fig. 11c) and some other exhibiting dislocation densities of the order of 10^{14} m^{-2}. Several observations of grain boundaries acting as sources for dislocations have been found. The samples contain residual pores which do not appear to be sites where plasticity concentrates. In grains displaying evidence of [100] and [001] slip activity, there is no evidence of interaction between the dislocations from the different slip systems.

III-4. Discussion

III-4.1 Mechanical data

The maximum differential stresses of our experiments at 1000 °C exceed the confining pressure by a factor of up to 3.5. The confining pressure (P) acts by opposing volume expansion (*e.g.* Edmond & Paterson, 1972) and against crack nucleation and propagation. The Goetze criterion, first proposed by Briegel and Goetze (1978), defines a critical stress needed to initiate crack nucleation as σ_1-σ_3 = P (see also Kirby, 1980; Evans & Kohlstedt 1995). With the exception of CMT17-2, there is no evidence for displacement along cracks in SEM images of our samples. On the short time scales of our experiments, the Goetze criterion does not hold true.

For deformation experiments at 1000 °C, the present stress-strain curves are consistent when compared to previous mechanical results for polycrystalline olivine (900 °C, 300 MPa, 1×10^{-5} s^{-1} - 3×10^{-5} s^{-1}, axial compression, with correction for the apparatus stiffness) from Demouchy et al. (2014). The

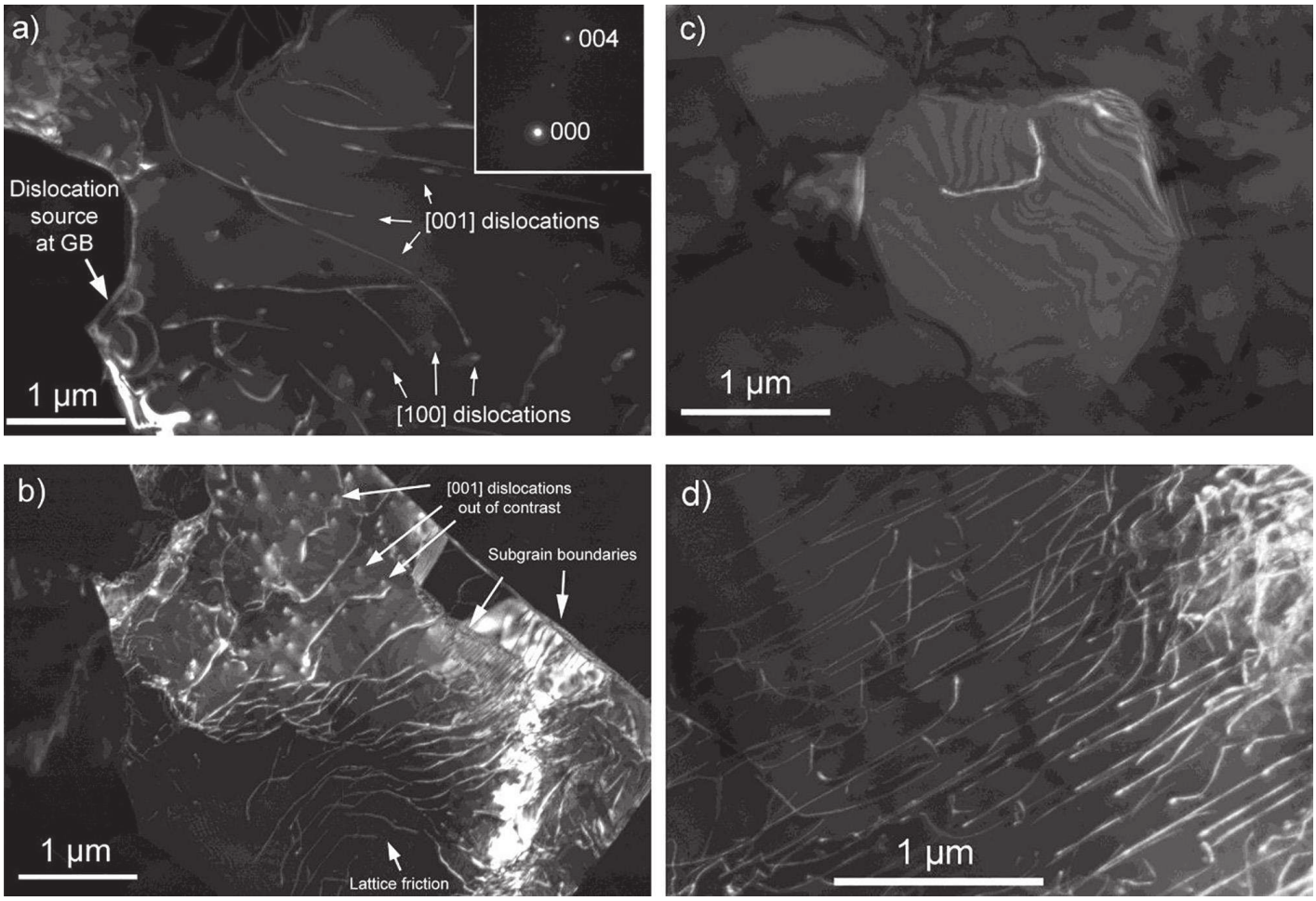

Fig. III-11 TEM weak-beam dark-field images of typical microstructures found in all samples. (a) Image from sample CMT16-2 showing a dislocation source at a grain boundary (diffraction vector g: 004). [001] dislocations are in contrast unless 100 dislocations for which only a residual contrast at the surface (white dots) can be seen. Both dislocation types are present. (b) Image from sample CMT16-8 displaying both [100] and [001] dislocations activity with the formation of subgrain boundaries (diffraction vector g: 004). [001] dislocations exhibit lattice friction. (c) Image from sample CMT16-9 showing a grain with almost no dislocation activity. (d) Image from sample CMT16-9 of a grain containing a dislocation density of $\approx 7\times10^{13}$ m^{-2}.

sample CMT17-2 of this study reaches brittle failure at a higher stress of 1127 MPa, while sample PoEM22 of Demouchy et al. (2014) fails at 930 MPa at 900 °C. Note that both CMT17-2 of this study and PoEM22 of Demouchy et al. (2014) did not reach steady state before brittle failure and thus give only a lower bound of strength. For a given strain, samples in this study reach a lower stress, consistent with deformation at higher temperatures. The maximum stresses from our experiments at 1000 °C and existing low temperature (exponentional) flow laws are shown in Figure III-12c. The maximum stress for 1.1 % of finite strain at 1000 °C (CMT16-8, no steady state or brittle failure) surpasses recent calculations based on 2.5-D dislocation dynamics models for single crystals of olivine oriented for easy slip (Boioli et al. 2015; their Figure III-3). In this study, they model a single glide direction, [100](001), in a olivine single crystal, therefore giving only a lower bound of the strength. The experiment CMT17-2 reached brittle failure around 3 % of finite strain, but the maximum stress before brittle failure of 1127 MPa can be used. The stress surpasses steady state estimations from the single crystal flow laws from Evans & Götze (1979) and Demouchy et al. (2013), but is in good agreement with the flow law based only on [001](100) glide from deformation experiments in shear from Tielke et al. (2016), as seen in Figure III-12. The higher strength of our samples can at least partly be attributed to the lack of sufficient independent slip systems in polycrystalline olivine samples (the so called olivine paradox) and the difference between single crystal and polycrystal rheology (*e.g.*, Evans and Goetze, 1979, their Fig 14).

The deformation curves of samples CMT16-13 and CMT16-9 obtained at 1200 °C (Figure III-12b) show a quasi-steady-state mechanical behavior. Their respective maximum stresses fit well with the

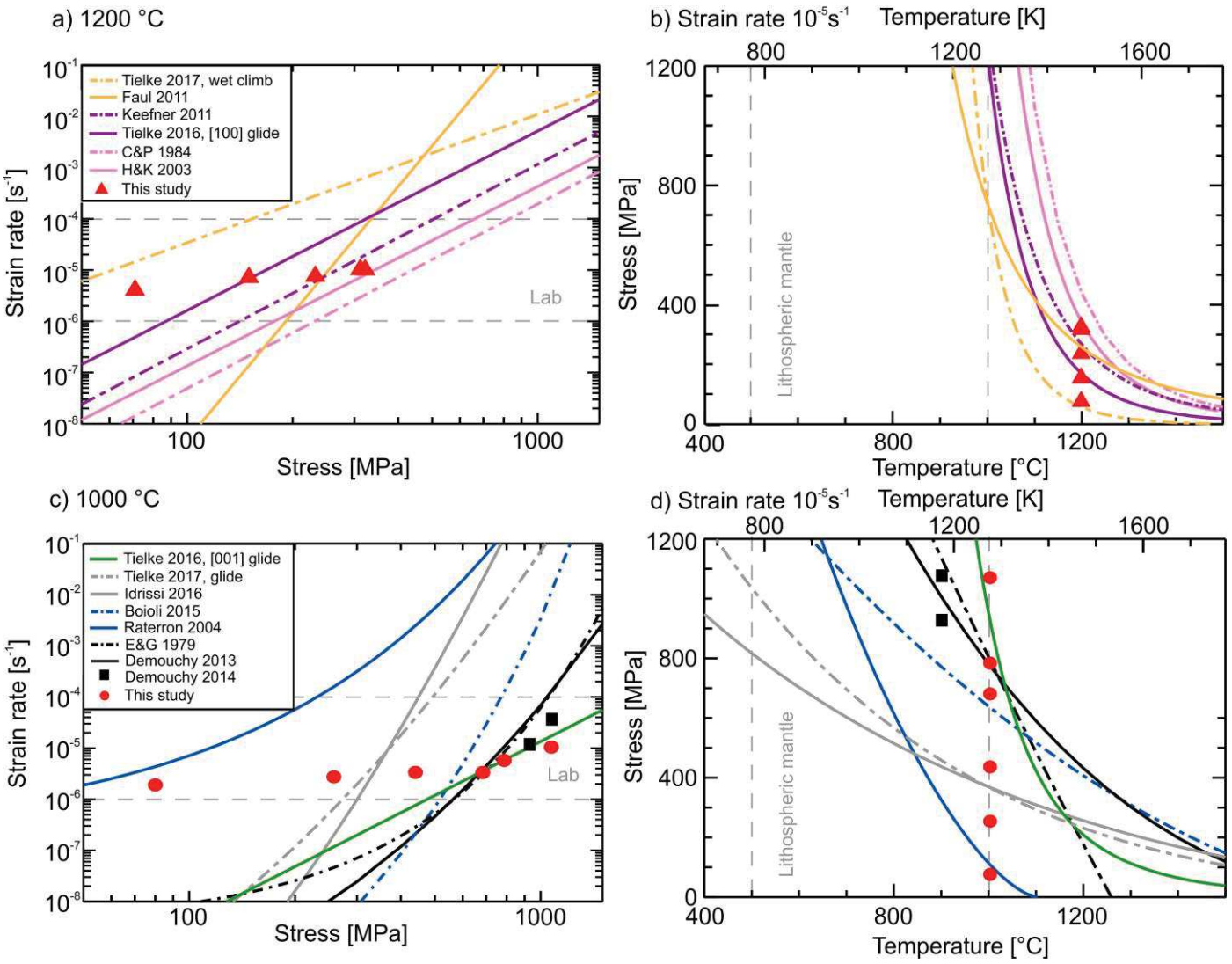

Fig. III-12 (a) Maximum stresses (red triangles) achieved for deformation at 1200 °C as a function of strain rate, compared to flow laws of previous studies. (b) Temperature-stress plot for deformation at 1200 °C. (c) Maximum stresses (red squares) achieved for deformation at 1000 °C as a function of strain rate, black squares are maximum stresses from Demouchy et al. (2014). (d) Temperature-stress plot for deformation at 1000 °C. Flow laws are from Evans & Goetze (1979), Chopra & Paterson (1984), Hirth & Kohlstedt (2003), Raterron et al. (2004), Faul et al. (2011), Keefner et al. (2011), Demouchy et al. (2013), Boioli et al. (2015), Idrissi et al. (2016), Tielke et al. (2016, shear on (100)[001] for 1000 °C and (001)[100] for 1200 °C) and Tielke et al. (2017, dry/wet glide for 1000 °C and wet climb for 1200 °C, 11-16 ppm H_2O wt. or 190-260 ppm H/10^6Si). The sample with the highest stress at 1000 °C (CMT17-2, 7.3 % strain) did not reach steady state and gives a lower bound of strength.

dislocation creep flow law for Âheim dunite from Keefner et al. (2011, grain size of 0.9 mm). The dislocation creep power law of Hirth & Kohlstedt (2003, using data from Mei and Kohlstedt, 2000b for dry conditions) and the dislocation creep flow law for dry dunites from Chopra and Paterson (1984) surpass the stresses reached in our samples deformed at high temperature by 100 MPa and 200 MPa respectively.

III-4.2 Deformation mechanisms & microstructure

While deformation is obviously plastic, one sample (CMT17-2) exhibits a higher density of cracks. Cracks generally exist in a subset of the grains in all samples, including the olivine powder, where they are more common and broader. They are therefore likely to be related to the powder preparation method of the olivine starting material (*i.e.*, fluid energy pulverization). The pulverisation might also explain the aspect ratio of 1.4-1.5 seen in all samples, since (010) planes are distinct cleavage planes in iron-rich olivine (Deer et al, 1997; Hawkes, 1946; Velinskiy & Pinus, 1969; Kuroda & Shimoda, 1967; Kuijper, 1979). During hot-pressing these cracks mostly healed. Sample CMT17-2 exhibits a higher density of cracks, which are paired with their acute angle (~60 °) orientated nearly parallel to the compression axis; opening grain boundaries, as well as crossing several grains. We conclude that the sample CMT17-2 deformed in the brittle field by micro fracturing for a strain > 3% (at 1127

MPa, where the cuve flattens abruptly), while the other samples underwent no brittle failure. Rigid body grain rotation cannot be observed, since the orientation of the long axis of the grains stays constant.

The main deformation mechanism can be identified from comparison of the mechanical data to published flow laws and the alignment of low-angle boundaries. The maximal stresses of our experiments match existing dislocation creep flow laws for temperatures > 1100 °C. Combined with the constant grain size, aspect ratio and TEM images, this suggests that dislocation creep was the dominant deformation mechanism, with a limited contribution of diffusion creep. The alignment of low-angle boundary misorientation axes parallel to the crystallographic [001] axis, shown in Figure III-10, is common for tilt walls composed of [100]{0kl} dislocations, while the weak concentration parallel to the [010] axis is common for tilt walls built from [001](hk0) dislocations (Nicolas et al. 1973; Wenk et al. 1991; Tommasi et al. 2008; Farla et al. 2011; Demouchy et al. 2013, 2014). However, the grain boundary misorientation axes obtained from EBSD maps only represent preserved geometrically necessary dislocations (GND's, i.e., dislocations contributing to the lattice curvature). Therefore, the slip systems active during deformation might differ slightly (Raleigh, 1965, 1967, 1968; Carter & Lallemant, 1970; Durham, 1975; Poirier, 1975; Tommasi et al., 2008; Soustelle et al., 2010; Demouchy et al. 2014). The distribution of grain boundary misorientation angles (Figure III-8) showing a peak at 90° is typical for a uniform distribution for orthorhombic crystal symmetry (Morawiec, 2004). The secondary peak at 10° matches well with observations from Marquardt et al. (2015), who investigated the grain boundary character distribution of undeformed synthetic and natural polycrystalline olivine.

The microstructures of the hot-pressed and deformed samples are identical. In particular, the distribution of deformation axes does not change in between hot-presses and experiments performed at 1000 °C and 1200 °C and as said above (4.2), it is due to perfect cleavage of olivine on (010) during powder preparation. The [100](001) slip system therefore seems not to be solely or preferentially activated in samples deformed at 1000 °C, compared to deformation at 1200 °C, which is consistent with experiments of Raleigh (1968) and Phakey et al. (1972). Likewise, the crystal preferred orientation (Figure III-7) does not change or increase in intensity, which is expected for low values of finite strains (Nicolas et al., 1973, Zhang & Karato, 1995; Skemer et al., 2012), and is confirmed here, even if high differential stresses are reached. We tried to hot-press an olivine aggregate for 20 h at 1270 °C (CMT17-3) and it produced only a limited grain growth to 2.8 µm and no significant reduction of dislocation density (as evidenced by the grain orientation spread and kernel average misorientation) or a change in texture (see J- and BA-index in Table III-2). To significantly alter the starting microstructure, much longer hot-press durations (> 100 h), a higher hot-press temperature (> 1300 °C) or an addition of water (drastic change of thermodynamic conditions) would be needed and these grain growth conditions are beyond the scope of this study.

III-4.3 Strain hardening during transient creep

We have two opposing observations, which question the current understanding of strain hardening in olivine. The stress during deformation rises nonlinearly as a function of finite strain before reaching steady state or brittle failure. This hardening is dependent on the deformation temperature and must therefore be based on a thermally activated process. Based on observations on metals, hardening is explained by competing effect of reduction of the grain size, and an increasing dislocation density in the neoformed sub-grains acting as obstacles and yielding an increasing sub-grain boundary misorientation (Estrin et al., 1998; Nes, 1997). Yet, the microstructure of our samples does not change with increasing stress or finite strain. Since none of these mechanisms seem to hold true during transient creep of our samples, the question of the mechanism of strain hardening in our sample remains. Thus, we discuss here several possibilities:

(i) *Dislocation interactions:* In metals, plastic strain hardening is commonly interpreted as the consequence of gliding dislocations interacting with the so-called forest dislocations (*i.e.* dislocations lying in different planes). This effect is reinforced by the possibility in most cubic metals that dislocation interaction can lead to stable junctions. In olivine, the two Burgers vectors [100] and [001] are perpendicular, which allows only rare and weak junctions (Mussi et al. 2017). Indeed, Fig. 11a,b shows no strong interactions between [100] and [001] glide. Other hardening mechanisms resulting from dislocation dynamics are collinear interaction and double cross slip. Our observations although preliminary, do not show more of these features in the low temperature samples.

(ii) Dislocation Mobility: In this temperature range, olivine is expected to involve significant lattice friction and this is supported by observation of the shapes of dislocation lines. However, here again, qualitative indication of lattice friction can be found in all samples (e.g. Fig11b, d). It is to be remembered that in the thermally activated regime, temperature enters an exponential and hence that a difference of 200 °C can lead to significant enhancement of dislocation mobility which could not be detected from post-mortem observations. This contribution can therefore not be excluded.

(iii) *Grain boundaries acting as obstacles*: In low-temperature plasticity, grain boundaries play mostly the role of obstacles leading to the well-known Hall-Petch effect

(Hansen, 2004; Louchet et al., 2006). With grain sizes of around 2 µm, the ratio of boundary area to grain volume is high. Therefore, the interaction of dislocations with grain boundaries might play a role by preventing easy transfer of plastic activity from grain to grain. The formation of pile-ups might cause sufficient back stresses to be a source of hardening. However, we did not observe more evidence for pile-ups in samples deformed at the lowest temperatures than at the highest temperature.

(iv) *Grain boundaries acting as dislocation sources*. For plastic deformation to proceed, dislocation multiplication mechanisms are necessary. Inside grains, multiplication is usually attributed to the operation of Frank-Read sources (Frank & Read, 1950), although they are rarely clearly observed. Our study follows this trend since we did not observe such sources. Instead, we observed several occurrences of dislocations being emitted from grain boundaries. We have no information about the ability of grain boundaries in olivine to act as dislocation sources and how temperature influences this mechanism. We note that the sources observed only produce a few loops. The hypothesis that dislocation nucleation represents a limiting factor in this temperature range cannot be further established or discarded.

(v) *Grain boundaries acting as agent of deformation*. Dislocation activity might not be the only deformation mechanism acting and in the recent years, a growing body of evidence has lead to establish grain boundary processes as a contribution to creep of olivine aggregates. This is most often attributed to the so-called grain boundary sliding mechanism (*i.e.*, relative tangential motion of adjacent grains parallel to their common boundary; e.g. Hirth & Kohlstedt, 1995; Langdon, 2006 ; Hansen et al. 2011) although other mechanisms described as shear-induced boundary migration, possibly involving disclinations, have also been proposed (Cordier et al., 2014). Grain boundary sliding was proposed to be active under high stresses and moderate to low homologous temperatures in olivine (T_m of Fo90 = 1765 °C, Bowen & Schairer, 1935; Wang, 2016) but also at temperatures very close to melting temperature and for a restricted type of tilt boundaries (e.g., in gold, Cahn et al., 2006). Without suitable markers (*i.e.*, grid or dot-array of deposited metal or electron engraving, Quintanilla-Terminel et al., 2017), we cannot determine if these mechanisms were more active at 1200 °C than at lower temperatures.

III-4.4 Implications for the uppermost mantle

Temperature conditions in our experiments (*i.e.,* 1000 °C) correspond to the uppermost lithospheric mantle, just below the Mohorovičić-Discontinuity. This layer acts as an imperfect mechanical boundary between the convecting mantle and the lithospheric plates. The maximum stresses obtained by our samples at 1000 °C surpass predictions from existing flow laws for this temperature domain (exponential law), but are indeed significantly lower than prediction deduced from high temperature flow laws (power law), without the intervention of additional weakening mechanism such as water weakening (*e.g.*, Mackwell et al., 1985; Demouchy et al., 2012) or partial melting (*e.g.*, Kohlstedt & Zimmerman, 1996). In consequence, the strength of olivine-rich rocks deformed at a temperature of 1000 °C and below, are in the order of 0.5 to 1 GPa when extrapolated at the strain rate of the mantle (*e.g.* 10^{-14} s^{-1}) which matches the requirement of a not so soft lithospheric mantle, ables to upkeep large orogens for millions of years (*e.g.*, Mouthereau et al., 2013).

III-5 Conclusions

- Deformation at 1000 °C surpasses predictions from most previous low-temperature flow laws, but is in good agreement with Tielke et al. (2016, shear on [001](100)).
- Deformation at 1200 °C is in good agreement with Keefner et al. (2011), Tielke et al. (2016, shear on [100](001)) and Hirth and Kohlstedt (2003).
- The non-linear dependence of stress on finite strain (hardening) during early stage deformation is not correlated to a change in statistical microstructure measured by several parameters or texture strength and symmetry using EBSD maps.
- The samples with constant statistical microstructure however have a strength that is sensitive to finite strain, temperature and strain rate in a similar way to previously reported flow laws.
- The achieved stresses, constant grain sizes and absence of grain shape change fit well to dislocation creep as the main deformation mechanism. Grain boundary mechanisms would suggest a lower strength than observed.
- Glide on [100](0kl) is dominant, as evidenced by the alignment of low-angle boundaries parallel to the crystallographic [001] direction.
- Even at early steady state (at 1200 °C) and stresses of up to 1073 MPa, a sizeable subset of grains remains free of misorientation, which could be related to the small grain size.
- We further confirm that flow laws obtained at temperatures > 1200 °C cannot predict the strength of olivine deformed at 1000 °C. The observed microstructures cannot explain the change in viscosity.

Acknowledgements

This project received funding from the European Union's Horizon 2020 research and innovation program under the Marie Sklodowska-Curie grant agreement No. 642029. We thank C. Nevado and D. Delmas for providing high-quality thin sections for SEM and TEM. N. Marino and J. Oustry are sincerely thanked for their help in the high-pressure lab and in the mechanical workshop. The TEM and EBSD-SEM national facilities in Lille and Montpellier are supported by the Institut National de Sciences de l'Univers (INSU) du Centre National de la Recherche Scientifique (CNRS, France), the Conseil Régional Occitanie/Pyrénées-Méditerranée (France), and by the Conseil Régional du Hauts-de-France, (France).

References

Bachmann, F., Hielscher, R., Schaeben, H., 2010. Texture analysis with MTEX – Free and open source software toolbox. Solid State Phenom. 160, 63–68. http://dx.doi.org/10.4028/www.scientific.net/SSP.160.63.

Bai, Q., Mackwell, S.J. & Kohlstedt, D.L., 1991. High-temperature creep of olivine single crystals - 1. Mechanical results for buffered samples. J. Geophys. Res. 96(B2), 2441-63.

Bai, Q., Kohlstedt, D.L., 1992. High-temperature creep of olivine single crystals, 2. dislocation structures. Tectonophysics 206, 1–29. http://dx.doi.org/10.1016/0040-1951(92)90365-D.

Beausir, B., Fressengeas, C., 2013. Disclination densities from EBSD orientation mapping. Int. J. Solids Struct. 50, 137–146. http://dx.doi.org/10.1016/j.ijsolstr.2012.09.016.

Beeman, M.L., Kohlstedt, D.L., 1993. Deformation of fine-grained aggregates of olivine plus melt at high temperatures and pressures. J. Geophys. Res. 98, 6443–6452. http://dx.doi.org/10.1029/92JB02697.

Boioli, F., Carrez, P., Cordier, P., Devincre, B., Marquille, M., 2015. Modeling the creep properties of olivine by 2.5-dimensional dislocation dynamics simulations. Phys. Rev. B 92, 1–12. http://dx.doi.org/10.1103/PhysRevB.92.014115.

Bowen, N.L., Shairer, J.F., 1935. The System MgO-FeO-SiO_2. Am. J. Sci. 29, 151–217.

Briegel, U., Goetze, C., 1978. Estimates of differential stress recorded in the dislocation structure of Lochseiten Limestone (Switzerland). Tectonophysics 48(1-2), 61-76. http://dx.doi.org/10.1016/0040-1951(78)90086-0.

Buening, D.K., Buseck, P.R., 1973. Fe-Mg lattice diffusion in olivine. J. Geophys. Res. 78, 6852–6862. http://dx.doi.org/10.1029/JB078i029p06852.

Bunge, H.-J., 1982. Texture Analysis in Materials Science. Butterworths, London, p. 593. http://dx.doi.org/10.1016/B978-0-408-10642-9.50019-2.

Cahn, J.W., Mishin, Y., Suzuki, A., 2006. Coupling grain boundary motion to shear deformation. Acta Mater. 54, 4953–4975. http://dx.doi.org/10.1016/j.actamat.2006.08.004.

Carter, N.L. & Avé Lallemant, H.G., 1970. High temperature deformation of dunite and peridotite. Geol. Soc. Am. Bull. 81, 2181-202.

Chakraborty, S., 2010. Diffusion coefficients in olivine, wadsleyite and ringwoodite. Rev. Mineral. Geochemistry 72, 603–639. http://dx.doi.org/10.2138/rmg.2010.72.13.

Chen, S., Hiraga, T. & Kohlstedt, D.L., 2006. Water weakening of clinopyroxene in the dislocation creep regime. J. Geophys. Res. 111(B8), 2156-202.

Chopra, P.N., Paterson, M.S., 1981. The experimental deformation of dunite. Tectonophysics 78, 453–473. http://dx.doi.org/10.1016/0040-1951(81)90024-X.

Chopra, P.N., Paterson, M.S., 1984. The role of water in the deformation of dunite. J. Geophys. Res. 89, 7861–7876. http://dx.doi.org/10.1029/JB089iB09p07861.

Cooper, R.F., Kohlstedt, D.L., 1984. Solution-precipitation enhanced diffusional creep of partially molten olivine-basalt aggregates during hot-pressing. Tectonophysics 107, 207–233. http://dx.doi.org/10.1016/0040-1951(84)90252-X.

Cooper, R.F., Kohlstedt, D.L., 1986. Rheology and structure of olivine-basalt partial melts. J. Geophys. Res. 91, 9315. http://dx.doi.org/10.1029/JB091iB09p09315.

Cordier, P., Demouchy, S., Beausir, B., Taupin, V., Barou, F., Fressengeas, C., 2014. Disclinations provide the missing mechanism for deforming olivine-rich rocks in the mantle. Nature 507, 51–6. http://dx.doi.org/10.1038/nature13043.

Deer, W.A., Howie, R.A., Zussmann, J., 1997. Rock forming minerals: Orthosilicates. Vol. 1A Geological Society of London, London, p.187.

Demouchy, S., 2010. Diffusion of hydrogen in olivine grain boundaries and implications for the survival of water-rich zones in the Earth's mantle. Earth Planet. Sci. Lett. 295, 305–313. http://dx.doi.org/10.1016/j.epsl.2010.04.019.

Demouchy, S., Schneider, S.E., Mackwell, S.J., Zimmerman, M.E., Kohlstedt, D.L., 2009. Experimental deformation of olivine single crystals at lithospheric temperatures. Geophys. Res. Lett. 36, L04304. http://dx.doi.org/10.1029/2008GL036611.

Demouchy, S., Tommasi, A., Barou, F., Mainprice, D., Cordier, P., 2012. Deformation of olivine in torsion under hydrous conditions. Phys. Earth Planet. Inter. 202–203, 56–70. http://dx.doi.org/10.1016/j.pepi.2012.05.001.

Demouchy, S., Tommasi, A., Ballaran, T.B. & Cordier, P., 2013. Low strength of Earth's uppermost mantle inferred from tri-axial deformation experiments on dry olivine crystals. Phys. Earth Plan. Inter., 220, 37-49.

Demouchy, S., Mussi, A., Barou, F., Tommasi, A., Cordier, P., 2014. Viscoplasticity of polycrystalline olivine experimentally deformed at high pressure and 900°C. Tectonophysics 623, 123–135. http://dx.doi.org/10.1016/j.tecto.2014.03.022.

Demouchy, S., Bolfan-Casanova, N., 2016. Distribution and transport of hydrogen in the lithospheric mantle: A

review. Lithos. 240-243, 402-425. http://dx.doi.org/10.1016/j.lithos.2015.11.012.

Durham, W.B., 1975. Plastic flow of single-crystal olivine. Ph.D. Thesis, Dep. of Earth and Planet. Sci., Mass. Inst. of Technol., Cambridge, USA.

Durham, W.B., Goetze, C., Blake, B., 1977. Plastic flow of oriented single crystals of olivine. J. Geophys. Res. 82, 5755–5770.

Edmond, J.M., Paterson, M. S., 1972. Volume changes during the deformation of rocks at high pressure. Int. J. Rock Mech. and Mining Sci. 9, 161-182.

Estrin, Y., Tóth, L.S., Molinari, A., Bréchet, Y., 1998. A dislocation-based model for all hardening stages in large strain deformation. Acta Mater. 46, 5509–5522. http://dx.doi.org/10.1016/S1359-6454(98)00196-7.

Evans, B., Goetze, C., 1979. The temperature variation of hardness of olivine and its implication for polycrystalline yield stress. J. Geophys. Res. 84, 5505–5524.

Evans, B., Kohlstedt, D.L., 1995. Rheology of rocks. in: Ahrens, T. J. (ed.): Rock physics and phase relations: A handbook of physical constants, AGU Ref. Shelf 3, 148-165.

Farla, R.J.M., Kokkonen, H., Gerald, J.D.F., Barnhoorn, A., Faul, U.H., Jackson, I., 2011. Dislocation recovery in fine-grained polycrystalline olivine. Phys. Chem. Miner. 38, 363–377. http://dx.doi.org/10.1007/s00269-010-0410-3.

Faul, U.H., Fitz Gerald, J.D., Farla, R.J.M., Ahlefeldt, R., Jackson, I., 2011. Dislocation creep of fine-grained olivine. J. Geophys. Res. 116, B01203. http://dx.doi.org/10.1029/2009JB007174.

Faul, U.H., Cline, C. J. II, David, E. C., Berry A. J., Jackson, I., 2016. Titanium-hydroxyl defect-controlled rheology of the Earth's upper mantle. Earth Planet. Sci. Lett., 452, 227-237.

Faul, U. H., Cline, C. J., Andrew, I. I., Ian, B., & Gordana, J. (2017). Constraints on oxygen fugacity within metal capsules. Physics and Chemistry of Minerals. http://doi.org/10.1007/s00269-017-0937-7

Fei, H., Wiedenbeck, M., Yamazaki, D., Katsura, T., 2013. Small effect of water on upper-mantle rheology based on silicon self-diffusion coefficients. Nature 498, 213–215. http://dx.doi.org/10.1038/nature12193.

Frank, F. C., Read, Jr. W. T., 1950. Multiplication Processes for Slow Moving Dislocations. Phys. Rev. 79 (4): 722–723. doi:10.1103/PhysRev.79.722.

Frey, F.A., Prinz, M., 1978. Ultramafic inclusions from san carlos, Arizona: Petrologic and geochemical data bearing on their petrogenesis. Dev. Petrol. 5, 129–176. http://dx.doi.org/10.1016/B978-0-444-41658-2.50013-4.

Friedel, G., 1922. The mesomorphic states of matter, in: Annales de Physique. 18, 273–474. http://dx.doi.org/10.1201/9780203022658.ch1b.

Frost, H.J. & Ashby, M.F., 1982. Deformation mechanism maps: the plasticity and creep of metals and ceramics. Oxford: Pergamon Press.

Frost, D. J., & Mccammon, C. A. (2008). The Redox State of Earth' s Mantle. Annu. Rev. Earth Planet. Sci. 36, 389-420. http://doi.org/10.1146/annurev.earth.36.031207.124322

Frank, F.C., 1958. I. Liquid crystals. On the theory of liquid crystals. Discuss. Faraday Soc. 25, 19. http://dx.doi.org/10.1039/df9582500019.

Girard, J., Chen, J., Raterron, P., & Holyoke, C. W. (2013). Hydrolytic weakening of olivine at mantle pressure : Evidence of [100](010) slip system softening from single-crystal deformation experiments. Physics of the Earth and Planetary Interiors, 216, 12–20. http://dx.doi.org/10.1016/j.pepi.2012.10.009.

Goetze, C., 1978. Creep of engineering materials and of the Earth - The mechanisms of creep in olivine. Philos. Trans. R. Soc. London. A., 288, 99-119.

Goetze, C., Evans, B., 1979. Stress and temperature in the bending lithosphere as constrained by experimental rock mechanics. Geophys. J. R. Astron. Soc. 59, 463–478. http://dx.doi.org/10.1111/j.1365-246X.1979.tb02567.x.

Gribb, T.T., Cooper, R.F., 1998. A high-temperature torsion apparatus for the high-resolution characterization of internal friction and creep in refractory metals and ceramics: Application to the seismic-frequency, dynamic response of Earth's upper mantle. Rev. Sci. Instrum. 69, 559–564. http://dx.doi.org/10.1063/1.1148694.

Griggs, D.T., Turner, F.J., Heard, H.C., 1960. Deformation of rocks at 500° to 800°C. GSA Mem. 79, 39–104. http://dx.doi.org/10.1130/MEM79.

Gueguen, Y., Nicolas, A., 1980. Deformation of mantle rocks. Annu. Rev. Earth Planet. Sci. 8, 119–144. http://dx.doi.org/10.1146/annurev.ea.08.050180.001003.

Hansen, N., 2004. Hall-Petch relation and boundary strengthening, Scripta Mater. 51, 801-806.doi:10.1016/j.scriptamat.2004.06.002

Hansen, L.N., Zimmerman, M.E., Kohlstedt, D.L., 2011. Grain boundary sliding in San Carlos olivine : Flow law parameters and crystallographic - preferred orientation 116, 1–16. http://dx.doi.org/10.1029/2011JB008220.

Hansen, L.N., Zimmerman, M.E., Dillman, A.M., Kohlstedt, D.L., 2012. Strain localization in olivine aggregates at high temperature: A laboratory comparison of constant-strain-rate and constant-stress boundary conditions. Earth Planet. Sci. Lett. 333–334, 134–145. http://dx.doi.org/10.1016/j.epsl.2012.04.016.

Hawkes, H.E.J., 1946. Olivine from northern California showing perfect cleavage. Am. Mineral. 31, 276–283.

Hielscher, R., Schaeben, H., 2008. A novel pole figure inversion method: Specification of the MTEX algorithm. J. Appl. Crystallogr. 41, 1024–1037. http://dx.doi.org/10.1107/S0021889808030112.

Hiraga, T., Miyazaki, T., Tasaka, M., Yoshida, H., 2011. Mantle superplasticity and its self-made demise. Nature, 468, 1091-1094.

Hirth, G., Kohlstedt, D.L., 1995. Experimental constraints on the dynamics of the partially molten upper mantle: Deformation in the diffusion creep regime. J. Geophys. Res. 100, 15441–15449. http://dx.doi.org/10.1029/94JB02128.

Hirth, G. & Kohlstedt, D.L., 1996. Water in the oceanic upper mantle: implications for rheology, melt extraction and the evolution of the lithosphere. Earth Planet. Sci. Lett., 144, 93-108.

Hirth, G. & Kohlstedt, D.L., 2003. Rheology of the upper mantle and the mantle wedge: a view from the experimentalists. In J. Eiler, ed. Inside the Subduction Factory. Washington, DC: American Geophysical Union. pp.83-105.

Hutchinson, J.W., 1977. Creep and plasticity of hexagonal polycrystals as related to single crystal slip. Metall. Trans. A 8, 1465–1469. http://dx.doi.org/10.1007/BF02642860.

Idrissi, H., Bollinger, C., Boioli, F., Schryvers, D., Cordier, P., 2016. Low-temperature plasticity of olivine revisited with in situ TEM nanomechanical testing. Sci. Adv. 2, e1501671. http://dx.doi.org/10.1126/sciadv.1501671.

Jung, H., Karato, S.-i., 2001. Water-induced fabric transitions in olivine. Science. 293, 1460–1463. http://dx.doi.org/10.1126/science.1062235.

Karato, S.-i., Paterson, M.S. & Fitzgerald, J.D., 1986. Rheology of synthetic olivine aggregates: influence of grain size and water. J. Geophys. Res. 91, 8151-76.

Karato, S.-i., Wu, P., 1993. Rheology of the Upper Mantle: A synthesis. Science (80). 260, 771–778. http://dx.doi.org/10.1126/science.260.5109.771.

Karato, S.-i., Riedel, M.R., Yuen, D.A., 2001. Rheological structure and deformation of subducted slabs in the mantle transition zone: Implications for mantle circulation and deep earthquakes. Phys. Earth Planet. Int. 127, 83–108. http://dx.doi.org/10.1016/S0031-9201(01)00223-0.

Katayama, I., Jung, H., Karato, S.I., 2004. New type of olivine fabric from deformation experiments at modest water content and low stress. Geology 32, 1045–1048. http://dx.doi.org/10.1130/G20805.1.

Keefner, J.W., Mackwell, S.J., Kohlstedt, D.L., Heidelbach, F., 2011. Dependence of dislocation creep of dunite on oxygen fugacity: Implications for viscosity variations in Earth's mantle. J. Geophys. Res. 116, 1–15. http://dx.doi.org/10.1029/2010JB007748.

Kirby, S.H., 1980. Tectonic stresses in the lithosphere: constraints provided by the experimental deformation of rocks. J. Geophys. Res. 85, 6353–6363. http://dx.doi.org/10.1029/JB085iB11p06353.

Kohlstedt, D. L., Zimmermann, M. E., 1996. Rheology of partially molten mantle rocks. Annu. Rev. Earth Planet. Sci., 24, 41-62.

Kuijper, R.P., 1979. Olivine with perfect cleavage. Neues Jahrb. Miner. Monatshefte 10–16.

Kuroda, Y., Shimoda, S., 1967. Olivine with well-developed cleavages: its geological and minerological meanings. J. Geol. Soc. Japan 73, 377–388. http://dx.doi.org/10.5575/geosoc.73.377.

Liu, W., Kung, J., Li, B., 2005. Elasticity of San Carlos olivine to 8 GPa and 1073 K, Geophys. Res. Lett., L16301, doi:10.1029/2005GL023453.

Louchet, F., Weiss, J., Richeton, T., 2006. Hall-Petch Law Revisited in Terms of Collective Dislocation Dynamics. Phys. Rev. Lett., 97, 075504.

Mackwell, S., 2008. Rheological consequences of redox state. Rev. Mineral. Geochemistry 68, 555–569. http://dx.doi.org/10.2138/rmg.2008.68.20.

Mackwell, S.J., Kohlstedt, D.L., Paterson, M.S., 1985. The role of water in the deformation of olivine single crystals. J. Geophys. Res. 90, 11319. http://dx.doi.org/10.1029/JB090iB13p11319.

Mainprice, D., Bachmann, F., Hielscher, R., Schaeben, H. (2014) Descriptive tools for the analysis of texture projects with large datasets using MTEX: strength, symmetry and components. In: Faulkner, D. R., Mariani, E. & Mecklenburgh, J. (eds) Rock Deformation from Field, Experiments and Theory: A Volume in Honour of Ernie Rutter. Geological Society, London, Special Publications, 409, http://dx.doi.org/10.1144/SP409.8.

Mei, S., Kohlstedt, D., 2000a. Influence of water on plastic deformation of olivine aggregates 1 . Diffusion creep regime. J. Geophys. Res. 105, 21457–21469.

Mei, S., Kohlstedt, D.L., 2000b. Influence of water on plastic deformation of olivine aggregates 2. Dislocation creep regime. J. Geophys. Res. 105, 21471–21481.

Mei, S., Suzuki, A.M., Kohlstedt, D.L., Dixon, N.A., Durham, W.B., 2010. Experimental constraints on the strength of the lithospheric mantle. J. Geophys. Res. 115, 1–9. http://dx.doi.org/10.1029/2009JB006873.

Marquardt, K., Rohrer, G.S., Morales, L., Rybacki, E., Marquardt, H., Lin, B., 2015. The most frequent interfaces in olivine aggregates: the GBCD and its importance for grain boundary related processes. Contrib. Mineral. Petrol. 170, 40 http://dx.doi.org/10.1007/s00410-015-1193-9.

Mises, R. v., 1928. Mechanik der plastischen Formänderung von Kristallen. Zeitschrift Angew. Math. Mech. 8, 161–185.

Miyazaki, T., Sueyoshi, K., Hiraga, T., 2013. Olivine crystals align during diffusion creep of Earth's upper mantle. Nature, 502, 321-326.

Moosbrugger, C., 2002. Representation of stress-strain behavior. In: Tamarin, Y. (ed) Atlas of Stress-Strain Curves, ASM Int., Materials Park, Ohio, 2nd ed., 1-20

Morawiec, A., 2004. Orientations and rotations - computations in crystallographic textures. Springer Berlin Heidelberg, Berlin. pp.200.

Mouthereau, F., Watts, A.W., Burov E., 2013. Structure of orogenic belts controlled by
lithosphere age. Nature Geosciences, 6, 785-789, doi: 10.1038/NGEO1902

Mussi, A., Cordier, P., Demouchy, S., Hue, B. 2017. Hardening mechanisms in olivine single crystal deformed at 1090 °C: an electron tomography study. Phil. Mag., http://dx.doi.org/10.1080/14786435.2017.1367858.

Nes, E., 1997. Modelling of work hardening and stress saturation in FCC metals. Prog. Mater. Sci. 41, 129–193. http://dx.doi.org/10.1016/S0079-6425(97)00032-7.

Nicolas, A., 1986. Structure and petrology of peridotites: Clues to their geodynamic environment. Rev. Geophys., 24, 875-895. http://dx.doi.org/10.1029/RG024i004p00875.

Nicolas, A., Boudier, F., Boullier, A. M., 1973. Mechanisms of flow in naturally and experimentally deformed peridotites. Am. J. Sci. 273, 853–876. http://dx.doi.org/10.2475/ajs.273.10.853.

Nicolas, A., Poirier, J.P., 1976. Crystalline plasticity and solid state flow in metamorphic rocks, selected topics

in geological sciences series. London and New York, John Wiley & Sons, 976, p. 246.
Paterson, M.S., 1990. Rock deformation experimentation. Geophys. Monograph, 56, 187-194.
Phakey, P., Dollinger, G., Christie, J., 1972. Transmission electron microscopy of experimentally deformed olivine crystals, in: Heard, H.C., Borg, I.Y., Carter, N.L., Raleigh, C.B. (Eds.), Flow and Fracture of Rocks. Geophys. Monogr. Ser., Washington, D.C., 16, 117-129.
Poirier, J.-P., 1975. On the slip systems of olivine. J. Geophys. Res. 80, 4059–4061. http://dx.doi.org/10.1029/JB080i029p04059.
Proietti, A., Bystricky, M., Guignard, J., Béjina, F., Crichton, W., 2016. Effect of pressure on the strength of olivine at room temperature. Phys. Earth Planet. Inter. 259, 34–44. http://dx.doi.org/10.1016/j.pepi.2016.08.004.
Quintanilla-Terminel, A., Zimmerman, M.E., Evans, B. and Kohlstedt, D.L. (2017) Microscale and nanoscale strain mapping techniques applied to creep of rocks. Solid Earth, 8, 751-765
Raleigh, C.B., 1965. Glide mechanisms in experimentally deformed minerals. Science 150, 739–741. http://dx.doi.org/10.1126/science.150.3697.739.
Raleigh, C.B., 1967. Plastic deformation of upper mantle silicate minerals. Geophys. J. R. Astron. Soc. 14, 45–49. http://dx.doi.org/10.1111/j.1365-246X.1967.tb06220.x.
Raleigh, C.B., 1968. Mechanisms of plastic deformation of olivine. J. Geophys. Res. 73, 5391. http://dx.doi.org/10.1029/JB073i016p05391.
Raterron, P., Wu, Y., Weidner, D.J., Chen, J., 2004. Low-temperature olivine rheology at high pressure. Phys. Earth Planet. Inter. 145, 149–159. http://dx.doi.org/10.1016/j.pepi.2004.03.007.
Skemer, P., Warren, J.M., Hirth, G., 2012. The influence of deformation history on the interpretation of seismic anisotropy. Geochemistry, Geophys. Geosystems 13, Q03006. http://dx.doi.org/10.1029/2011GC003988.
Soustelle, V., Tommasi, A., Demouchy, S., Ionov, D.A., 2010. Deformation and fluid-rock interaction in the supra-subduction mantle: Microstructures and water contents in peridotite xenoliths from the Avacha volcano, Kamchatka. J. Petrol. 51, 363–394. http://dx.doi.org/10.1093/petrology/egp085.
Tommasi, A., Tikoff, B., Vauchez, A., 1999. Upper mantle tectonics: Three-dimensional deformation, olivine crystallographic fabrics and seismic properties. Earth Planet. Sci. Lett. 168, 173–186. http://dx.doi.org/10.1016/S0012-821X(99)00046-1.
Tommasi, A., Vauchez, A., Ionov, D.A., 2008. Deformation, static recrystallization, and reactive melt transport in shallow subcontinental mantle xenoliths (Tok Cenozoic volcanic field, SE Siberia). Earth Planet. Sci. Lett. 272, 65–77. http://dx.doi.org/10.1016/j.epsl.2008.04.020.
Tommasi, A., Baptiste, V., Vauchez, A., Holtzman, B., 2016. Deformation, annealing, reactive melt percolation, and seismic anisotropy in the lithospheric mantle beneath the southeastern Ethiopian rift: Constraints from mantle xenoliths from Mega. Tectonophysics 682, 186–205. http://dx.doi.org/10.1016/j.tecto.2016.05.027.
Tielke, J.A., Zimmerman, M.E., Kohlstedt, D.L., 2016. Direct shear of olivine single crystals. Earth Planet. Sci. Lett. 455, 140–148. http://dx.doi.org/10.1016/j.epsl.2016.09.002
Tielke, J.A., Zimmerman, M.E., Kohlstedt, D.L., 2017. Hydrolytic weakening in olivine single crystals. J. Geophys. Res. 122, 3465–3479. http://dx.doi.org/10.1002/2017JB014004
Turner, F.J., 1942. Preferred orientation of olivine crystals in peridotites, with special reference to New Zealand examples. Trans. R. Soc. New Zeal. 72, 280-300.
Underwood, E.E., 1970. Quantitative stereology. Reading, Mass., Addison-Wesley Pub. Co. p. 274.
Velinskiy, V. V., Pinus, G. V., 1969. Olivines with perfect cleavages in ultrabasite of Chukotok. Docklady Academy of Sciences of the USSR Earth Science Sections (English translation edition) 185, 99–101.
Wang, Q., 2016. Homologous temperature of olivine: Implications for creep of the upper mantle and fabric transitions in olivine. Sci. China Earth Sci. 59, 1138–1156. http://dx.doi.org/10.1007/s11430-016-5310-z.
Warren, J.M., Hirth, G., 2006. Grain size sensitive deformation mechanisms in naturally deformed peridotites. Earth Planet. Sci. Lett., 248, 438-450.
Wenk, H.-R., Bennett, K., Canova, G.R., Molinari, A., 1991. Modelling plastic deformation of peridotite with the self-consistent theory. J. Geophys. Res. 96, 8337. http://dx.doi.org/10.1029/91JB00117.
Young, C.I., 1969. Dislocations in the deformation of olivine. Am. J. Sci. 267, 841–852.
Zhang, S., Karato, S., 1995. Lattice preferred orientation of olivine aggregates deformed in simple shear. Nature 375, 774–777.

Chapter IV – Disclination density in polycrystalline olivine experimentally deformed at 1000 °C and 1200 °C

Samples from chapter III and from Demouchy et al. (2012) were investigated to map densities of rotational and translational defects (i.e. disclinations and dislocations, respectively). The disclination density and geometry is compared to the microstructure and literature observations in polycrystalline olivine and metals. This chapter is in preparation for an article in American Mineralogist.

Disclination density in polycrystalline olivine experimentally deformed at 1000 °C and 1200 °C

M. Thieme[1*], S. Demouchy[1], F. Barou[1], B. Beausir[2]

1 Geosciences Montpellier, CNRS & Université de Montpellier, UMR5243, 34095 Montpellier, France

2 Laboratoire d'Etude des Microstructures et de Mécanique des Matériaux, Université de Lorraine, UMR7239, 57045 Metz, France

In preparation for American Mineralogist

* corresponding author

Manuel Thieme

Place Eugène Bataillon, Bat. 22

34095 Montpellier, FRANCE

Manuel.Thieme@gm.univ-montp2.fr

+33 7 68 47 22 81

Abstract

We report a comprehensive dataset characterizing the disclination density in polycrystalline olivine deformed in uniaxial compression or torsion, at temperatures of 1000 °C and 1200 °C, under confining pressure of 300 MPa and deformed to finite strains ranging from 0 to 8.6 %. We find no correlation of the disclination density to stress, strain, temperature or geometrically necessary dislocation (GND) density, but, as expected, a linear correlation to the EBSD step size. Along vertical or horizontal boundaries, disclinations partly occur in dipoles of similar density, but also frequently as isolated monopoles at triple junctions. The occurrence of these monopoles could strongly affect the mechanical strength of fine-grained material by introducing significant stress fields, impeding the movement of defects. Yet, they might also aid as a complementary mechanism to grain boundary sliding and/or dislocation glide and climb by allowing rotation of small crystal volumes.

Keywords: defects; disclinations; plastic deformation; olivine; Earth lithosphere.

IV-1 Introduction

As the most abundant (> 60 % $_{vol}$) and weakest mineral phase in the Earth's upper mantle, olivine largely controls upper mantle rheology and hence the kinematics of upper mantle convection. Experimental deformation of olivine at temperatures relevant to the lithospheric mantle and subducting slabs (< 1200 °C) and extensive studies of mantle-derived xenoliths of peridotites show that dislocation creep is a major deformation mechanism in the uppermost mantle. Dislocations are two dimensional topological defects in the crystal lattice arising from translational lattice incompatibility (as measured by the Burgers vector $\vec{b}$) that are able to glide in defined slip systems. For a polycrystalline aggregate to undergo an arbitrary imposed deformation, four independent slip systems are required (von Mises criterion, Mises, 1928; Hutchinson, 1977). Yet, dislocations in olivine can only glide in three independent slip systems ([100](010), [100](001), [001](010) or [100](010), [001](010), [001](100)) and additional degrees of freedom must be provided by e.g. dislocation climb or grain boundary mechanisms like grain boundary sliding or grain boundary migration. However, at temperatures of < 1200 °C, dislocation climb in olivine is a mechanism too slow to significantly contribute to macroscopic creep (e.g. Goetze, 1978; Evans & Goetze, 1979; Hirth & Kohlstedt, 2003; Cordier, 2014) and dislocation accommodated grain boundary sliding requires displacement and/or rotational discontinuities at grain boundaries (Langdon, 2006). It has been suggested that disclinations can provide such a complementary mechanism for creep in olivine aggregates (Cordier et al., 2014; Sun et al., 2016) as reported for polycrystalline metals (Beausir and Fressengeas, 2013; Fressengeas and Beausir, 2018).

Disclinations are rotational topological defects arising from rotational lattice incompatibility (as expressed by the rotational Frank vector, $\vec{\omega}$; de Wit, 1970), which were already known to exist in liquid crystals (Voltera, 1907; Friedel, 1922; Frank, 1958). Historically, disclinations were thought to be too energetically costly to exist in crystalline

solids (Friedel, 1964; Hirth and Lothe, 1968, p.4), but were nevertheless described first in strongly deformed polycrystalline copper (Beausir & Fressengeas, 2013) and later in deformed polycrystalline olivine (Cordier et al., 2014). In polycrystalline solids, disclinations are thought to arrange in self-screened configurations like dipoles, significantly reducing the elastic energy stored in lattice deformation (Romanov & Vladimirov, 1992; Romanov & Kolesnikova, 2009; Cordier, 2014). As such, they can be used to describe the lattice structure when a single-valued elastic rotation field does not exist, such as grain boundaries (Li, 1972). Disclinations might therefore prove useful in modeling high-angle grain boundaries, grain boundary ledges, deformation of nano-aggregates and grain boundaries as sources and sinks for dislocations (e.g., Kleman & Friedel, 2008). Heinemann et al. (2005) showed that in forsterite, only grain boundaries with misorientation angles up to 20 ° can be modeled with the classic dislocation based Read-Shockley model (Read & Shockley, 1950). For high-angle boundaries, dislocation cores would overlap, invalidating this description. Therefore, high-angle grain boundaries have been modeled successfully as periodic arrays of disclination dipoles (Fressengeas et al., 2011, 2014; Upadhyay et al., 2011; Taupin et al., 2014, Sun et al., 2016, 2017). Similar limitations in dislocation-based grain boundary models are given by spatial considerations. Grain boundaries are traditionally described as infinitely long and thin dislocation walls, which complicates modeling of three-dimensional grain networks in polycrystals and contradicts predictions of spatial patterns referred to as structural units (Sutton & Vitek, 1983). Disclination based models can remove these limitations by rendering the discontinuities of the elastic displacement (i.e., respective rotation) of the crystal lattice along grain boundaries.

In this paper, we investigate the microstructure, particularly we quantify the disclination density in deformed polycrystalline olivine as a function of temperature, finite strain and hydrogen concentration. We use experimental samples from Demouchy et al. (2012) and Thieme et al. (2018), providing a complete new dataset for finite strains up to early steady

state and temperatures of 1000 °C and 1200 °C. Additionally, we investigate the effect of data treatments such as of smoothing and user-defined scale upon display of maps of disclination density.

IV-2 Methods

IV-2.1 Sample material and preparation

We have selected samples previously deformed and characterized by Demouchy et al. (2012) and Thieme et al. (2018). All samples are derived from inclusion free single crystals of San Carlos olivine washed and pulverized in a fluid energy mill, resulting in a grain equivalent diameter before deformation of ~ 2 μm. San Carlos olivine has a mean composition of $(Mg_{0.91}Fe_{0.09}Ni_{0.003})_2SiO_4$ (e.g., Buening & Buseck, 1973; Frey & Prinz, 1978) and naturally low water content of less than 1 ppm wt H_2O (Mackwell et al., 1985; Mei & Kohlstedt, 2000a; Demouchy, 2010). The fine-grained powders of San Carlos olivine were first cold-pressed in Ni capsules, and subsequently sintered at 1200 °C and 300 MPa for 3 h, producing dense polycrystalline samples ~8 mm in diameter and ~16 mm long. Sintered polycrystals were deformed in either uniaxial compression (Thieme et al., 2018) or torsion (Demouchy et al., 2012) in a high pressure high temperature deformation apparatus ("*Paterson Press*"; Paterson, 1990). Confining pressures were 300 MPa, temperature was set to 1000 °C or 1200 °C and equivalent strains range from 0 to 8.6 %. Torsion samples PI0546 and PI0548 contain 45 μl of deionized water added to the cold-pressed aggregate, but limited hydrogen was actually embedded in the olivine lattice (see Demouchy et al., 2012 for details). The samples deformed in torsion were recovered by dissolving the outer Fe and inner Ni jacket in a 1:1 mixture of HNO_3 and HCl. Sections perpendicular to the deformation axis were cut with a low speed saw and embedded in epoxy. Recovered samples were embedded in

epoxy, then polished, including a final chemo-mechanical polish using colloidal silica (0.04 μm particles, average polishing times of 1 h).

For samples deformed in torsion, electron backscatter diffraction (EBSD) maps were taken from three points (1) the maximum radius (i.e., outer edge), (2) the center of the sample, at 1 mm from the maximum radius and (3) at the inner radius, 2 mm from the outer edge. Therefore, for each torsion sample there are three maps corresponding to three different finite strains and strain rates. The shear strain γ was calculated as

$$\gamma = \left(\frac{A_{dis}D}{2l}\right)$$

where A_{dis} is the angular displacement, D the sample diameter and l the sample length. To allow comparison to samples deformed in uniaxial compression, the equivalent strain rate $\dot{\varepsilon}$ was calculated as

$$\dot{\varepsilon} = \dot{\gamma}/\sqrt{3}$$

where $\dot{\gamma}$ is the shear strain rate.

Likewise, the equivalent stress σ was calculated as

$$\sigma = \tau\sqrt{3}$$

where τ is the shear stress.

IV-2.2 Crystallographic orientation measurements and treatments

Olivine crystallographic orientation was obtained by EBSD with the CamScan X500FE CrystalProbe at Geosciences Montpellier (University of Montpellier, France). Exposed sample surfaces were coated with 10-20 nm of carbon, leaving a central uncoated window for EBSD mapping. Electrical conductivity through the sample holder was ensured by applying a double-sided copper-carbon tape partly over and around the epoxy plug. The beam acceleration voltage was 17-17.5 kV, beam current 10 nA and working distance 24-25.1 mm. Olivine, diopside, enstatite and Cr-spinel were acquired during mapping. EBSD data were recorded using the HKL Aztec2 software and treated with ATEX (Beausir & Fundenberger, 2015; Fundenberger & Beausir, 2015). We do not detail here the theoretical framework for disclinations as it is already fully detailed in both Beausir and Fressenges (2013) and Cordier et al., (2014). Figure IV-1 demonstrates how disclination densities are calculated from the elastic rotation field ω_e. In this example, there are two crystals with orientations of (0°,0°,0°) and (45°,0°,0°). A subgrain is inserted into the top grain with a disorientation of 3 ° around axis e_1 (Fig. 1a). The κ_{31}^e component of the curvature tensor (i.e., curvature field) is now derived by one-sided differentiation of the ω_3^e component of the elastic rotation vector (i.e., elastic rotation field), as illustrated in Figure IV-1b. The κ_{32}^e component is derived by forward differentiation of ω_3^e (Figure IV-1c). Finally, the density of wedge disclinations θ_{33} is derived from forward differentiation of the curvature fields κ_{31}^e and κ_{32}^e. The resulting pair of positive (A) and negative (B) wedge disclinations form a dipole that terminates the sub-grain boundary toward the grain boundary and therefore bridges the discontinuity of 3 ° in elastic rotation along this interface. For a full description of the method, see Beausir & Fressengeas (2013), Cordier et al., (2014) and Fressengeas & Beausir (2018).

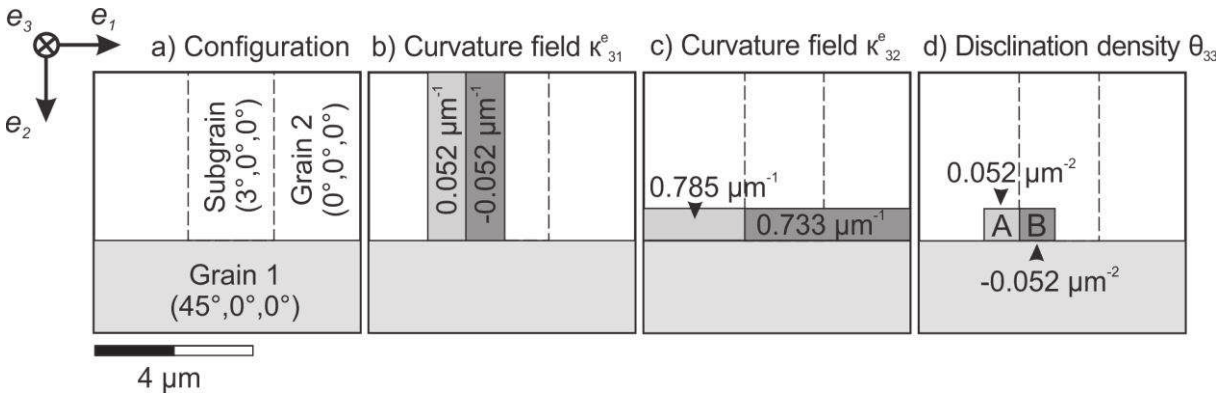

Fig. IV-1 Exemplary calculation of the wedge disclination density for dislocation θ_{33} only. (a) Two grains with orientations of (0°,0°,0°) and (45°,0°,0°). A subgrain is inserted into the top grain with a disorientation of 3 ° around axis e_1. (b) The field of κ^e_{31} component of the curvature tensor is derived by one-sided differentiation of field of ω^e_3 component of the elastic rotation vector (c) The field of κ^e_{32} component of the curvature tensor is derived by forward differentiation of ω^e_3. (d) The density of wedge disclinations θ_{33} is derived from forward differentiation of the field of κ^e_{31} and κ^e_{32} components of the curvature tensor. Image modified after Fressengeas & Beausir (2018, their Figure IV-2).

Data treatment using ATEX software consists of (1) removing the wild spikes defined as pixels with a misorientation of > 1 ° to at least seven neighbors; (2) filtering of orientations with a Kuwahara filter with two iterations and a maximum angle of 5 ° to help identify subgrain boundary domains; (3) defining grain boundaries as planes with a misorientation > 15 ° across them, and subgrains as planes with a misorientation between 2 and 15 °.

Densities of geometrically necessary dislocations (GNDs) and disclination densities were solely calculated for the olivine phase. Disclination densities were obtained for misorientations of 0 – 5 °, since this range of misorientation was found appropriate for our samples during grain determination. Average GND and disclination densities were calculated as the entrywise norm of the respective matrix. Since the maps are only in 2D, the entrywise norm is a partial representation of the 'true' disclinaison density. Thus, here, $\rho_\alpha = \sqrt{\alpha_{12}^2 + \alpha_{13}^2 + \alpha_{21}^2 + \alpha_{23}^2 + \alpha_{33}^2}$ and $\rho_\theta = \sqrt{\theta_{13}^2 + \theta_{23}^2 + \theta_{33}^2}$. For EBSD maps that were acquired

at step sizes < 0.1 µm (see table IV-1), GND and disclination densities were calculated for the original step size, but also for a step size (0.1 µm) common to other maps

IV-3 Results

Forward scattered electron images of the the starting material, samples from uniaxial compression at 1000 °C, from uniaxial compression at 1200 °C and from torsion experiments at 1200 °C are presented in Figure IV-2. The samples are composed of Olivine (> 99.8 $\%_{Area}$), with enstatite and cr-spinel as rare secondary phases (< 0.2 $\%_{area}$). Grains are sub-equant, with a mean aspect ratio of 1.4–1.5 and maximum aspect ratios are up to ~ 3.0. The long axis of grains of the starting material and of samples deformed in uniaxial compression is preferentially oriented at 180 ° to the compression axis. Grain boundaries are curved and/or serrated. We observed hints for grain boundary migration (i.e. grains growing at the expense of more highly misoriented neighbors), which already appear in the sintered (hot pressed) starting material. Some grains show internal micro-cracks oriented at 60 ° to each other, that are already present in the starting material. There is no significant displacement along these cracks (i.e., no clear grain boundary sliding). Figure IV-2 dominantly shows porosity created by plucking of grains during the polishing stage. Original porosity of similar experiments is typically < 3$\%_{area}$ (Beeman & Kohlstedt, 1993; Hirth & Kohlstedt, 1995; Hansen et al., 2012).

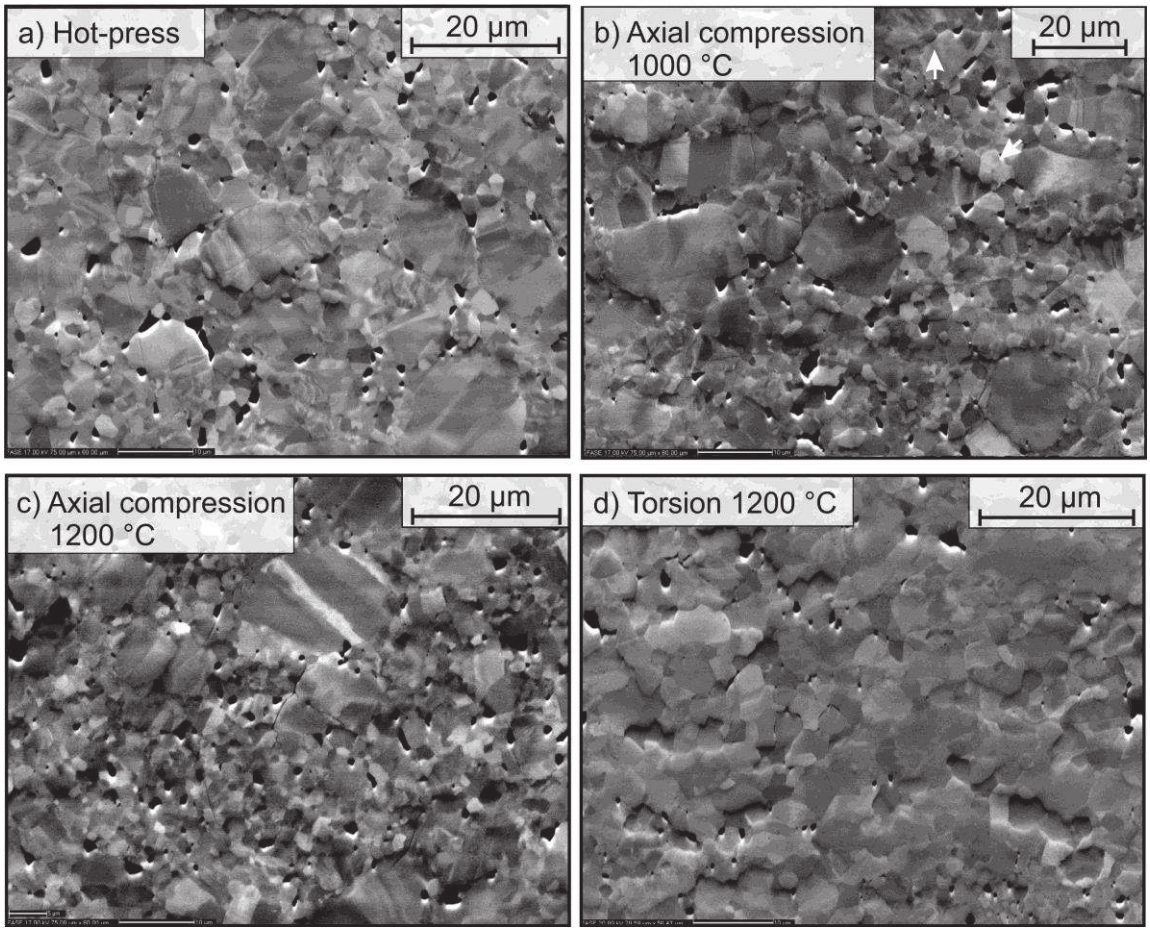

Fig. IV-2 Forward scattered electron images from scanning electron microscopy (SEM). (a) prior to deformation (hot-press CMT16-7); (b) after axial compression at 1000 °C and for 7.3% of finite strain (CMT17-2); (c) after axial compression at 1200 °C and for 8.6% of finite strain (CMT16-9); (d) after torsion at 1200 °C and for 2.05 % of equivalent strain (PI0546 from Demouchy et al., 2012). Dark areas are plug outs from polishing and residual pores from hot-press.

The conditions of the deformation experiments and average GND and disclination densities are summarized in Table IV-1. The indexation rate is > 91.44 %. Average grain sizes range from 1.9 to 3.3 µm. the GND density ranges from 3.6×10^{-2} to 1.7×10^{-1} μm^{-1} and disclination density ranges from 2.5×10^{-4} to 6.9×10^{-3} $rad\mu m^{-2}$ (IV-1). As expected, both densities are strongly dependent on the resolution of the map (i.e., EBSD map step size), but do not clearly vary between samples deformed in uniaxial compression or torsion for samples with comparable stresses and finite strains. Doubling the step size (from 0.05 to 0.1 µm)

results in a reduction of the GND density by a factor of 2 and of the disclination density by a factor of 4. The frequency of subgrain boundaries (percentage of boundaries with a misorientation of $3° \leq \theta \leq 15°$) is highly variable, ranging from 2.8 to 13 and depends on the map (area size and step size) rather than the sample. Hydrous samples (PI0546 and PI0548) have similar GND and disclination densities compared to samples deformed in uniaxial compression.

Table IV-1 Experimental parameters, dislocation and disclination densities for all samples. Roman numbers identify individual EBSD maps of the same sample. Average grain sizes are calculated as the diameter of a circle with equivalent area. Geometric necessary dislocation (GND) and disclination densities are calculated as the entrywise norm. Maps of torsion samples are taken from three different sample diameters and hence strains. GND and disclination densities of maps obtained with step sizes < 0.1 μm were additionally calculated for a subsampled dataset with step size of 0.1 μm.

Sample	Temperature T (°C)	Equivalent strain ε/γ_{eq} (%)	Equivalent strain rate $\dot{\varepsilon}/\dot{\gamma}$ (s^{-1})	Diff. stress σ (MPa)	Nb. grains	Step size (μm)	Indexation rate (%)	Av. grain size (μm)	Freq. subgrain boundaries (%; $3° \leq \theta \leq 15°$)	GND density (μm^{-1})	Max GND density (μm^{-1})	Disclination density ($rad\mu m^{-2}$)
Deformation in axial compression												
CMT16-7 SII	1200	0	0	0	176	0.1	97.23	2.41	8.33	1.0×10^{-1}	1.3×10^{1}	3.8×10^{-3}
CMT16-6 SIII	1000	0.11	1.9×10^{-6}	80	313	0.1	97.67	1.88	12.62	1.3×10^{-1}	1.5×10^{1}	4.3×10^{-3}
CMT16-8 SV	1000	1.07	3.3×10^{-6}	684	97	0.1	95.79	2.41	14.11	1.3×10^{-1}	1.3×10^{1}	1.9×10^{-3}
CMT16-8 SVI	1000	1.07	3.3×10^{-6}	684	93	0.07	98.53	1.97	10.03	1.5×10^{-1}	2.1×10^{1}	6.9×10^{-3}
						0.1				1.0×10^{-1}	1.5×10^{1}	3.4×10^{-3}
CMT16-12 SIII	1200	0.88	7.2×10^{-6}	150	38	0.06	96.44	2.12	7.1	8.0×10^{-2}	2.3×10^{1}	3.3×10^{-3}
						0.1				4.8×10^{-2}	1.4×10^{1}	1.2×10^{-3}
CMT16-13 SII	1200	3.68	1.0×10^{-5}	313	41	0.5	94.87	1.48	2.83	8.8×10^{-2}	2.5×10^{1}	9.9×10^{-4}
						0.1				4.4×10^{-2}	1.3×10^{1}	2.5×10^{-4}
CMT16-13 SIII	1200	3.68	1.0×10^{-5}	313	225	0.1	96.14	1.86	10.17	1.3×10^{-1}	1.5×10^{1}	3.7×10^{-3}
CMT16-13 SIV	1200	3.68	1.0×10^{-5}	313	104	0.1	95.62	1.94	8.04	8.5×10^{-2}	1.4×10^{1}	3.7×10^{-3}
CMT16-9/2 SI	1200	8.59	1.0×10^{-5}	322	144	0.07	98.33	1.72	10.03	3.6×10^{-2}	1.8×10^{0}	6.6×10^{-4}
						0.1				9.6×10^{-2}	1.5×10^{1}	2.2×10^{-3}
CMT16-9 SII	1200	8.59	1.0×10^{-5}	322	265	0.1	96.36	2.22	12.75	1.2×10^{-1}	1.4×10^{1}	4.2×10^{-4}
Deformation in torsion												
PI0548 III	1200	1.75	3.6×10^{-5}	248	613	0.1	91.44	1.89	5.08	1.6×10^{-1}	1.5×10^{1}	2.3×10^{-3}
PI0546 VII	1200	1.08	3.6×10^{-5}	264	226	0.1	96.05	2.4	7.93	1.5×10^{-1}	1.4×10^{1}	1.4×10^{-3}
PI0546 XVII	1200	1.08	3.6×10^{-5}	264	152	0.07	94.98	2.33	3.95	1.1×10^{-1}	2.1×10^{1}	3.0×10^{-3}
						0.1				7.9×10^{-2}	1.4×10^{1}	1.5×10^{-3}
PI0546 V	1200	1.24	4.1×10^{-5}	264	153	0.062	95.09	2.35	3.08	1.5×10^{-1}	2.4×10^{1}	2.2×10^{-3}
						0.1				9.4×10^{-2}	1.5×10^{1}	8.4×10^{-4}
PI0546 VIII	1200	1.24	4.1×10^{-5}	264	228	0.1	96.88	2.99	7.99	1.4×10^{-1}	1.4×10^{1}	2.2×10^{-3}
PI0546 XVI	1200	1.24	4.1×10^{-5}	264	135	0.07	95.28	2.44	3.52	1.0×10^{-1}	2.0×10^{1}	3.5×10^{-3}
						0.1				7.2×10^{-2}	1.4×10^{1}	1.7×10^{-3}
PI0546 IX	1200	1.4	4.6×10^{-5}	264	217	0.1	97.15	2.72	10.42	1.7×10^{-1}	1.5×10^{1}	3.4×10^{-3}
PI0546 XIV	1200	1.4	4.6×10^{-5}	264	26	0.07	93.19	2.91	1.69	1.2×10^{-1}	1.7×10^{1}	1.2×10^{-2}
						0.1				8.1×10^{-2}	1.2×10^{1}	5.9×10^{-3}
PI0546 XVIII	1200	1.4	4.6×10^{-5}	264	116	0.07	94.94	3.34	2.59	7.3×10^{-2}	2.0×10^{1}	2.2×10^{-3}
						0.1				5.1×10^{-2}	1.4×10^{1}	1.1×10^{-3}

Maps of the average grain misorientation, grain internal misorientation and GND density are given in Figure IV-3 as an example. Grain internal misorientation is not always well developed, showing areas with gradual changes in orientation with no straight boundaries. As expected, GND density is the highest along well-developed subgrain boundaries.

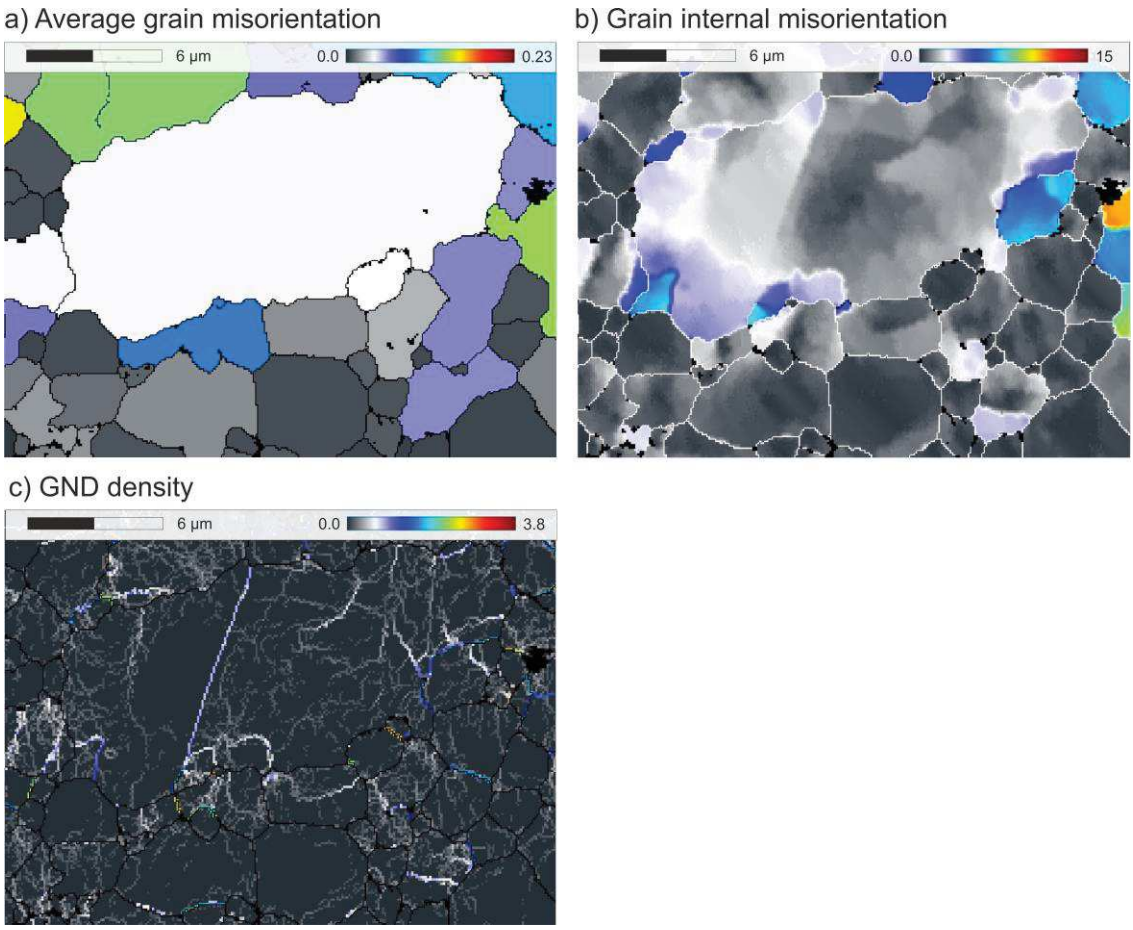

Fig. IV-3 (a) average grain misorientation map, (b) internal misorientation relative to the grain gravity center and (c) density of geometrically necessary dislocations, for sample PI0546 deformed in torsion at 1200 °C and for 1.8 % of equivalent strain.

Although disclinations densities for $\theta_{13,}$ θ_{23} and θ_{33} are calculated by ATEX, we only present maps of the wedge disclination density θ_{33} in figure IV-4, using different values of smoothing and scale (automatic or user-defined). We focus on θ_{33} since it only depends on

κ_{31}^{e} and κ_{32}^{e} and can be readily obtained from the 2-D maps of our samples. While smoothing strongly affects the mapped size of disclinations, it does not affect the calculated disclination density. In automatic mode, strongly negative disclination densities create artifacts where the center of disclination poles jumps the scale and is mapped as a highly positive value (red arrows in Figure IV-4 showing dark red color surrounded by blue-shade colors). This can be alleviated by manually adjusting the scale individually for each map by a factor of ~1.5, although in the same process, disclinations with low densities blend in with the background. Maps of disclination densities as a function of strain, temperature and deformation setup are given in Figure IV-5. We chose maps with high percentages of straight horizontal or vertical grain boundaries, to avoid artifacts created at grain boundary steps (e.g., due to map pixelization) and the inherent limited calculation of the rotation gradient at a stepped boundary. Although disclination dipoles do exist, many disclinations appear as monopoles located at triple junctions. Where dipoles exist, both the negative and the positive poles show densities of the same magnitude. Weaker disclinations often appear as strings of monopoles along grain boundaries, possibly due to pixelization. Torsion samples, deformed at higher finite strain (~8%), do not show quantitative differences in disclination density when compared to samples deformed in uniaxial compression.

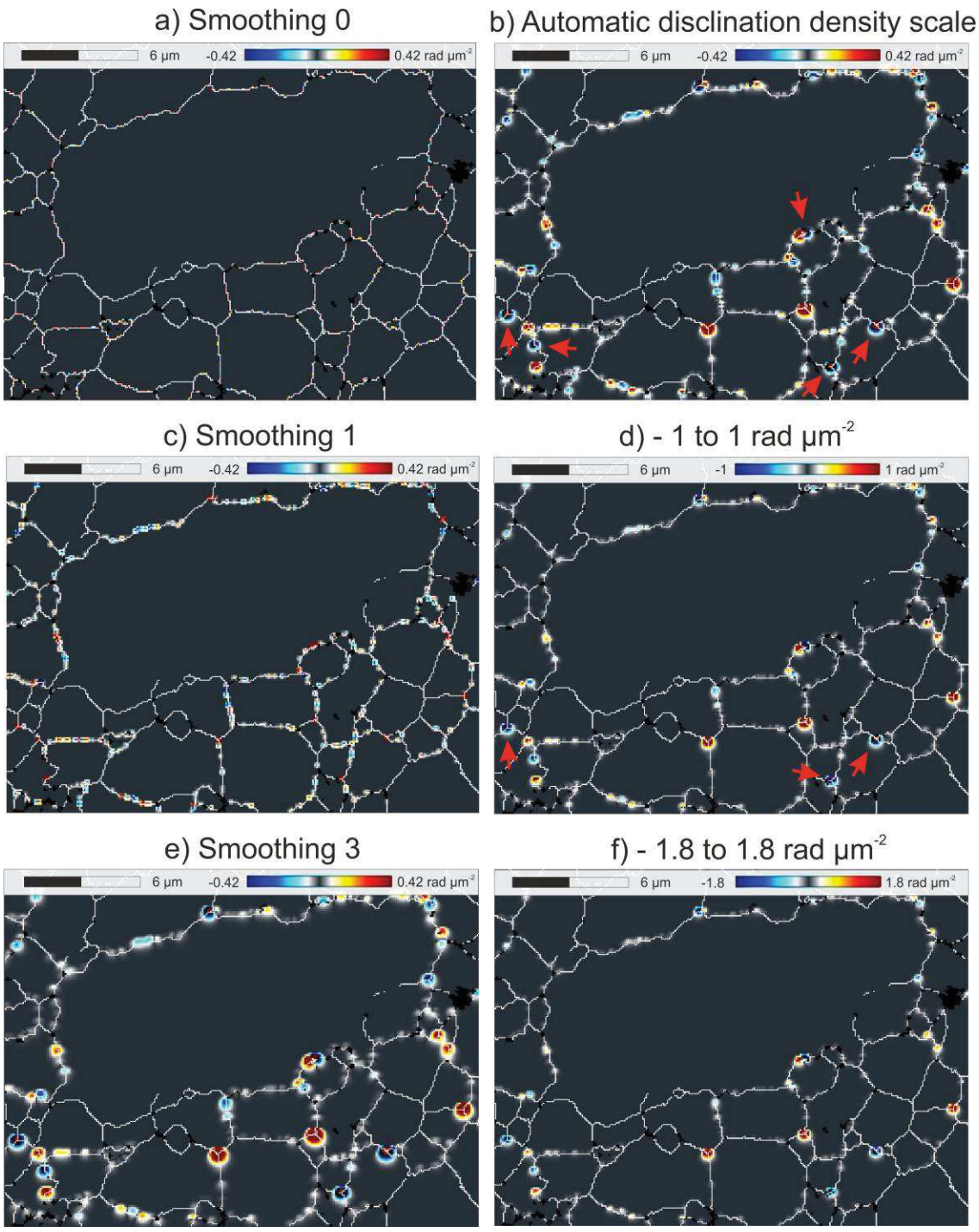

Fig. IV-4 Comparison of wedge disclination densities θ_{33} for smoothing values of 0, 1 and 3 and for different disclination density scales (automatic or user-defined scale). Maps are for sample PI0546 deformed in torsion at 1200 °C and for 1.08 % of equivalent strain.

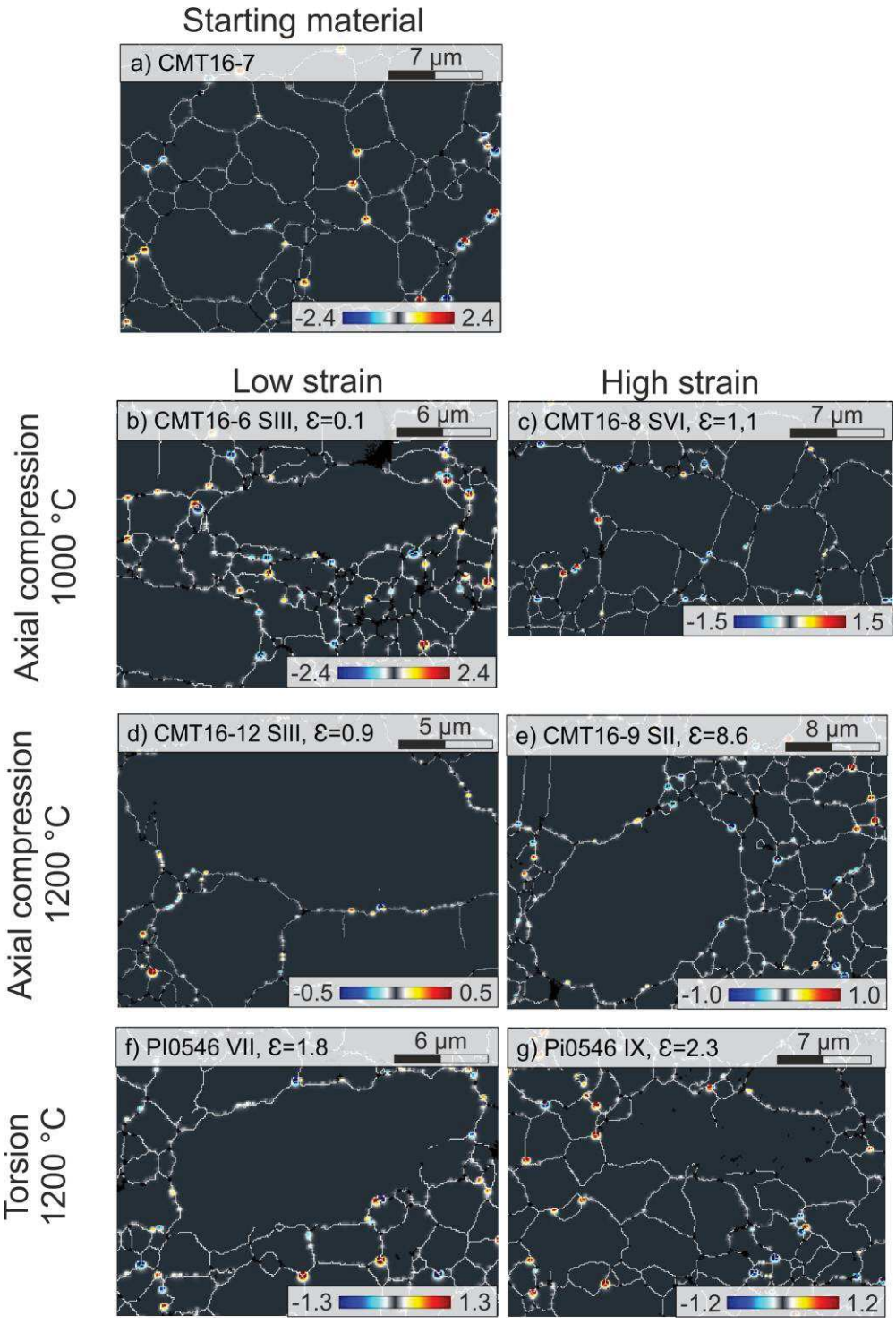

Fig. IV-5 (a) Maps of wedge disclination density θ_{33} in the starting material and (b to g) for representative samples deformed at different values of strain and temperature in either uniaxial compression or torsion. All maps are obtained with a smoothing value of 2.

To qualify and quantify the possible dependence of the disclination density on the experimental parameters, the average density of disclinations (entrywise norm) is shown as a function of the GND density, step size from EBSD maps, maximal stress and finite strain in Figure IV-6. Densities generally cluster without any clear (positive or negative) correlation. Outliers are most likely related to maps with a small number of grains not being representative.

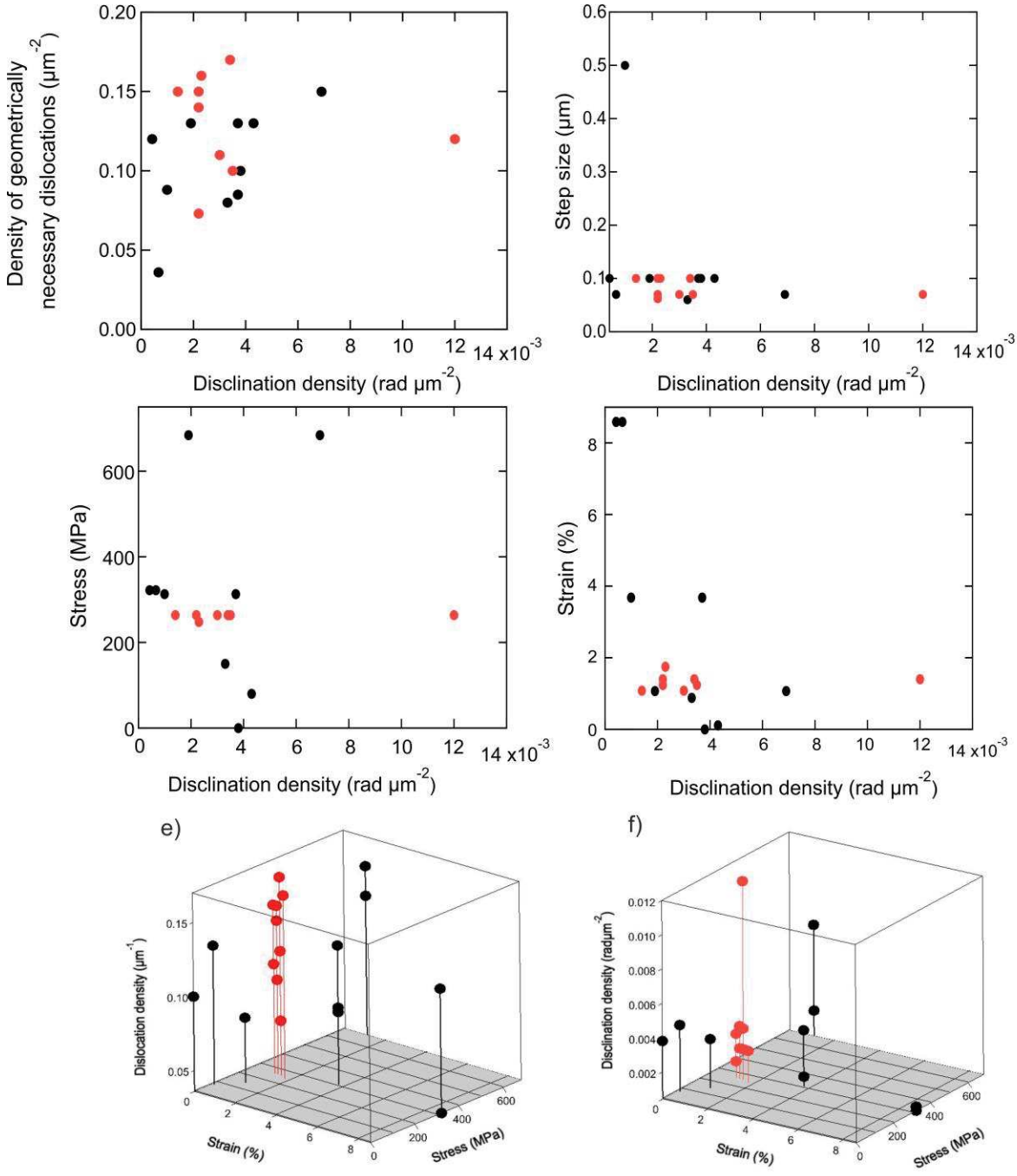

Fig. IV-6 Average disclination density as a function of (a) the density of GNDs, (b) EBSD map step size, (c) maximal stress, (d) finite strain and (e & f) 3-D scatter plots of the dislocation and disclination density as a function of stress and strain.

4. Discussion

As expected for any parameter which is a function of grid resolution, the calculated dislocation and disclination density depends on the EBSD step size. Nevertheless, for a constant step size (0.07 or 0.1 μm), we did not find the mechanical strength of olivine to be directly controlled by the average disclination density (fig. IV-6). Although the disclination density seems not to be controlled by mechanical parameters (i.e. stress and strain), disclinations might provide additional degrees of freedom for dislocation glide and climb, as well as for grain boundary sliding at lower temperature (and high stresses). The occurrence of isolated disclination monopoles fits to high-resolution transmission microscopy of mechanically milled, nanocrystalline Fe by Murayama et al. (2002). The existence of a high amount of disclination monopoles might affect the mechanical strength of fine-grained materials, due to the stress fields associated with disclinations impeding defect movement (Marcinkowski, 1977; Hirth & Lothe, 1982). Likewise, partial wedge disclinations only allow rotation of small lattice volumes of several nm, possibly further affecting the deformation response and contributing to grain size reduction (ie., dynamic recrystallization) during deformation. To the contrary, disclinations might provide a complementary or competing mechanism to grain boundary sliding in fine-grained material by allowing rotation even in the absence of ionic diffusion and the inherent recovery processes. The result would be a partial softening and hence disclinations might control the maximum viscosity in these conditions.

As a first study, we point out to the need for normalization procedures for step size and area size during EBSD maps acquisitions and recommend the use of conductive epoxy to reduce the electrical charging of fine-grained silicates and the resulting drifting in EBSD maps.

5. Conclusions

In this paper we present dislocation and disclination densities in deformed polycrystalline olivine for a broad range of experimental conditions. Based on the new data set, we find that the disclination density is independent of stress, strain, temperature and GND density, but proportional to the EBSD step size. Lowering step sizes results in increasing calculated disclination densities at a rate of 1:4. Disclinations appear as dipoles but also as monopoles. Where dipoles exist, both partial poles show similar disclination densities in polycrystalline olivine.

Acknowledgements

This project received funding from the European Union's Horizon 2020 research and innovation program under the Marie Sklodowska Curie Grant agreement No. 642029. We thank C. Nevado and D. Delmas for providing high-quality thin sections for SEM and TEM. The EBSD-SEM facility in Montpellier is supported by the Institut National de Sciences de l'Univers (INSU) du Centre National de la Recherche Scientifique (CNRS, France) and the Conseil Régional Occitanie (France).

References

Beausir, B., Fressengeas, C., 2013. Disclination densities from EBSD orientation mapping. Int. J. Solids Struct. 50, 137–146.

Beausir, B. and J.-J. Fundenberger, Université de Lorraine - Metz, 2015, ATOM - Analysis Tools for Orientation Maps, http://atom-software.eu/.

Beeman, M.L., Kohlstedt, D.L., 1993. Deformation of fine-grained aggregates of olivine plus melt at high temperatures and pressures. J. Geophys. Res. 98, 6443–6452. http://dx.doi.org/10.1029/92JB02697.

Buening, D.K., Buseck, P.R., 1973. Fe-Mg lattice diffusion in olivine. J. Geophys. Res. 78, 6852–6862. http://dx.doi.org/10.1029/JB078i029p06852.

Cordier, P., Demouchy, S., Beausir, B., Taupin, V., Barou, F., Fressengeas, C., 2014. Disclinations provide the missing mechanism for deforming olivine-rich rocks in the mantle. Nature 507, 51–56.

Demouchy, S., 2010. Diffusion of hydrogen in olivine grain boundaries and implications for the survival of water-rich zones in the Earth's mantle. Earth Planet. Sci. Lett. 295, 305–313. http://dx.doi.org/10.1016/j.epsl.2010.04.019.

Demouchy, S., Tommasi, A., Barou, F., Mainprice, D., Cordier, P., 2012. Deformation of olivine in torsion under hydrous conditions. Phys. Earth Planet. Inter. 202–203, 56–70. http://dx.doi.org/10.1016/j.pepi.2012.05.001.

deWit, R., 1970. Linear theory of static disclinations. In: Fundamental aspects of dislocation theory. In: Simmons, J.A., de Wit, R., Bullough, R. (Eds.), NBS Spec. Publ. 317, vol. 1, pp. 651–680 (National Bureau of Standards, Washington, DC).

Evans, B. and Goetze, C., 1979. The temperature variation of hardness of olivine and its implication for polycrystalline yield stress, Journal of Geophysical Research, 84, 5505-5524.

Frank, F.C., 1958. I. Liquid crystals. On the theory of liquid crystals. Discuss. Faraday Soc. 25, 19. http://dx.doi.org/10.1039/df9582500019.

Frey, F.A., Prinz, M., 1978. Ultramafic inclusions from san carlos, Arizona: petrologic and geochemical data bearing on their petrogenesis. Dev. Petrol. 5, 129–176. http://dx.doi.org/10.1016/B978-0-444-41658-2.50013-4.

Friedel, G., 1922. The mesomorphic states of matter. Ann. Phys. 18, 273–474. http://dx.doi.org/10.1201/9780203022658.ch1b.

Goetze, C., 1978. The mechanisms of creep in olivine, Philosophical Transactions of the Royal Society of London A, 288, 99-119.

Hansen, L.N., Zimmerman, M.E., Dillman, A.M., Kohlstedt, D.L., 2012. Strain localization in olivine aggregates at high temperature: a laboratory comparison of constant-strainrate and constant-stress boundary conditions. Earth Planet. Sci. Lett. 333–334, 134–145. http://dx.doi.org/10.1016/j.epsl.2012.04.016.

Hirth, G. and Kohlstedt, D. L., 2003. Rheology of the Upper Mantle and the Mantle Wedge: A View from the Experimentalists in The Subduction Factory, Eiler, J., ed. American Geophysical Union Geophysical Monograph 138, 83-105.

Hirth, G., Kohlstedt, D.L., 1995. Experimental constraints on the dynamics of the partially molten upper mantle: deformation in the diffusion creep regime. J. Geophys. Res. 100, 15441–15449. http://dx.doi.org/10.1029/94JB02128.

Hirth, J.P., Lothe, J., 1982. Theory of Dislocations. McGraw-Hill, New York.

Fundenberger, J.-J., Beausir, B., 2015. JTEX - Software for -Texture Analysis, http://jtex-software.eu/.

Kleman, M., Friedel, J., 2008. Disclinations, dislocations, and continuous defects: a reappraisal. Rev. Mod. Phys. 80, 61.

Langdon, T. G. Grain boundary sliding revisited: developments in sliding over four decades. J. Mater. Sci. 41, 597–609 (2006).
Li, J.C.M., 1972. Disclination model of high angle grain boundaries. Surface Sci. 31,12.
Marcinkowski, M. J., 1977. The differential geometry of twisting. Philos. Mag. 36, 1499.
Mackwell, S.J., Kohlstedt, D.L., Paterson, M.S., 1985. The role of water in the deformation of olivine single crystals. J. Geophys. Res. 90, 11319. http://dx.doi.org/10.1029/JB090iB13p11319.
Mei, S., Kohlstedt, D., 2000a. Influence of water on plastic deformation of olivine aggregates 1. Diffusion creep regime. J. Geophys. Res. 105, 21457–21469.
Paterson, M.S., 1990. Rock deformation experimentation. Geophys. Monogr. 56, 187–194.
Romanov, A.E., Vladimirov, V.I., 1992. Disclinations in crystalline solids. In: Nabarro, F.R.N. (Ed.), Dislocations in Solids, vol. 9. Elsevier, Amsterdam, p. 191. Romanov, A.E., Kolesnikova, A.L., 2009. Application of disclination concept to solid structures. Prog. Mat. Sci. 54, 740.
Heinemann, S., Wirth, R., Gottschalk, M., Dresen, G., 2005. Synthetic [100] tilt grain boundaries
in forsterite: 9.9 to 21.5°, Phys. Chem. Miner. 32, pp. 229–240.
Sutton, A.P., Vitek, V., 1983. On the structure of tilt grain boundaries in cubic metals. I. Symmetrical tilt boundaries. Phil. Trans. Roy. Soc. London A309, 1.
Sun, X.-Y., Cordier, P., Taupin, V., Fressengeas, C., Jahn, S., 2016. Continuous description of a grain boundary in forsterite from atomic scale simulations: the role of disclinations. Phil. Mag. 96(17), 1757-1772.
Volterra, V., 1907. Sur l'équilibre des corps élastiques multiplement connexes. Ann. Sci. Ecol. Norm. Sup. III 24, 401–517.
Warren, J.M. and G. Hirth, 2006. Grain Size Sensitive Deformation Mechanisms in Naturally Deformed Peridotites, Earth and Planetary Science Letters, 248, 423-435.

Chapter V – Shear deformation of nano- and micro-crystalline olivine at seismic slip rates

Here, I investigate the frictional strength and correlated microstructure of olivine powders under slip rates common during seismic slip. The data for this chapter was obtained in the scope of my academic ITN-CREEP secondment at the Rock Mechanics Laboratory, Durham University in January 2018. This chapter is an article in preparation for Earth and Planertary Science Letters.

Shear deformation of nano- and micro-crystalline olivine at seismic slip rates

M. Thieme[1*], G. Pozzi[2], S. Demouchy[1], N. De Paola[2], F. Barou[1], S. Koizumi[3]

1 Geosciences Montpellier, CNRS & Université de Montpellier, UMR5243, 34095 Montpellier, France

2 Rock Mechanics Laboratory, Earth Sciences Department, Durham University, DH1 3LE Durham, UK

3 Geochemical Laboratory, Graduate School of Science, University of Tokyo, 113-0033 Tokyo, Japan

In preparation for *Earth and Planetary Science Letters*

* corresponding author

Manuel Thieme

Place Eugène Bataillon, Bat. 22

34095 Montpellier, FRANCE

Manuel.Thieme@gm.univ-montp2.fr

+33 7 68 47 22 81

Abstract

We report mechanical data and fully characterize the microstructure of olivine aggregates deformed in torsion at slip rates from 10^{-2} ms^{-1} to 1 ms^{-1} and axial stresses of 20 MPa. A number of 33 experiments were performed using iron-free nanocrystalline olivine powder (ϕ = 0.07 μm) and powder of iron-bearing olivine from the San Carlos and San Bernardino volcanic fields (Arizona, USA; ϕ = 70 ± 2 μm). Recovered samples were characterized with scanning electron microscopy and electron backscatter diffraction. Friction coefficients drop to < 0.4 after only 0.1 m of slip, independent of grain size and/or chemistry. Likewise, initial texture in the compacted starting material as expressed by the texture J-index is reduced to 1.1 after only 0.03 m of slip. We find evidence that deformation takes place by both cataclastic flow and dislocation creep. Cataclastic flow leads to a rapid grain size reduction and initiates shear localization near the sample zone with the highest shear strain (γ = 38 – 9560). While the dominant deformation mechanism seems to be temperature weakening, we find no evidence for frictional melting or thermal decomposition.

Keywords: olivine, friction, experimental deformation, shear zone, high-velocity torsion

V-1 Introduction

The drastic energy release during Earthquakes is both related to the accumulated elastic strain of the rock volume around a fault and to the fault itself as a contact problem. Deformation during typical earthquakes reaches comparatively high slip rates of up to 10 ms^{-1}, displacements during single events of up to 10 m and normal stresses of up to several hundred MPa (Heaton, 1990). While it is currently impossible to reproduce all parameters affecting fault strength in Nature during laboratory-based deformation experiments, combinations of e.g. slip-rate and axial stress have been investigated in rotary shear deformation experiments (e.g., Beeler et al., 1996; Goldsby & Tullis, 2002). The coefficient of friction (μ, shear stress divided by axial stress) appears to be a key parameter controlling slip, geometry, radiated seismic energy and heat flow of faults (e.g., Scholz, 2002; Cocco & Tinti, 2008). Sliding experiments at sub-seismic slip rates (< 1 mm s^{-1}) and with natural rocks by Byerlee (1978) demonstrated that μ ranges from 0.6 to 0.85 depending on load and that μ is mostly independent of material under experimental conditions. Yet, numerical geodynamic models (e.g. Crameri et al., 2012; Crameri & Tackley, 2015; Nakagawa & Tackley, 2015), seismic stress inversion (Maerten et al., 2016a,b) and stress inversion and slip analyses on natural fault zones (e.g., Bolognesi & Bistacchi, 2018) require significantly lower coefficients of friction, typically ≤ 0.2, to achieve model Earth-like fault behaviors. Additionally, assuming coefficients of friction in the range of 0.6 – 0.85 leads to misbalanced energy budgets. Such values of friction should result in shear stresses on faults near the Earth's surface in the order of 50 – 100 MPa and hence substantial frictional heat production – an observation not made in nature (e.g., Saffer, 2003; Scholz, 2000).

Laboratory experiments approaching seismic slip rates (≥ 0.5 m s^{-1}) report coefficients of friction between 0.1 and 0.3 (Di Toro et al., 2004, 2006 a, b., 2011; Hirose & Shimamoto, 2005; Han et al., 2007; Del Gaudio et al., 2009; Mizoguchi et al., 2009; Ferri et al., 2010;

Reches & Lockner, 2010; De Paola et al., 2011; Di Toro et al., 2011; Goldsby & Tullis, 2011). This reduction in friction was proposed to be caused by several processes: frictional heating (Rice, 2006), melting (Hirose & Shimamotot, 2005; Di Toro et al., 2006a; Nielsen et al., 2006), an *a priori* presence of weak mineral phases (e.g. smectite; Carpenter et al., 2011), mineral phase reaction or thermal decomposition (e.g., Di Toro et al., 2004; Han et al., 2007; De Paola et al., 2011), but a satisfying consensus based on observables was not reached yet.

Field evidence (Griggs and Handin, 1960; Obata and Karato, 1995; Andersen & Austrheim, 2006; Andersen et al., 2008; Piccardo et al., 2008), torsion experiments under high axial stress (5 GPa, Bridgman, 1936) and theoretical studies (Ogawa, 1987; Kelemen & Hirth, 2007; Braeck & Podladchikov, 2007; John et al., 2009) suggest friction-induced melting occuring in olivine-rich mantle rocks at asthenospheric mantle temperature conditions. The case of the 1994 Bolivia earthquake (magniude M_w 8.2, 641 km of depth) has been used to suggest lubrication by frictional melt based on energetic and seismic considerations (Kanamori et al., 1998; Bouchon & Ihmlé, 1999). But so far, the only experimental investigation of peridotite deformed at seismic slip rates was performed by Di Toro et al. (2006b) & Del Gaudio (2009), yet without full characterization of the recovered microstructures.

In this study we investigate the previously suggested weakening mechanisms by deforming olivine at seismic slip rates but at lower axial stresses than expected at depths relevant for upper mantle rocks. Olivine (Fo_{90}), while not a common mineral composing Earth's crust has a significantly lower melting temperature (Tm = 1765 °C at 0 GPa, 2075 °C at 6 GPa; Bowen and Shairer, 1935; Wang, 2016) and low self-diffusion rates at crustal conditions, impeding dislocation creep, diffusion creep and dislocation/diffusion accommodated grain boundary sliding at temperatures routinely achieved in deformation experiments at seismic slip rates. We investigate here mechanical data and discuss previously proposed deformation mechanisms as a function of grain size, chemical composition and

microstructure of deformed monomineralic olivine aggregates obtained by scanning electron microscopy and electron backscatter diffraction.

V-2 Methods

V-2.1 Starting material

We used three different types of starting material (1) iron-free nanocrystalline olivine powder with an average grain size of ϕ = 0.07 μm, synthetized by Koizumi et al. (2010; vacuum sintered), called 'nanoFo_{100}' in the following text; (2) powder from crushed iron-bearing olivine from San Carlos (Arizona, USA) with a composition close to Fo_{91} (see Buening & Buseck, 1973; Frey & Prinz, 1978) later called 'SC olivine'; and (3) powder from crushed iron-bearing olivine from the San Bernardino volcanic field (Arizona, USA; Lynch, 1978; Neville et al., 1985), later called 'SB olivine'.

SC and SB olivines were prepared by picking optically inclusion-free single crystals and manually crushing them with a mortar and pestle. Crushed grains were dry sieved and only the grain fraction between 63 – 90 μm (70 ± 2 μm in average) used for deformation experiments. San Carlos olivine naturally has an extremely low hydrogen concentration of less than 1 ppm wt H_2O (Mackwell et al., 1985; Mei & Kohlstedt, 2000; Demouchy, 2010). Potential hydrogen incorporated in the NanoFo_{100} starting materials was removed during powder sintering at high temperature (Koizumi et al. 2010; analyzed by gas chromatography-mass spectrometry).

V-2.2 Deformation assembly and apparatus

A total number of 33 experiments were performed with a rotary shear frictional testing machine at the Rock Mechanics Laboratory, Durham University (UK; Model MIS-233-1-77; Ma et al. 2014, De Paola et al. 2015, Pozzi et al. 2018). Unconsolidated olivine powders were loaded into polytetrafluoroethylene (PTFE) cylinders with internal diameters of 25 mm and a central hole of 10.5 mm and contained in-between two titanium alloy cylinders with machined pyramidal grooves at the end. To prevent powder loss during the experiment, the ring was tightened to the titanium cylinders with a hose clip. The inner edges of the PTFE cylinder were machined and smoothed to reduce ablation and contamination of the sample. The alignment of the assembly during experiments is maintained by a hydraulic mechanical lock. One gram of SC and SB olivine powder was used per experiment resulting in a layer of uncompressed powder of approximately 1.2 mm of thickness. Since the nanoFo$_{100}$ powder is less dense, only 0.7 g were used per experiment. This amount still resulted in a layer thickness of approximately 5.1 mm. The powders were compacted *in situ* prior to deformation by applying 20 MPa of axial (8.09 kN, applied for a few seconds). Target velocities were 1 m s^{-1}, 0.1 m s^{-1} and 0.01 ms^{-1}. Experiments were stopped at different points in the mechanical curves to provide sample microstructure evolution with increasing strain and therefore allowing investigation of the involved deformation mechanisms and their impact on frictional strength. All experiments were run at room temperature and humidity.

The acceleration and deceleration of the deformation cylinders was controlled by a signal generator (DF1906), imposing a target slip. The maximum target slip rate of 1 ms^{-1} was reached in 260^{-6} s or about 200 μm of slip, giving an acceleration velocity of 3.85 ms^{-2}. Sampling frequency was in between 500 Hz and 5 kHz depending on the slip rate. Axial load cell resolution is ± 5 × 10^{-3} kN, torque is measured by two compression load cells with a resolution of ± 5 × 10^{-4} kN. Axial displacement is measured by a high sensitivity strain gauge with a resolution of ± 2 × 10^{-3} mm. Fluctuations in the load are automatically corrected by a

high-precision air regulator. Since the slip rate v in the sample depends on the radius r, we calculate an equivalent slip rate v_e, at 2/3 of the radius as

$$v_e = \frac{4\,\pi\,R\,r}{3} \qquad \text{eq. (1)}$$

where R is the revolution rate of the titanium cylinders holding the olivine aggregate. Likewise, we calculate an equivalent slip d_e at 2/3 of the radius as

$$d_e = v_e\,t \qquad \text{eq. (2)}$$

where t is the time of deformation. For the same reasons, all our thin sections are cut at 2/3 of the radius, to be consistent with the calculated values of v_e and d_e. The average shear strain γ has been calculated as

$$\gamma = \tan\varphi = \frac{r\theta}{2h} \qquad \text{eq. (3)}$$

where φ is the angular shear, θ is the angular displacement in radians and h is the average slip zone thickness inferred from scanning electron microscopy (SEM) imaging. The average thickness of our slip zones satisfies the condition $h \leq 4\sqrt{\kappa d/v}$, where k is the thermal diffusivity, which allows to treat the slip zone as a zero-thickness plane. Due to the geometry of the assembly, the temperature of the sample could not be measured directly. The temperature change inside the slip zone during deformation has therefore been calculated based on frictional heating, heat capacity and thermal diffusivity following Rice (2006),

$$\Delta T = \frac{\mu\sigma_n\sqrt{vd}}{\rho c_p\sqrt{\pi\kappa}} \qquad \text{eq. (4)}$$

where μ is the friction coefficient, σ_n the axial stress, v the slip velocity, d the displacement, ρ the sample density and c_p the specific heat capacity.

V-2.3. Scanning electron microscopy and electron backscatter diffraction

Starting powder, compressed undeformed powder and deformed samples were embedded into epoxy at room pressures and subsequently analyzed using a FEI Quanta 200 FEG SEM at Géosciences Montpellier (Montpellier University, France) and using a Hitachi SU-70 FEG SEM at the Department of Earth Sciences Durham (Durham University, UK). Microstructure analyses using electron backscatter diffraction (EBSD) were performed at Geosciences Montpellier with a CamScan X500FE CrystalProbe. Deformed samples contained Riedel fractures and thermal cooling cracks, making recovery challenging. Nevertheless, chips of most samples could be obtained. These chips were fixed to mounts with cyanoacrylate while aligned vertically and embedded in epoxy. Epoxy mounts were polished to reveal a cross section through the sample at the reference radius of 2/3 used in eq. (1) and (2). Polishing included a final chemo-mechanical step using colloidal silica (0.04 μm particles, and an average polishing duration of 1 – 4 h). Exposed sample surfaces were then carbon coated with a coating thickness of 10-20 nm for SEM images. For EBSD analyses, only the zone surrounding the section of interest was carbon coated. Additionally, a copper-carbon tape was applied on top of the sample to assure conductive connection to the EBSD sample holder.

EBSD maps were obtained with an acceleration voltage of 17 kV, a beam current of 10 nA, a working distance of 25.0 mm and an exposure time of 28.8 ms. Acquired phases were olivine, diopside, enstatite and chromite. EBSD data was acquired with the Oxford instruments HKL Aztec2 software and treated with the MTEX toolbox (Hielscher & Schaeben, 2008; Bachmann et al., 2010). Wild spikes were removed during data treatment and non-indexed pixels filled with neighboring values where 7 neighbors with identical orientations were present. Grain boundaries were defined where the misorientation to the next pixel is higher than 10 °. Grains containing less than 15 indexed pixels were rejected. The density of the orientation distribution function was calculated using an axially symmetric de la

Vallee Poussin kernel, with a half-width of 10° (band-width of 28 in spherical harmonic coefficients). The texture J-index (Bunge, 1982) is a measurement of the texture strength and was calculated as the integral of the square of the orientation distribution function.

V-3 Results

V-3.1 Mechanical data

Out of 33 experiments, 27 showed reproducible data summarized in V-1. Additionally, two experiments have been performed to record the cold press stage of the olivine powder. Mechanical curves of all deformation experiments are shown in Figure V-1. The evolution of friction coefficient as a function of displacement shows four distinct stages: (I) Steep increase of friction to initial values upon acceleration; (II) transient stage with friction increasing to maximum values attained when reaching the targeted deformation speed; (III) rapid decrease of friction, followed by a slowly decreasing plateau toward steady state; and (IV) re-strengthening for samples deformed at 1 ms^{-1} upon deceleration and hence cooling, followed by a sharp drop in friction coefficient for all samples after deformation cylinders have stopped rotating. During stage III, experiments at slip rates of 1 ms^{-1} generally show lower coefficients of friction for given values of displacement than experiments deformed at 10^{-2} ms^{-1}. SC and SB olivine samples which have large grain sizes (70 ± 2 μm) yield similar friction coefficients as $nanoFo_{100}$ (0.07 μm). Deformation at intermediate slip rates of 0.1 ms^{-1} unfortunately resulted in significant loss of powder, inducing continuous dropping of the friction coefficient, and no steady state. We therefore do not further consider these experiments for the discussion.

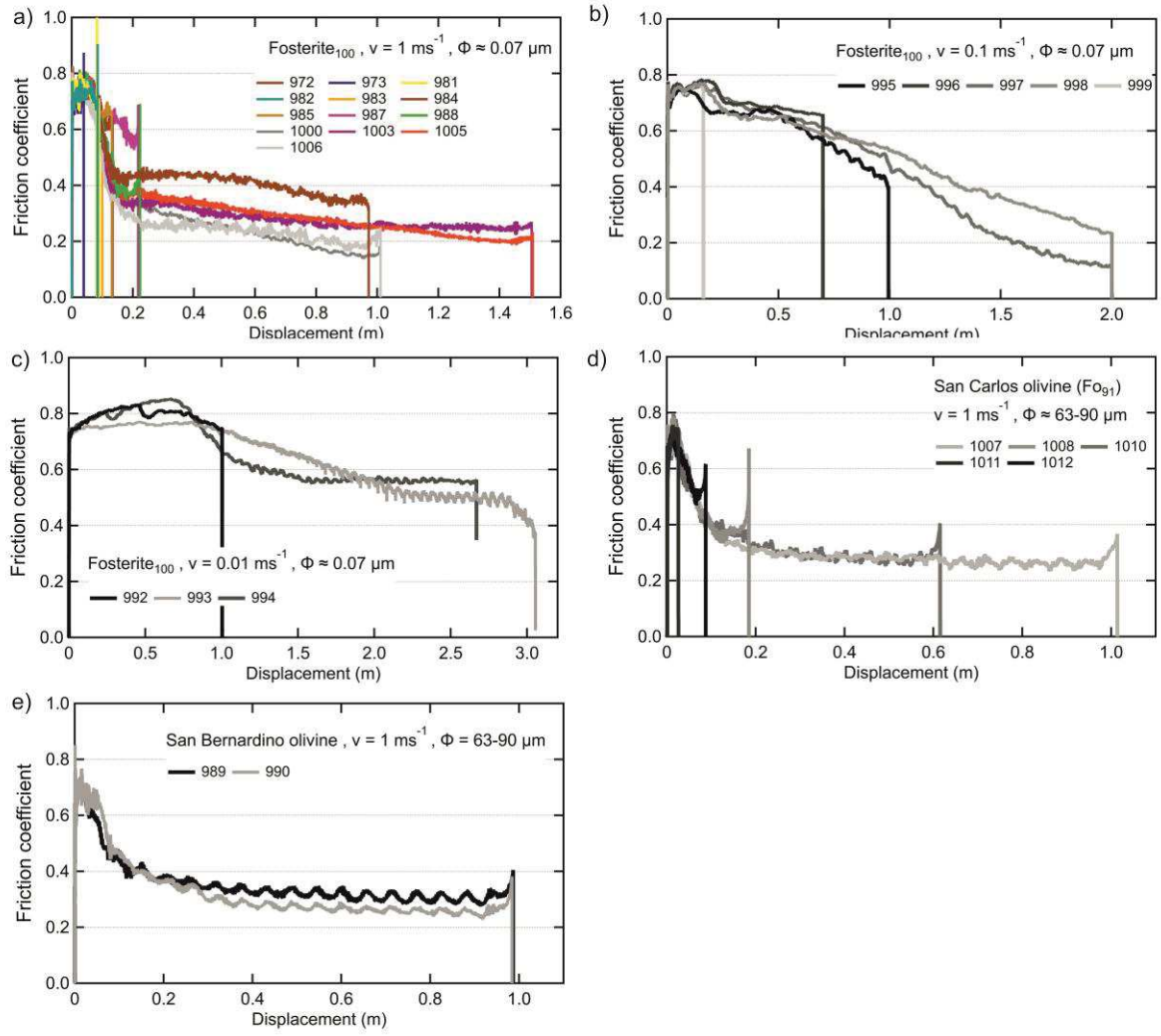

Fig. V-1 Friction coefficient as a function of displacement for (a) nanoFo100 with an average grain size of 0.07 µm deformed at 1 ms^{-1}, (b) nanoFo100 with an average grain size of 0.07 µm deformed at 0.1 m s^{-1}, (c) nanoFo100 with an average grain size of 0.07 µm deformed at 0.01 ms^{-1}, (d) San Carlos olivine with an initial grain size of 70 ± 2 µm deformed at 1 m s^{-1} and (e) San Bernardino olivine with an initial grain size of 70 ± 2 µm deformed at 1 ms^{-1}.

The evolution of calculated temperature (see eq. 4) as a function of displacement and the evolution of the friction coefficient as a function of temperature for sample 1007 are both displayed in Figure V-2. Sample 1007 is representative for all samples deformed at 1 ms^{-1}. Temperature increases steeply (40 °C/cm) until stage III deformation is reached. During stage III, temperature continues to increase non-linearly until deceleration starts. The friction

coefficient is negatively and non-linearly correlated to the calculated temperature during deformation. Upon deceleration, both the temperature and the friction coefficient increase until full stop of the deformation. The noise in Figure V-2b is typical for the high velocity frictional testing apparatus and arises from elastic oscillation of the deformation cylinder and sample assembly, as well as from keeping constant slip velocity.

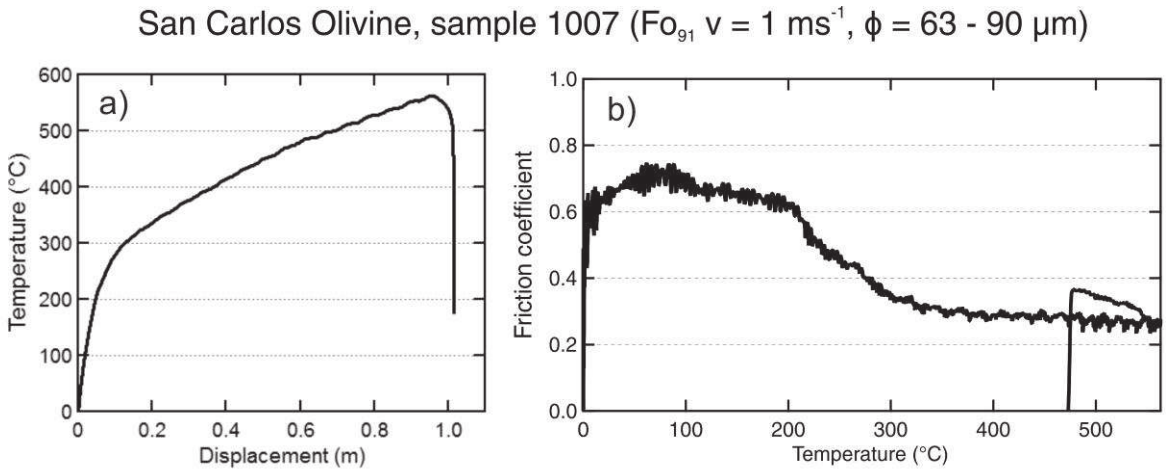

Fig. V-2 (a) Temperature as a function of displacement and (b) friction coefficient as a function of temperature for San Carlos olivine 1007 deformed in torsion at 1 ms^{-1} to 1 m of slip.

Table V-1 Experimental conditions and mechanical results for torsion deformation under an axial stress of 20 MPa at room pressure and temperature.

Conditions						Results												
Sample	Material	Grain size φ (μm)	Slip velocity V (ms^{-1})	Sampling Freq. (kHz)	Target slip d_e (m)	Slip (m)	Stress σ_s (MPa)			Friction coefficient μ			Shear strain γ			Shear strain rate $\dot{\gamma}$ (s^{-1})			Temperature T (°C)
							stage II	early stage III	late stage III	stage II	early stage III	late stage III	stage II	early stage III	late stage III	stage II	early stage III	late stage III	
972	Nano Forst.	~0.07	1	2	1.000	0.97	15.3	-	-	0.76	-	-	134	-	-	38	-	-	400
973	Nano Forst.	~0.07	1	2	0.030	0.04	14.6	-	-	0.73	-	-	130	-	-	26	-	-	124
981	Nano Forst.	~0.07	1	2	0.085	0.08	15.8	-	-	0.79	-	-	117	-	-	24	-	-	216
982	Nano Forst.	~0.07	1	2	0.085	0.08	15.7	-	-	0.78	-	-	215	-	-	47	-	-	209
983	Nano Forst.	~0.07	1	2	0.105	0.1	15.7	-	-	0.78	-	-	180	-	-	59	-	-	237
984	Nano Forst.	~0.07	1	2	0.136	0.11	15.5	-	-	0.77	-	-	181	-	-	61	-	-	362
987	Nano Forst.	~0.07	1	2	0.200	0.21	15.9	-	-	0.79	-	-	89	-	-	29	-	-	302
988	Nano Forst.	~0.07	1	2	0.200	0.19	16.1	-	-	0.80	-	-	156	-	-	50	-	-	403
989	S.B. Olivine	63-90	1	2	1.000	0.94	14.5	8.1	6.6	0.72	0.41	0.33	39	440	3120	10	109	645	636
990	S.B. Olivine	63-90	1	2	1.000	0.93	15	7.8	5.1	0.75	0.39	0.25	49	520	3120	14	139	692	560
992	Nano Forst.	~0.07	1×10^{-2}	1	1.000	1	16.7	-	-	0.83	-	-	1492	-	-	31	-	-	-
993	Nano Forst.	~0.07	1×10^{-2}	0.5	3.000	2.87	15.6	-	10	0.78	-	0.50	2520	-	9560	31	-	33	201
994	Nano Forst.	~0.07	1×10^{-2}	0.5	2.600	2.67	17.2	12.8	11.4	0.86	0.63	0.56	2156	3592	8920	32	33	33	204
995	Nano Forst.	~0.07	1×10^{-1}	5	1.000	0.99	15.1	-	-	0.75	-	-	270	-	-	364	-	-	346
996	Nano Forst.	~0.07	1×10^{-1}	5	0.700	0.70	15.8	-	-	0.79	-	-	165	-	-	814	-	-	364
997	Nano Forst.	~0.07	1×10^{-1}	5	2.000	1.99	15.4	-	-	0.77	-	-	524	-	-	508	-	-	297
998	Nano Forst.	~0.07	1×10^{-1}	5	2.000	1.88	15.6	-	-	0.78	-	-	564	-	-	1662	-	-	379
999	Nano Forst.	~0.07	1×10^{-1}	5	0.160	0.16	15.4	-	-	0.77	-	-	488	-	-	508	-	-	188
1000	Nano Forst.	~0.07	1	5	1.000	0.97	15	7.0	3.1	0.75	0.35	0.15	134	612	3240	196	851	3685	459
1003	Nano Forst.	~0.07	1	5	1.500	1.46	15.8	7.3	5	0.79	0.36	0.25	134	520	4880	57	211	1293	680
1005	Nano Forst.	~0.07	1	5	1.500	1.45	15.8	7.3	3.9	0.79	0.36	0.20	138	564	4800	45	174	1059	655
1006	Nano Forst.	~0.07	1	5	1.000	0.95	15.5	5.7	3.8	0.77	0.28	0.18	170	596	3880	59	198	1025	484
1007	S.C. Olivine	63-90	1	5	1.000	0.97	14.4	6.8	5.1	0.72	0.34	0.25	61	468	3240	23	169	898	557
1008	S.C. Olivine	63-90	1	5	0.170	0.12	15.8	-	-	0.79	-	-	51	-	-	20	-	-	295
1009	S.C. Olivine	63-90	Only compaction recorded																
1010	S.C. Olivine	63-90	1	5	0.600	0.58	16	7.4	5.7	0.80	0.37	0.28	50	480	1960	18	165	582	455
1011	S.C. Olivine	63-90	1	5	0.025	0.03	14.9	-	-	0.74	-	-	54	-	-	22	-	-	84
1012	S.C. Olivine	63-90	1	5	0.090	0.07	14.9	-	-	0.74	-	-	38	-	-	17	-	-	228
1013	Nano Forst.	~0.07	Only compaction recorded																

V-3.2 Microstructures

The miscrostructures were investigated by SEM and EBSD. The large interaction volume of the electron beam (at least several dozen nm depending on the acceleration voltage and the beam current) prevented satisfying detection of Kikuchi patterns and hence prevented analysis of nanoFo$_{100}$ samples by EBSD. Therefore, NanoFo$_{100}$ samples were only analyzed by SEM, including for grain size quantification.

The SC and SB olivine samples, with grain sizes of 70 ± 2 μm, were successfully analyzed by both SEM and EBSD. The composition of San Bernardino olivine was determined by quantitative EDS to be approximately Fo$_{91}$, as given in supplementary material 1. Neither melt, nor any phase except olivine could be identified in significant quantities. A high magnification image of typical grains in SC olivine from near the top of the sample is given in Figure V-3. Grains of up to 40 μm in diameter are surrounded by a finer grained matrix. Larger grains are mostly spherical, but angular to sub-angular with straight boundary segments and often cracked grains, especially along their surface, are also visible. Images from SEM of samples deformed at 1 ms^{-1} and 10^{-2} ms^{-1} are displayed in Figure V-4. The samples with SC and SB olivine are distinguished into a center section of grains remaining at the size of the starting material, and a top layer with significantly reduced grain sizes (as low as 3 ± 1 μm). This layer with reduced grain sizes terminates in a sharp boundary towards the epoxy. The recovered thickness of the fine-grained layer is reduced from 24 μm at 0.07 m of slip (sample 1012) to 8 μm at 1 m of slip (sample 1007). Imaging NanoFo$_{100}$ samples was challenging due to strong electrostatic charging. Grain sizes in the compressed and uncompressed nanoFo$_{100}$ powder before deformation vary between 50 and 100 nm and remain constant during deformation. Even under stage III deformation, grains experience no growth or change in shape. At deformation rates of 1 ms^{-1}, clusters of grains that are not sintered are visible for low values of displacement (up to 0.2 m, early steady state, nanoFo$_{100}$ 984, 987 and

988) near the top close to the highest gradient in strain rate where strain is anticipated to localize. These clusters were also visible in the starting material and do neither appear further in the center, nor in samples deformed to high slip (up to 1 m). Based on SEM images, the samples deformed at slip velocities of 10^{-1} ms^{-1} and 10^{-2} ms^{-1} are similar to the ones deformed at 1 ms^{-1}, but showing no sign of clusters.

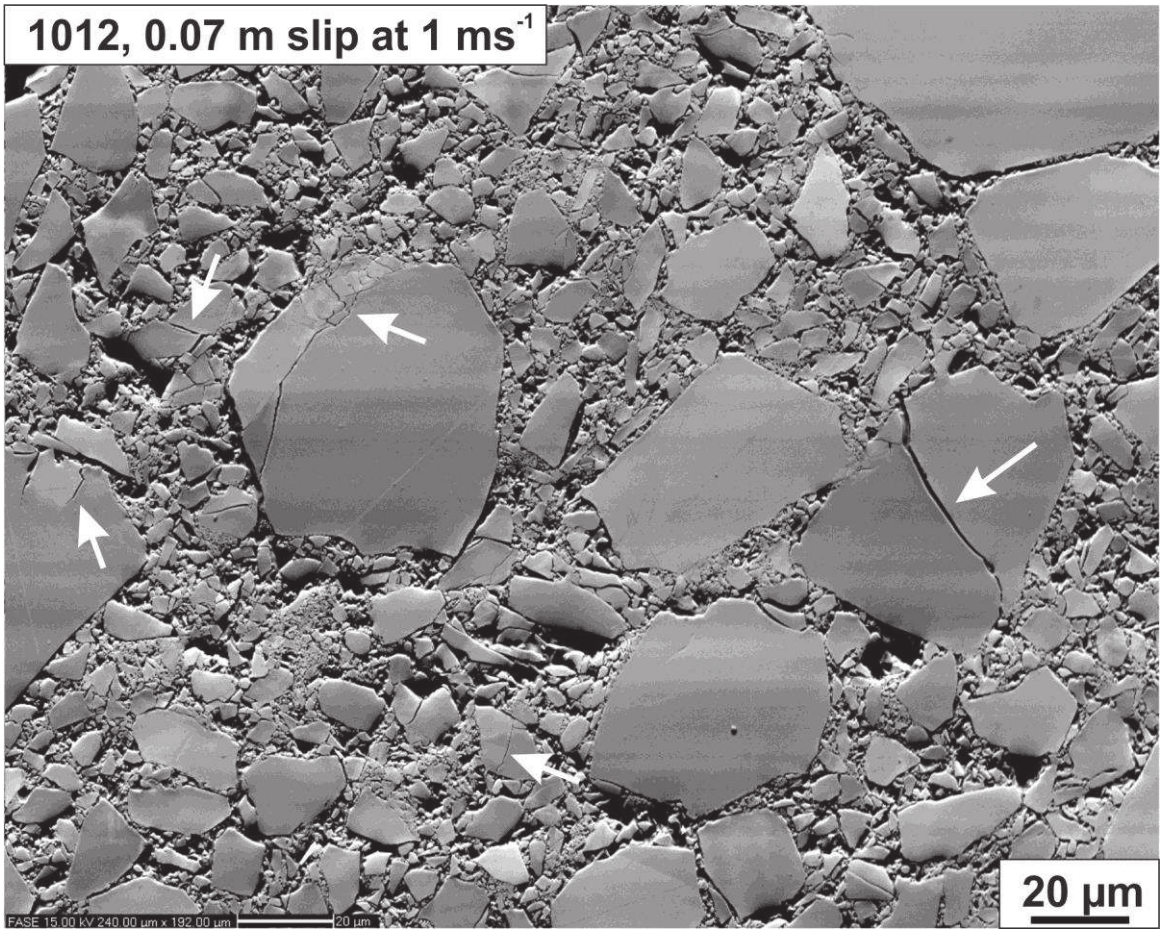

Fig. V-3 Forward scattered electron image from near the fine-grained zone in San Carlos olivine 1012. White arrows highlight fractures.

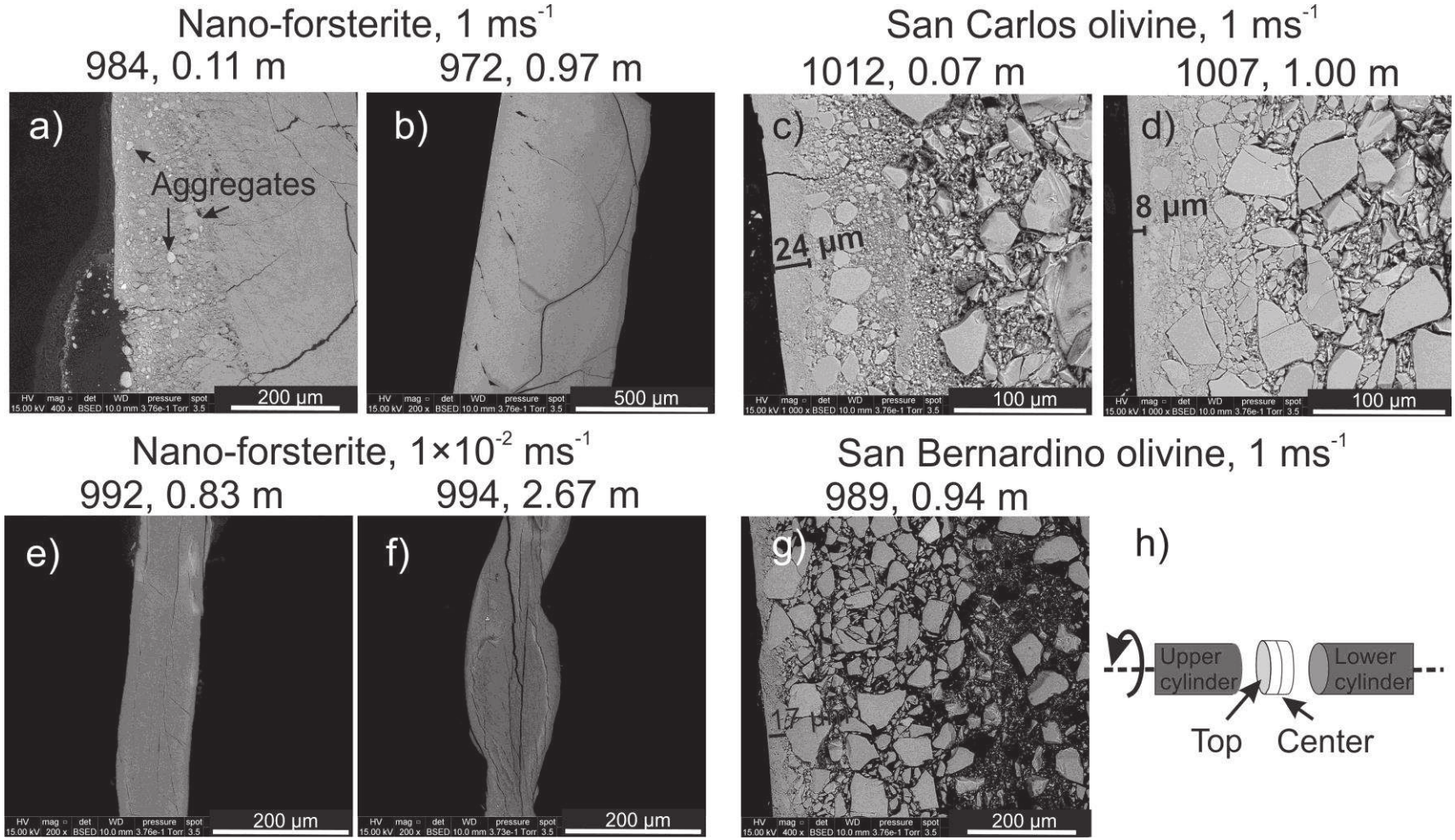

Fig. V-4 Backscattered electron images of samples representing the lowest and highest slip of each group of deformed samples. The top of the sample, which is in contact with the rotating deformation cylinder, is located to the left of the sample.

The microstructural parameters obtained by EBSD maps for SB and SC olivine are listed in Table V-2. Mean grain sizes calculated as the grain equivalent diameter range from 73 µm in the undeformed SC starting material (sample 1009) to as low as 3 µm in SB olivine deformed at high strain rates and to a high slip (sample 989, 1 ms^{-1}, 1 m). All deformed SB and SC samples show important grain size reduction towards the top (towards the rotating upper deformation cylinder). The density of geometrically necessary dislocations is directly related to the activity of dislocation creep. The mean kernel average misorientation (KAM) acts as a proxy for the density of geometrically necessary dislocations (e.g., Nye 1953; Adams 1997; Arsenlis & Park 1999) and ranges from 0.21 ° in the undeformed starting material to 0.84 ° for highly deformed SC olivine (1007, 1 ms^{-1}, 1 m). Cataclastic flow is thought to increase grain roundness, which is reflected by the percentile average relative indented surface boundary (PARIS), a measure of the curvature of grain boundaries. PARIS ranges from 4.03 (sample 1009, SC starting power) to 23.41 (sample 990, 1 ms^{-1}, 1 m). The development of plastically deformed texture strength of our samples is best quantified using a textural J-index (Bunge 1982; integral of the squared orientation distribution function). In our case, EBSD treatment using one point per grain (1PPG) gives results that do not overestimate

Table V-2 Microstructural parameters obtained from EBSD maps for experimental samples with grain sizes of 70 ± 2 µm deformed at 1 ms^{-1}.

Sample	sample area	slip (m)	N grains	mean diameter [a] (µm)	1 σ diameter (µm)	max diameter (µm)	min diameter (µm)	mean PARIS [b]	1 σ PARIS	mean KAM [c] (°)	1 σ KAM (°)	Texture J-index [d] 1ppp	Texture J-index 1ppg
989 T I	Top	0.94	197	4.74	1.38	16.61	2.50	14.88	11.23	0.68	1.86	2.1	1.7
989 T II	Top	0.94	98	4.61	1.37	17.08	2.32	19.65	12.22	0.56	2.00	3.7	1.7
989 T III	Top	0.94	97	2.79	1.47	7.06	1.48	20.41	12.72	0.75	1.82	3.2	1.8
990 T II	Top	0.93	227	2.69	1.42	14.35	1.40	23.41	11.21	0.80	1.74	3.5	1.8
990 C I	Center	0.93	391	13.03	1.67	68.68	5.38	14.12	8.94	0.48	1.86	3.0	1.5
990 C II	Center	0.93	761	12.42	1.65	81.51	5.19	14.69	9.53	0.47	1.90	2.4	1.3
1007 T I	Top	0.97	294	5.53	1.46	27.75	2.38	10.75	8.20	0.84	2.17	11	1.3
1007 C I	Center	0.97	6992	10.00	1.65	98.48	4.51	24.12	12.51	0.26	2.11	4.0	1.1
1008 T I	Top	0.12	88	6.08	1.48	20.23	3.18	8.44	7.97	0.76	2.02	5.7	2.6
1008 T II	Top	0.12	123	2.54	1.35	7.58	1.29	8.24	6.17	0.69	1.83	3.4	4.9
1008 C I	Center	0.12	4740	5.70	1.64	107.15	2.33	17.36	10.67	0.34	2.20	1.7	1.1
1008 C II	Center	0.12	1826	6.08	1.66	82.70	2.29	16.47	9.93	0.31	2.24	2.4	1.1
1009 C I	Compacted Starting Material SC	0.00	59	66.58	1.65	164.68	22.34	4.27	4.90	0.21	1.99	7.1	3.5
1009 C II		0.00	31	72.91	1.43	129.79	35.00	4.03	4.15	0.21	2.15	8.3	5.7
1010 T II	Top	0.58	409	4.46	1.51	40.75	2.34	21.17	12.20	0.57	1.90	5.3	1.4
1011 T I	Top	0.03	505	12.81	1.49	71.50	5.65	7.04	5.59	0.24	2.21	2.6	1.3
1011 C I	Center	0.03	1349	7.75	1.59	61.61	2.60	9.36	8.67	0.46	2.18	2.2	1.1
1012 T I	Top	0.07	101	2.87	1.35	5.22	1.45	6.34	5.24	0.75	1.74	2.6	2.4
1012 C I	Center	0.07	70	6.28	1.37	20.61	3.99	6.16	5.27	0.73	1.92	6.2	3.0

a The grain size is calculated as the geometric mean of the log-normal distribution of the grain equivalent diameter (i.e., diameter of a sphere with equivalent area).
b PARIS: Percentile average relative indented surface boundary, measure of the curvature of grain boundaries. A high PARIS indicates highly curved or indented boundaries.
c KAM: Geometric mean of the log-normal distribution of the Kernel Average Misorientation (proxy for density of Geometrically Necessary Dislocations), 2nd order, threshold of 5°.
d One point per pixel (1ppp) uses every map pixel with an olivine orientation for the calculation of the texture j-index (Bunge 1982; integral of the squared orientation distribution function). One point per grain (1ppg) uses the mean orientation of each grain.

the few large grains in the sample. J-index (1PPG) ranges from 1.1 in highly deformed sample 1007 (0.97 m slip) to 5.7 in the compacted starting material.

Compared to the starting material, the center section of sample 1011, deformed to a low slip of 0.025 m, already shows a significant reduction in grain size (73 μm to 8 μm) and an increase in KAM values from 0.21 to 0.46 °, as well as in PARIS values (from 4.03 to 9.36). Furthermore, the top layer (most deformed) of each sample always shows a significantly lower grain size (as low as 3 ± 1 μm), and also higher KAM and PARIS than their respective samples center as reported in Table V-2.

V-4 Discussion

V-4.1 Mechanism of deformation

The friction coefficients from this study and previous experiments in torsion at seismic slip rates are compiled in Figure V-5. Most of the existing data are limited to felsic, metamorphic or carbonate rocks. Nevertheless, the friction coefficients from our experiments are in agreement with previous mechanical data obtained on peridotite and other rock types. The frictional strength of our monophase samples reaches higher values of up to 0.33 than data from Del Gaudio et al. (2009) and Di Toro (2006b) who used natural peridotites from Balmuccia (Italy) with grain sizes between 0.5 and 1 mm.

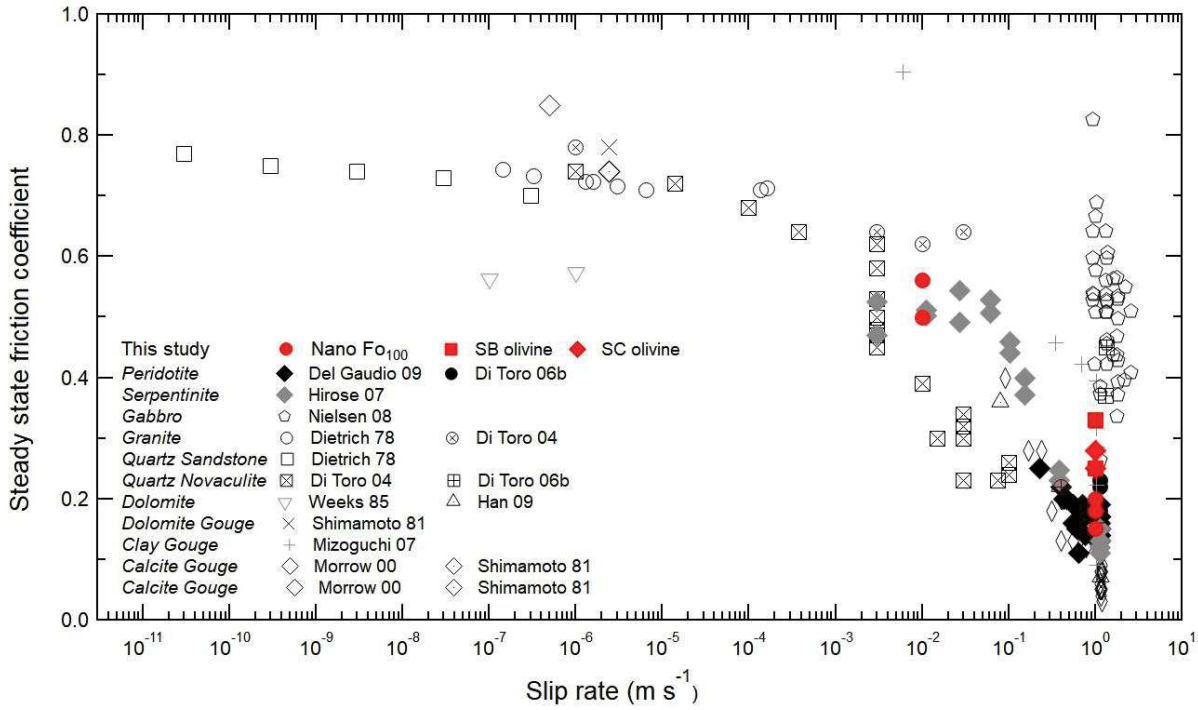

Fig. V-5 Evolution of friction coefficient with log slip rate. Bright red markers are from Olivine of this study. There is a marked decrease in the friction coefficient after slip rates of approximately 10-3 ms-1. Data from Dietrich et al. 1978, Shimamoto et al. (1981), Weeks et al. (1985), Morrow et al. (2000), Di Toro et al. (2004), Di Toro et al. (2006b), Hirose et al. (2007), Mizoguchi et al. (2007), Nielsen et al. (2008) and Del Gaudio et al. (2009).

Fracturing of grains can often be seen in high magnification SEM images. Grains are oriented with their long axis parallel to the shear axis as illustrated in Figure V-6 and PARIS values are reduced (hence grain roundness increases). Thus, we conclude that the dominant deformation mechanism active during stage I and stage II deformation is brittle, i.e. cataclastic flow (Sibson 1977, 1986; Blenkinsop 2000). Cataclastic flow also leads to the strong grain size reduction close to the highest strain rate gradient – in the top layer of the sample. Additionally, cataclastic flow is thought to reduce texture strength, which is observed in our samples after a very low slip of 0.03 m.

Increasing dislocation density as a function of slip hints at an early onset of dislocation creep. Dislocation creep seems to be preferentially active in the fine-grained top layer as evidenced by a higher KAM values than in the center section. The sharp boundary of the top layer towards the epoxy can be described as a mirror surface. It is unclear if this top layer represents the immediate vicinity of the actual principal slip zone (e.g. Smith et. al. 2011) or if the principal slip zone is partially lost during sample removal from the PTFE holder and/or sample preparation. Likewise, the apparent reduction in the thickness of the top layer from 24 µm to 8 µm (sample 1012 and 1007) might be related to sample preparation and/or thickness of the primary slip zone.

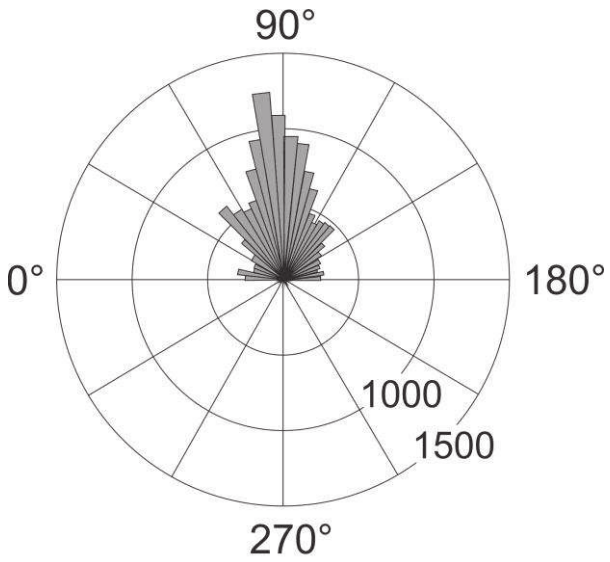

Fig. V-6 Rose diagram of the orientation of the long axis of the olivine grains to the shear axis. The sample of San Carlos olivine (1007) was deformed at 1 ms^{-1} to 1 m of slip and is representative for all deformed samples.

V-4.2 Origin of weakening

The friction coefficient in the literature data significantly decreases above slip rates of 10^{-4} ms^{-1}, implying a temperature-induced weakening deformation mechanism. Del Gaudio et al. (2009) previously reported frictional melting in Balmuccia peridotites (av. grain size of 0.7 mm) experimentally deformed in rotary shear to 2 m of slip at 0.92 ms^{-1}, under axial stress of 13 MPa. In the study by Del Gaudio et al. (2009), the authors report a range of constant calculated temperature between 1100 and 1300 °C, achieved after about 20 m of slip. The maximum homologous temperature $T_H = 0.39$ achieved in this study is significantly below the melting temperature of Fo_{90}, Tm = 1771 °C (at 20 MPa, Bowen and Shairer, 1935; Wang, 2016; T_m of Fo_{100} = 1896 °C). Additionally, here the material strength does not seem to depend on the chemical composition. Samples deformed in axial compression (without torsion) at lower strain rates than here and with comparable or higher temperatures show significantly higher stresses (e.g. Evans & Goetze, 1979; Demouchy et al., 2014; Thieme et al., 2018) than the stresses reported in Table V-1. Therefore, there must be a change in either microstructure or deformation mechanism at the high strain rates and temperatures of our experiments.

Based on EDS analyses of the deformed samples, we could not observe phase reactions or phase decomposition. In conclusion, thermal decomposition. melting and *a priori* presence of weak phases or phase transition can be excluded as possible frictional weakening mechanisms in olivine deformed at our conditions. Thus, we conclude that frictional heating and change of microstructure (mostly grain size and microcracks) lead to the reduction in friction coefficient below Byerlee's values.

The onset of weakening occurs after a slip of about 0.1 m and at speeds of 0.01 ms^{-1}, fitting with observations that seismic-stress reduction occurs over at least 6 orders of magnitude in fault dimension (i.e. meter to 100 km scale; Marone, 2004) and hence a large range in earthquake magnitude. This furthermore implies that the mechanisms of weakening

are likewise similar for small and large earthquakes. Therefore, we suggest that only faults in olivine-rich rocks which (1) creep aseismically (at low slip rates and hence high friction), (2) consist of multiple phases reducing the bulk melting temperature and (3) show slip in the scale of >> 2 m can generate melting. Our data furthermore solidify that no threshold of earthquake magnitude is required for frictional weakening.

V-5 Conclusion

Nano- (0.07 µm) to micro sized (70 µm) olivine aggregates have been deformed at seismic slip rates up to 1 ms^{-1} in rotary shear. Both mechanical data as well as microstructure have been characterized as a function of grain size, slip rate, chemistry and slip. Our main results are the following:

- At slip rates of 1 ms^{-1}, friction coefficients drop from 0.8 to < 0.4, independent of initial grain size and iron content.
- Displacements as low as 0.1 m are sufficient to cause a reduction of the friction coefficient to 0.3.
- Deformation at seismic slip rates activates a temperature sensitive mechanism that induces rapid grain size reduction.
- The density of geometrically necessary dislocations is increasing in all stages of deformation, but dislocation creep can not explain the achieved strain rates alone.
- Cataclastic flow is responsible for the initial grain size reduction and increased rounding.

Acknowledgments

This project received funding from the European Union's Horizon 2020 research and innovation program under the Marie Sklodowska-Curie Grant agreement No. 642029. We thank C. Nevado and D. Delmas for providing high-quality thin sections for SEM and TEM. We are grateful to G. Di Toro for providing a dataset helping to shape Figure V-5.

References

Adams, B.L., 1997. Orientation imaging microscopy: Emerging and future applications. Ultramicroscopy 67 (1-4), 11–17. doi:10.1016/s0304-3991(96)00103-9

Andersen, T.B. & Austrheim, H. 2006: Fossil earthquakes recorded by pseudotachylytes in mantle peridotite from the Alpine subduction complex of Corsica, Earth Planet. Sc. Lett. 242, 58–72. doi:10.1016/j.epsl.2005.11.058

Andersen, T.B., Mair, K.. Austrheim, H., Podladchikov, Y.Y. and Vrijmoed, J.C., 2008. Stress release in exhumed intermediate and deep earthquakes determined from ultramafic pseudotachylyte, Geology 36, 995–998, doi:10.1130/G25230A.1.

Arsenlis, A, Parks, D.M, 1999. Crystallographic aspects of geometrically-necessary and statistically-stored dislocation density. Acta Materialia. 47 (5), 1597–1611. doi:10.1016/s1359-6454(99)00020-8

Bachmann, F., Hielscher, R., Schaeben, H., 2010. Texture analysis with MTEX – Free and open source software toolbox. Solid State Phenom. 160, 63–68. http://dx.doi.org/10.4028/www.scientific.net/SSP.160.63.

Buening, D.K., Buseck, P.R., 1973. Fe-Mg lattice diffusion in olivine. J. Geophys. Res. 78, 6852–6862. http://dx.doi.org/10.1029/JB078i029p06852.

Bunge, H.-J., 1982. In: Texture Analysis in Materials Science. Butterworths, London, pp. 593

Beeler, N. M., T. E. Tullis, M. Blanpied, and J. Weeks (1996), Frictional behavior of large displacement experimental faults, J. Geophys. Res., 101(B4), 8697 – 8715, doi:10.1029/96JB00411.

Blenkinsop, T., 2000. Deformation Microstructures and Mechanisms. Springer. p. 150.

Bolognesi, F., & Bistacchi, A., 2018. A km-scale "triaxial experiment" reveals the extreme mechanical weakness and anisotropy of mica-schists (Grandes Rousses Massif, France). Journal of Structural Geology, 107, 53–63. https://doi.org/10.1016/J.JSG.2017.12.001

Bouchon, M., and P. Ihmle, 1999. Stress drop and frictional heating during the 1994 deep Bolivia earthquake, Geophys. Res. Lett., 26(23), 3521–3524, doi:10.1029/1999GL005410

Bowen, N.L. & Schairer, J.F., 1935. Preliminary report on equilibrium-relations between feldspathoids, alkali-feldspars, and silica. Transactions, American Geophysical Union 16: doi: 10.1029/TR016i001p00325. issn: 0002-8606.

Braeck, S., and Podladchikov, Y.Y., 2007. Spontaneous thermal runaway as an ultimate failure mechanism of materials, Phys. Rev. Lett. 98, 095504–095508, doi:10.1103/PhysRevLett.98.095504.

Bridgman, P. W., 1936. Shearing phenomena at high pressure of possible importance for geology, J. Geol. 44, 653– 669.

Byerlee, J. D., 1978. Friction of rocks. Pure Appl. Geophys. 116, 615–626.

Carpenter, B. M., Marone, C., & Saffer, D. M., 2011. Weakness of the San Andreas Fault revealed by samples from the active fault zone. Nature Geoscience 4(4), 251–254. https://doi.org/10.1038/ngeo1089

Cocco, M. & Tinti, E, 2008. Scale dependence in the dynamics of earthquake propagation: evidence from seismological and geological observations. Earth Planet. Sci. Lett. 273, 123–131.

Crameri, F., Schmeling, H., Golabek, G. J., Duretz, T., Orendt, R., Buiter, S. J., May, D. A., Kaus, B. J., Gerya, T. V. and Tackley, P. J., 2012. A comparison of numerical surface topography calculations in geodynamic modelling: an evaluation of the 'sticky air' method. Geophysical Journal International 189, 38-54. doi:10.1111/j.1365-246X.2012.05388.x

Crameri, F., and Tackley, P.J., 2015. Parameters controlling dynamically self - consistent plate tectonics and single - sided subduction in global models of mantle convection. J. Geophys. Res. Solid Earth 120, 3680–3706. doi: 10.1002/2014JB011664.

De Paola, N, Hirose, T, Mitchell, T, Di Toro, G, Viti, C & Shimamoto, T, 2011. Fault lubrication and earthquake propagation in thermally unstable rocks. Geology 39(1), 35-38.

De Paola, N., Holdsworth, R. E., Viti, C., Collettini, C. & Bullock, R., 2015. Can grain size sensitive flow lubricate faults during the initial stages of earthquake propagation? Earth and Planetary Science Letters 43, 48-58.

Del Gaudio, P., Di Toro, G., Han, R., Hirose, T., Nielsen, S., Shimamoto, T., & Cavallo, A., 2009. Frictional melting of peridotite and seismic slip. Journal of Geophysical Research 114(B6), B06306. https://doi.org/10.1029/2008JB005990

Di Toro, G., Goldsby, D. L. & Tullis, T. E, 2004. Friction falls towards zero in quartz rock as slip velocity approaches seismic rates. Nature 427, 436–439.

Di Toro, G. & Hirose, T. Nielsen, S. Pennacchioni, G. & Shimamoto, T, 2006a. Natural and experimental evidence of melt lubrication of faults during earthquakes. Science 311, 647–649.

Di Toro, G., Hirose, T., Nielsen, S. & Shimamoto, T., 2006b. Relating High - Velocity Rock - Friction Experiments to Coseismic Slip in the Presence of Melts in Radiated Energy and the Physics of Faulting (eds Abercrombie, R., McGarr, A., Di Toro, G. & Kanamori, H.) 121–134 (Geophys. Monogr. Ser. 170, American Geophysical Union).

Di Toro, G., Han, R., Hirose, T., De Paola, N., Nielsen, S., Mizoguchi, K., Ferri, F., Cocco, M., Shimamoto, T., 2011. Fault lubrication during earthquakes. Nature 471(7339), 494–499. https://doi.org/10.1038/nature09838

Demouchy, S., 2010. Diffusion of hydrogen in olivine grain boundaries and implications for the survival of water-rich zones in the Earth's mantle. Earth Planet. Sci. Lett. 295, 305–313. http://dx.doi.org/10.1016/j.epsl.2010.04.019.

Demouchy, S., Mussi, A., Barou, F., Tommasi, A., Cordier, P., 2014. Viscoplasticity of polycrystalline olivine experimentally deformed at high pressure and 900°C. Tectonophysics 623, 123–135. http://dx.doi.org/10.1016/j.tecto.2014.03.022.

Evans, B., Goetze, C., 1979. The temperature variation of hardness of olivine and its implication for polycrystalline yield stress. J. Geophys. Res. 84, 5505–5524.

Ferri F., Di Toro G., Hirose T., Shimamoto T., 2010. Evidences of thermal pressurization in high velocity friction experiments on smectite-rich gouges. Terra Nova 22, pp. 347-353

Frey, F.A., Prinz, M., 1978. Ultramafic inclusions from san carlos, Arizona: petrologic and geochemical data bearing on their petrogenesis. Dev. Petrol. 5, 129–176. http://dx. doi.org/10.1016/B978-0-444-41658-2.50013-4.

Goldsby, D. L. & Tullis, T. E, 2002. Low frictional strength of quartz rocks at subseismic slip rates. Geophys. Res. Lett. 29, 1844.

Goldsby, D. L. & Tullis, T.E, 2011. Flash Heating Leads to Low Frictional Strength of Crustal Rocks at Earthquake Slip Rates. Science, 216-218

Griggs, D., & J. Handin, 1960. Observations on fracture and a hypothesis of earthquakes. Geol. Soc. Am. Mem. 79, 343– 373.

Han, R., Shimamoto, T., Hirose, T., Ree, J.-H.& Ando, J, 2007. Ultralow friction of carbonate faults caused by thermal decomposition. Science 316, 878–881.

Heaton, T. H., 1990. Evidence for and implications of self-healing pulses of slip in earthquake rupture. Phys. Earth Planet. Inter. 64, 1–20.

Hielscher, R., Schaeben, H., 2008. A novel pole figure inversion method: specification of the MTEX algorithm. J. Appl. Crystallogr. 41, 1024–1037. http://dx.doi.org/10. 1107/S0021889808030112.

Hirose, T. & Shimamoto, T., 2005. Growth of molten zone as a mechanism of slip weakening of simulated faults in gabbro during frictional melting. J. Geophys. Res. 110, B05202.

John, T., Medvedev, S., Rüpke, L.H., Andersen, T.B., Podladchikov, Y.Y., Austrheim, H., 2009. Generation of intermediate-depth earthquakes by self-localizing thermal runaway. Nat. Geosci. 2, 137 – 140, doi:10.1038/ngeo419

Kanamori, H., D. L. Anderson, and T. H. Heaton, 1998. Frictional melting during the rupture of the 1994 Bolivian earthquake. Science 279, 839–842, doi:10.1126/science.279.5352.839.

Kelemen, P. B., and G. Hirth, 2007. A periodic shear-heating mechanism for intermediate-depth earthquakes in the mantle. Nature 446, 787– 790, doi:10.1038/nature05717

Koizumi, S., Hiraga, T., Tachibana, C., Tasaka, M., Miyazaki, T., Kobayashi, T., Takamasa, A., Ohashi, N., Sano, S., 2010. Synthesis of highly dense and fine-grained aggregates of mantle composites by vacuum sintering of nano-sized mineral powders. Physics and Chemistry of Minerals, 37(8), 505–518. https://doi.org/10.1007/s00269-009-0350-y

Lynch, D. J., 1978. The San Bernadino volcanic field of southeastern Arizon. in: Land of Cochise (Southeastern Arizona), Callender, J. F.; Wilt, J.; Clemons, R. E.; James, H. L.; [eds.], New Mexico Geological Society 29th Annual Fall Field Conference Guidebook, 348 p.

Ma, S., Shimamoto, T., Yao, L., Togo, T., & Kitajima, H., 2014. A rotary-shear low to high-velocity friction apparatus in Beijing to study rock friction at plate to seismic slip rates. Earthquake Science 27(5), 469–497. https://doi.org/10.1007/s11589-014-0097-5

Mackwell, S.J., Kohlstedt, D.L., Paterson, M.S., 1985. The role of water in the deformation of olivine single crystals. J. Geophys. Res. 90, 11319. http://dx.doi.org/10.1029/JB090iB13p11319.

Maerten, F., Madden, E. H., Pollard, D. D., & Maerten, L., 2016a. Incorporating fault mechanics into inversions of aftershock data for the regional remote stress, with application to the 1992 Landers, California earthquake. Tectonophysics 674, 52–64. https://doi.org/10.1016/j.tecto.2016.01.032

Maerten, L., Maerten, F., Lejri, M., & Gillespie, P., 2016b. Geomechanical paleostress inversion using fracture data. Journal of Structural Geology 89, 197–213. https://doi.org/10.1016/j.jsg.2016.06.007

Marone, C., 2004. Faults greased at high speed. Nature 427, 405-406.

Mei, S., Kohlstedt, D., 2000. Influence of water on plastic deformation of olivine aggregates 1. Diffusion creep regime. J. Geophys. Res. 105, 21457–21469.

Mizoguchi, K., Hirose, T., Shimamoto, T. & Fukuyama, E., 2009. High-velocity frictional behavior and microstructure evolution of fault gouge obtained from Nojima fault, southwest Japan. Tectonophysics 471, 285–296.

Nakagawa, T., and P. J. Tackley, 2015. Influence of plate tectonic mode on the coupled thermochemical evolution of Earth's mantle and core. Geochem. Geophys. Geosyst. 16, 3400–3413, doi: 10.1002/2015GC005996.

Neville, S. L., Schiffman, P., Sadler, P., 1985. Ultramafic inclusions in late Miocene alkaline basalts from Fry and Ruby Mountains, San Bernardino Country, California. Am. Min. 70, 668-677

Nielsen, S. & Di Toro, G, Hirose, T., Shimamoto, T., 2006. Constitutive law for melt lubrication on earthquakes faults. AGU Fall Meeting Abstracts.

Nye, J.F, 1953. Some geometrical relations in dislocated crystals. Acta Metallurgica. 1 (2): 153–162. doi:10.1016/0001-6160(53)90054-6

Obata, M., and S. Karato, 1995. Ultramafic pseudotachylite from the Balmuccia peridotite, Ivrea Verbano Zone, northern Italy. Tectonophysics 242, 313– 328, doi:10.1016/0040-1951(94)00228-2.

Ogawa, M., 1987. Shear instability in a viscoelastic material as the cause of deep focus earthquakes. J. Geophys. Res. 92(B13), 13,801– 13,810, doi:10.1029/JB092iB13p13801

Piccardo, G.B., Coltorti, M., Grégoire, M., 2008. The Jurassic Ligurian Tethys, a fossil ultra-slow spreading ocean: the mantle perspective, Metasomatism in Oceanic and Continental Lithospheric Mantle. Geological Society, London, Special Publications 293 (pg. 11-33).

Pozzi, G., De Paola, N., Nielsen, S.B., Holdsworth, R.E. & Bowen, L., 2018. A new interpretation for the nature and significance of mirror-like surfaces in experimental carbonate-hosted seismic faults. Geology 46(7): 583-586.

Reches, Z. & Lockner, D.A., 2010. Fault weakening and earthquake instability by powder lubrication. Nature 467, 452–455.

Rice, J. R, 2006. Heating and weakening of faults during earthquake slip. J. Geophys. Res. 111, B05311.

Saffer, D. M., Bekins, B. A., & Hickman, S., 2003. Topographically driven groundwater flow and the San Andreas heat flow paradox revisited. Journal of Geophysical Research: Solid Earth 108(B5), 405–406. https://doi.org/10.1029/2002JB001849

Scholz, C. H., 2000. Evidence for a strong San Andreas fault. Geology 28: 163–166

Scholz, C. H., 2002. The Mechanics of Earthquakes and Faulting. Cambridge Univ. Press.

Sibson, R.H., 1977. Fault rocks and fault mechanisms. Journal of the Geological Society. 133 (3): 191–213. doi:10.1144/gsjgs.133.3.0191

Sibson, R.H., 1986. Brecciation processes in fault zones: Inferences from earthquake rupturing. Pure and Applied Geophysics. 1241 (1–2): 159–175. doi:10.1007/BF00875724

Smith, S.A.F., Billi, A. Di Toro, G., Spiess, R., 2011. Principal slip zones in limestone: microstructural characterization and implications for the seismic cycle (Tre Monti fault, central Apennines, Italy). Pure Appl. Geophys. 168, pp. 2365-2393

Thieme, M., Demouchy, S., Mainprice, D., Barou, F., & Cordier, P., 2018. Stress evolution and associated microstructure during transient creep of olivine at 1000–1200 °C. Physics of the Earth and Planetary Interiors 278, 34–46. https://doi.org/10.1016/j.pepi.2018.03.002

Wang, L., S. Blaha, Z. Pintér, R. Farla, T. Kawazoe, N. Miyajima, K. Michibayashi, T. Katsura, 2016. Temperature dependence of [100](010) and [001](010) dislocation mobility in natural olivine. Earth Planet. Sci. Lett. 441, pp. 81-90

Chapter VI – Conclusion

Summary, implications for the lithospheric mantle and perspectives.

This thesis consists of a series of studies aiming to improve our understanding of the atomistic processes involved during deformation of uppermost mantle rocks. Our aims were to investigate deformation mechanisms affecting the strength of rocks at conditions relevant for the lithospheric mantle. To this end, we:

- (1) Provide a fully characterized dataset of the mechanical strength and corresponding microstructure of olivine at 1000 °C and 1200 °C.
- (2) Investigate the mechanisms active during viscous deformation of uppermost mantle rocks.
- (3) Constrain the extrapolation of experimental data to strain-rates of the lithospheric mantle.
- (5) Quantify the frictional strength of polycrystalline olivine deformed under seismic slip rates.
- (6) Investigate potential rate weakening mechanisms responsible for the reduction in frictional strength occuring during deformation at seismic slip rates.
- (7) Characterize and quantified dislocation and disclination densities and geometries in deformed polycrystalline olivine and decipher their influence on the strength.

We found that the strength of polycrystalline olivine deformed at 1000 °C and strain rates of $10^{-5}s^{-1}$ is surpassing predictions of most previously published low-temperature flow laws, achieving the best fit with the flow law of Tielke et al. (2016; shear on [001](100)). Maximum stresses exceeded 1127 MPa before samples failure is partially due to microfracturing without achieving mechanical steady state. Deformation at 1200 °C achieves mechanical steady state at stresses of about 320 MPa and agrees well with classical high temperature flow laws from Keefner et al. (2011), Tielke et al. (2016, shear on [100](001)) and Hirth and Kohlstedt (2003). Although the mechanical strength depends on temperature, strain rate and (possibly) grain size for diffusion creep or grain boundary mediated plasticity, the evolution of stress during deformation was found uncorrelated with the deformed microstructure (or texture). The constant grain sizes, the absence of change in grain shape and achieved maximum stresses hint at dislocation creep controlling the rheology of olivine deformed at these conditions. In a novel observation, we report a sizeable subset of grains remaining free of internal misorientation including during early mechanical steady state, implying that strain in polycrystals is predominantly accommodated by grains in favourable orientations. Since the strengths of our samples deformed at 1000 °C are significantly lower

than predictions deduced from high temperature 'powder' flow laws, no additional water weakening mechanism or partial melting is needed to achieve low viscosities needed for earth-like geodynamic models of plate tectonics. When extrapolated to strain rates of Earth's mantle (10^{-4} s^{-1}) and temperatures below 1000 °C, the strength of olivine-rich rocks of 0.5 to 1 GPa is sufficiently high to upkeep orogens for millions of years. In spite of providing the highest resolution orientation data for olivine to date (0.05 μm EBSD step size), it remains unclear what causes strain localization and strain hardening in fine-grained olivine rocks. We propose the development of novel methods, which allow *in situ* and *ex situ* investigation of grain boundaries on the nanoscopic scale. Furthermore, deformation experiments at similar conditions but with larger grain sizes (500 μm) might exclude mechanisms specific to small grains (e.g., Hall-Petch effect) and aid extrapolation to conditions in Nature.

Powders of olivine deformed at seismic slip rates (0.01 – 1 ms^{-1}) show a contrasting behaviour to strain hardening seen during deformation at lower velocities – as strain increases, the frictional strength as expressed by the coefficient of friction decreases significantly from 0.8 to less than 0.4. The final strength does not depend on the initial grain size and iron content, and barely from the mineral phase. During deformation, strain localizes in a shear zone of a few dozen μm thickness. In this zone, cataclastic flow reduces grain sizes drastically from 70 ± 2 μm to 13 ± 1 μm after only 0.03 m of slip and 3 ± 1 μm after 0.07 m of slip. Grains in the less deformed center of the sample likewise reduce in grain size, albeit in a less significant manner (i.e., 6 ± 1 μm after 0.07 of slip). Similarly, the coefficient of friction decreases from 0.8 to 0.3 after only 0.1 m of slip. This suggests a possible fault lubrication process in Nature which does not require preexisting weak layers or fault reactivation. As a consequence, we suggest that only faults in olivine-rich rocks, which creep aseismically (at low slip rates and hence high friction), which consist of multiple phases reducing the bulk melting temperature and which show slip in the scale of >> 2 m generate melting.

Contrary to previous studies investigating the microstructure of geo-materials deformed at high velocity, olivine has a significantly higher melting point. Since our experiments were performed on nearly pure olivine and achieved homologous temperatures of < 0.39, we can exclude several previous mechanisms proposed to be responsible for weakening during deformation at seismic slip rates: diffusion creep, partial melting and phase reactions or phase changes. The mechanism responsible for the reduction in frictional strength

remains elusive. Future experiments might be optimized by performing torsion under higher confining pressures (e.g. 300 MPa to allow comparison to existing experiments deformed in axial compression) and temperatures, which requires a novel experimental deformation setup.

Similar to results presented in Chapter I, the disclination density does not depend on the stress, strain temperature and density of geometrically necessary dislocations. Additionally, disclinations appear as dipoles, but also as monopoles, mostly located at triple junctions. The presence of these monopoles introduces large elastic lattice strains that could impedes the movement of defects. Disclinations might therefore provide a mechanism explaining the Hall-Petch relationship, where the mechanical strength increases with reduced grain size. To the contrary, such disclinations provide a way to bridge incompatibilities in the elastic rotation field, readily providing a complementary mechanism to dislocation glide by inducing grain boundary migration, and possibly to grain boundary sliding as well. Since a single disclination only allows rotation of a volume of a few nm^3, they might contribute to grain size reduction during low temperature deformation (i.e., no significant diffusion) in the commonly occurring in the lithospheric mantle. Furthermore, investigating the interplay between disclinations and disclocations, especially dislocation walls, as well as mapping the disclination density in samples which contain rotation markers might help in the future to show if disclinations are quantitatively sufficient as a complementary mechanism to deformed plastically mantle rocks.

References

Ashcroft, N.W., Mermin, N.D., 1976. Solid state physics. Harcourt, Orlando, 826 pp.

Bai, Q., Mackwell, S.J. & Kohlstedt, D.L., 1991. High-temperature creep of olivine single crystals - 1. Mechanical results for buffered samples. J. Geophys. Res. 96(B2), 2441-63.

Beausir, B., Fressengeas, C., 2013. Disclination densities from EBSD orientation mapping. Int. J. Solids Struct. 50, 137–146.

Benzerga, A.A., Besson, J., Pineau, A., 2004. Anisotropic ductile fracture. Part II: Theory. Acta Materialia 52, 4639-4650.

Birle, J.D., Gibbs, G.V., Moore, P.B., Smith, J.V., 1968. Crystal structures of natural olivines. American Mineralogist 53, p.807-824.

Boioli, F., Carrez, P., Cordier, P., Devincre, B., Marquille, M., 2015. Modeling the creep properties of olivine by 2.5-dimensional dislocation dynamics simulations. Phys. Rev. B 92, 1–12. http://dx.doi.org/10.1103/PhysRevB.92.014115.

Bolognesi, F., & Bistacchi, A., 2018. A km-scale "triaxial experiment" reveals the extreme mechanical weakness and anisotropy of mica-schists (Grandes Rousses Massif, France). Journal of Structural Geology, 107, 53–63. https://doi.org/10.1016/J.JSG.2017.12.001

Brace, W.F., Kohlstedt, D.L. 1980. Limits on lithospheric stress imposed by laboratory experiments. J. Geophys. Res. 84, 6248–52.

Buening, D.K., Buseck, P.R., 1973. Fe-Mg lattice diffusion in olivine. J. Geophys. Res. 78, 6852–6862. http://dx.doi.org/10.1029/JB078i029p06852.

Burov, E.B., Watts, A.B., 2006. The long-term strength of continental lithosphere: "jelly sandwich" or "crème brûleé"?. GSA Today 12, 4–10.

Bürgmann, R., Dresen, G., 2008. Rheology of the Lower Crust and Upper Mantle: Evidence from Rock Mechanics, Geodesy, and Field Observations. Ann. Rev. Earth Plan. Sci., 36, 531-567.

Byerlee, J. D., 1978. Friction of rocks. Pure Appl. Geophys. 116, 615–626.

Chen, S., Hiraga, T. & Kohlstedt, D.L., 2006. Water weakening of clinopyroxene in the dislocation creep regime. J. Geophys. Res. 111(B8), 2156-202.

Chester, F.M., Evans, J.P., Biegel, R.L. (1993). Internal structure and weakening mechanisms of the San Andreas fault. Journal of Geophysical Research 98, doi: 10.1029/92JB01866. issn: 0148-0227.

Chopra, P.N., Paterson, M.S., 1984. The role of water in the deformation of dunite. J. Geophys. Res. 89, 7861–7876. http://dx.doi.org/10.1029/JB089iB09p07861.

Cordier, P., Demouchy, S., Beausir, B., Taupin, V., Barou, F., Fressengeas, C., 2014. Disclinations provide the missing mechanism for deforming olivine-rich rocks in the mantle. Nature 507, 51–56.

Crameri, F., Schmeling, H., Golabek, G. J., Duretz, T., Orendt, R., Buiter, S. J., May, D. A., Kaus, B. J., Gerya, T. V. and Tackley, P. J., 2012. A comparison of numerical surface topography calculations in geodynamic modelling: an evaluation of the 'sticky air' method. Geophysical Journal International 189, 38-54. doi:10.1111/j.1365-246X.2012.05388.x

Crameri, F., Tackley, P.J., 2015. Parameters controlling dynamically self consistent plate tectonics and single sided subduction in global models of mantle convection. J. Geophys. Res. Solid Earth 120, 3680–3706. doi: 10.1002/2014JB011664.

De Bresser, J., Ter Heege, J., Spiers, C., 2001. Grain size reduction by dynamic recrystallization : can it result in major rheological weakening ? Internat. Jour. Earh Sci. 91, 28-45.

Deer, W.A., Howie, R.A., Zussmann, J., 1997. Rock forming minerals: Orthosilicates. Vol. 1A

Geological Society of London, London, p.187.
Demouchy, S., Schneider, S.E., Mackwell, S.J., Zimmerman, M.E., Kohlstedt, D.L., 2009. Experimental deformation of olivine single crystals at lithospheric temperatures. Geophys. Res. Lett., 36. L04304. 10.1029/2008gl036611.
Demouchy, S., 2010. Diffusion of hydrogen in olivine grain boundaries and implications for the survival of water-rich zones in the Earth's mantle. Earth Planet. Sci. Lett. 295, 305–313. http://dx.doi.org/10.1016/j.epsl.2010.04.019.
Demouchy, S., Tommasi, A., Ballaran, T.B. & Cordier, P., 2013. Low strength of Earth's uppermost mantle inferred from tri-axial deformation experiments on dry olivine crystals. Phys. Earth Plan. Inter., 220, 37-49.
Demouchy, S., Mussi, A., Barou, F., Tommasi, A., Cordier, P., 2014. Viscoplasticity of polycrystalline olivine experimentally deformed at high pressure and 900°C. Tectonophysics 623, 123–135. http://dx.doi.org/10.1016/j.tecto.2014.03.022.
DePaola, N., Holdsworth, R. E., Viti, C., Collettini, C. & Bullock, R., 2015. Can grain size sensitive flow lubricate faults during the initial stages of earthquake propagation? Earth and Planetary Science Letters 43, 48-58.
Devereux, O.F., 1983. Topics in Metallurgical Thermodynamics. John Wiley & Sons, 494 pp.
Evans, B., Goetze, C., 1979. The temperature variation of hardness of olivine and its implication for polycrystalline yield stress. J. Geophys. Res. 84, 5505–5524.
Faul, U.H., Fitz Gerald, J.D., Farla, R.J.M., Ahlefeldt, R., Jackson, I., 2011. Dislocation creep of fine-grained olivine. J. Geophys. Res. 116, B01203. http://dx.doi.org/10.1029/2009JB007174.
Fischer, K.M, Ford, H.A., Abt, D.L., Rychert, C.A., 2010. The Lithosphere-Asthenosphere Boundary. Annual Review of Earth and Planetary Sciences 38:1, 551-575.
Frank, F.C., 1958. I. Liquid crystals. On the theory of liquid crystals. Discuss. Faraday Soc. 25, 19. http://dx.doi.org/10.1039/df9582500019.
Frey, F.A., Prinz, M., 1978. Ultramafic inclusions from san carlos, Arizona: petrologic and geochemical data bearing on their petrogenesis. Dev. Petrol. 5, 129–176. http://dx.doi.org/10.1016/B978-0-444-41658-2.50013-4.
Friedel, G., 1922. The mesomorphic states of matter. Ann. Phys. 18, 273–474. http://dx.doi.org/10.1201/9780203022658.ch1b.
Gay, P., Le Maitre, R.W., 1961. Some Observations on Iddingsite. American Mineralogist. 46 (1–2), pp. 92–111.
Gleason, G.C., Tullis, J., 1994. A Flow Law for Dislocation Creep of Quartz Aggregates Determined with the Molten-Salt Cell. Tectonophysics 247(1), 1-23.
Gueguen, Y., Nicolas, A., 1980. Deformation of mantle rocks. Annu. Rev. Earth Planet. Sci. 8, 119–144. http://dx.doi.org/10.1146/annurev.ea.08.050180.001003.
Hager, B.H., 1984. Subducted slabs and the geoid: Constraints on mantle rheology and flow. Journal of Geophysical Research: Solid Earth 89 (B7). https://doi.org/10.1029/JB089iB07p06003
Hansen, L.N., Zimmerman, M.E., Kohlstedt, D.L., 2011. Grain boundary sliding in San Carlos olivine: Flow law parameters and crystallographic - preferred orientation 116, 1–16. http://dx.doi.org/10.1029/2011JB008220.
Hansen, L.N., Zimmerman, M.E., Dillman, A.M., Kohlstedt, D.L., 2012. Strain localization in olivine aggregates at high temperature: A laboratory comparison of constant-strain-rate and constant-stress boundary conditions. Earth Planet. Sci. Lett. 333–334, 134–145. http://dx.doi.org/10.1016/j.epsl.2012.04.016.
Hirose, T., Shimamoto, T. (2005). Growth of molten zone as a mechanism of slip weakening of simulated faults in gabbro during frictional melting, J. Geophys. Res., 110, B05202, doi: 10.1029/2004JB003207.
Hirth, J.P., Lothe, J., 1982. Theory of dislocations. Krieger Publishing Company, 857 pp.

Hirth, G. & Kohlstedt, D.L., 2003. Rheology of the upper mantle and the mantle wedge: a view from the experimentalists. In J. Eiler, ed. Inside the Subduction Factory. Washington, DC: American Geophysical Union. pp.83-105.

Hirth, G., Kohlstedt, D.L., 2015. The stress dependence of olivine creep rate: Implications for extrapolation of lab data and interpretation of recrystallized grain size. Earth Planet. Sci. Lett. 418, 20-26.

Hutchinson, J.W., 1977. Creep and
plasticity of hexagonal polycrystals as related to single crystal slip. Metall. Trans. A 8, 1465–1469. http://dx.doi.org/10.1007/BF02642860.

Karato, S-I., 2012. On the origin of the asthenosphere. Earth and Planetary Science Letters 321–322, 95-103, ISSN 0012-821X, https://doi.org/ 10.1016/j.epsl.2012.01.001.

Kikuchi, S., 1928. Diffraction of Cathode Rays by Mica. Japanese Journal of Physics. 5, 83–96.

Keefner, J.W., Mackwell, S.J., Kohlstedt, D.L., Heidelbach, F., 2011. Dependence of dislocation creep of dunite on oxygen fugacity: Implications for viscosity variations in Earth's mantle. J. Geophys. Res. 116, 1–15. http://dx.doi.org/10.1029/2010JB007748.

Kittel, C., 1996. Introduction to Solid State Physics. 7th edition, John Wiley & Sons, Inc, pp 592–593.

Klein, C., Hurlburt, C.S., 1985. Manual of Mineralogy (21st ed.). New York: John Wiley & Sons. ISBN 0-471-80580-7.

Kohlstedt, D.L., Hansen, L.N., 2015. Constitutive equations, rheological behavior, and viscosity of rocks. Treatise on Geophysics, 2nd edition, vol 2., pp. 441-472.

Koizumi, S., Hiraga, T., Tachibana, C., Tasaka, M., Miyazaki, T., Kobayashi, T., Takamasa, A., Ohashi, N., Sano, S., 2010. Synthesis of highly dense and fine-grained aggregates of mantle composites by vacuum sintering of nano-sized mineral powders. Physics and Chemistry of Minerals, 37(8), 505–518. https://doi.org/10.1007/s00269-009-0350-y

Kronenberg, A.K., Kirby, S. H., Pinkston, J. C., 1990. Hydrolytic weakening and penetrative deformation within a natural shear zone. Geophysical Monograph 56, 21-36.

Ma, S., Shimamoto, T., Yao, L., Togo, T., & Kitajima, H., 2014. A rotary-shear low to high-velocity friction apparatus in Beijing to study rock friction at plate to seismic slip rates. Earthquake Science 27(5), 469–497. https://doi.org/10.1007/s11589-014-0097-5.

Mackwell, S.J., Kohlstedt, D.L., Paterson, M.S., 1985. The role of water in the deformation of olivine single crystals. J. Geophys. Res. 90, 11319. http://dx.doi.org/10.1029/JB090iB13p11319.

Mackwell, S.J., Kohlstedt, D.L., 1990. Diffusion of hydrogen in olivine: implications for water in the mantle. Journal of Geophysical Research 98 (B4), 5079-5088.

Mackwell, S.J., Zimmermann, M.E., Kohlstedt, D.L., 1998. High-temperature deformation of dry diabase with application to tectonics on Venus. Journal of Geophysical Research: Solid Earth 103 (B1), https://doi.org/10.1029/97JB02671.

Maerten, F., Madden, E. H., Pollard, D. D., & Maerten, L., 2016a. Incorporating fault mechanics into inversions of aftershock data for the regional remote stress, with application to the 1992 Landers, California earthquake. Tectonophysics 674, 52–64 https://doi.org/10.1016/j.tecto.2016.01.032.

Maerten, L., Maerten, F., Lejri, M., & Gillespie, P., 2016b. Geomechanical paleostress inversion using fracture data. Journal of Structural Geology 89, 197–213. https://doi.org/10.1016/j.jsg.2016.06.007

Maitland, T., Siltzman, S., 2007. Electron Backscatter Diffraction (EBSD) Technique and Materials Characterization Examples. in Zhou, W., Wang, Z.L., Scanning Microscopy for Nanotechnology: Techniques and Applications. Springer, 522 pp.

Mei, S., Kohlstedt, D., 2000. Influence of water on plastic deformation of olivine aggregates 1. Diffusion creep regime. J. Geophys. Res. 105, 21457–21469.

Mises, R. v., 1928. Mechanik der plastischen Formänderung von Kristallen. Zeitschrift Angew. Math. Mech. 8, 161–185.

Nakagawa, T., Tackley, P.J., 2015. Influence of plate tectonic mode on the coupled thermochemical evolution of Earth's mantle and core. Geochem. Geophys. Geosyst. 16, 3400–3413, doi: 10.1002/2015GC005996.

Nakamura, A., Schmalzried, H., 1983. On the nonstoichiometry and point defects of olivine. Physics and Chemistry of Minerals 10 (1), pp 27–37.

Nicolas, A., 1986. Structure and petrology of peridotites: Clues to their geodynamic environment. Rev. Geophys., 24, 875-895. http://dx.doi.org/10.1029/RG024i004p00875.

Nicolas, A., Poirier, J.P., 1976. Crystalline plasticity and solid-state flow in metamorphic rocks, selected topics in geological sciences series. London and New York, John Wiley & Sons, 976, p. 246.

Paterson, M.S., Olgaard, D.L., 2000. Rock deformation tests to large shear strains in torsion. Journal of Structural Geology 22(9), 1341-1358. DOI: 10.1016/S0191-8141(00)00042-0

Raterron, P., Wu, Y., Weidner, D.J., Chen, J. (2004). Low-temperature olivine rheology at high pressure. Phys. Earth Planet. Inter. 145, 149–159.

Reiner M., 1964. The Deborah number. Phys. Today, 62.

Ross, S., 1925. The Origin, Occurrence, Composition and Physical Properties of the Mineral Iddingsite. Proc. U.S. Nat., Mus. 67.

Sanosh, K.P., Chu, M-C., Balakrishnan, A., Kim, T.N., Cho, S-J., 2010. Pressureless sintering of nanocrystalline hydroxyapatite at different temperatures. Metals and Materials Internat. 16 (4), 605-611.

Schmalzried, H, 1981. Solid State Reactions. 2nd edn, Weinheim: Verlag Chemie, 254 pp.

Shannon, R.D., 1976. Revised effective ionic radii and systematic studies of interatomic distances in halides and chalcogenides. Acta Crystallogr. A. 32, 751–767. Bibcode:1976AcCrA ..32..751S. doi:10.1107/S0567739476001551.

Sharple, P.P., 1914. The Relation between the Melting Point and the Viscosity of Refined Tars. Ind. Eng. Chem. 6 :4, pp 285–286, DOI: 10.1021/ie50064a006.

Sills, R.B., William, P., Kuykendall, P., Aghaei, A., Cai, W., 2016. Fundamentals of Dislocation Dynamics Simulations. in: Weinberger, C.R. Tucker, G.J. (eds.), Multiscale Materials Modeling for Nanomechanics, Springer Series in Materials Science 245, DOI 10.1007/978-3-319-33480-6_2

Spray, J.G., 1987. Artificial generation of pseudotachylyte using friction welding apparatus: Simulation of melting on a fault plane. J. Struct. Geol. 9, 49–60, doi:10.1016/0191-8141(87)90043-5.

Spray, J.G., 1992. A physical basis for the frictional melting of some rockforming minerals, Tectonophysics, 204, 205 – 221, doi:10.1016/0040-1951(92)90308-S.

Spray, J.G., 1995. Pseudotachylyte controversy: Fact or friction? Geology, 23, 1119 – 1122, doi:10.1130/0091-7613

Spray, J.G., 2005. Evidence for melt lubrication during large earthquakes, Geophys. Res. Lett., 32, L07301, doi:10.1029/2004GL022293.

Sykes, D., Rossman, G.R., Veblen, D.R., Grew, E.S., 1994. Enhanced H and F incorporation in borian olivine. American Mineralogist 79, 904–908.

Taylor, G.I., 1934. The Mechanism of Plastic Deformation of Crystals. Part I. Theoretical. Proceedings of the Royal Society of London Series A. 145 (855), 362–87. Bibcode:1934RSPSA.145.362T. doi:10.1098/rspa.1934.0106. JSTOR 2935509.

Thatcher, W., 1983. Nonlinear strain buildup and the earthquake cycle on the San Andreas fault. J. Geophys. Res. 88:5893–902.

Tielke, J.A., Zimmerman, M.E., Kohlstedt, D.L., 2016. Direct shear of olivine single crystals.

Earth Planet. Sci. Lett. 455, 140–148.
Tommasi, A., Tikoff, B., Vauchez, A., 1999. Upper mantle tectonics: Three-dimensional deformation, olivine crystallographic fabrics and seismic properties. Earth Planet. Sci. Lett. 168, 173–186. http://dx.doi.org/10.1016/S0012-821X(99)00046-1.
Tommasi, A., Baptiste, V., Vauchez, A., Holtzman, B., 2016. Deformation, annealing, reactive melt percolation, and seismic anisotropy in the lithospheric mantle beneath the southeastern Ethiopian rift: Constraints from mantle xenoliths from Mega. Tectonophysics 682, 186–205. http://dx.doi.org/10.1016/j.tecto.2016.05.027.
Tse, S.T., Rice, J.R., 1986. Crustal earthquake instability in relation to the depth variation of frictional slip properties. J. Geophys. Res. 91:9452–72.
Tullis, J., Yund, R.A., 1985. Dynamic recrystallization of feldspar: A mechanism for ductile shear zone formation. Geology 13 (4), 238-241. https://doi.org/10.1130/0091-7613
Zoback, M. L., et al. (1989). Global patterns of tectonic stress. Nature 341, 291– 298.

Annex A - Co-authorship of an article originally published in The American Ceramic Society in 2018, doi: https://doi.org/10.1111/jace.15588. Due to copyright issues, a reshaped version of the abstract is resented (copy available at hal.archives-ouvertes.fr).

Effect of pressure and temperature on viscosity of N-BK7 glass

Linfeng Ding[1]*, Manuel Thieme[2], Sylvie Demouchy[2], Clemens Kunisch[3], Boris J.P. Kaus[1]

[1]Institute of Geosciences, Johannes Gutenberg University, 55128 Mainz, Germany
[2]Geosciences Montpellier, Université de Montpellier & CNRS, 34095 Montpellier, France
[3]Schott AG, Corporate Research & Development, 55122 Mainz, Germany
Corresponding author: dingli@uni-mainz.de

Abstract

We experimentally quantified the effect of pressure and temperature on the viscosity of SCHOTT N-BK7® glass, by performing *in situ* deformation experiments at temperatures between 550 and 595 °C and a confining pressure between 100 MPa and 300 MPa. Experiments were performed at constant displacement rates to produce almost constant strain rates between 9.70×10^{-6} s^{-1} and 4.98×10^{-5} s^{-1}. The resulting net axial stresses range from 81 MPa to 802 MPa and the finite strains range from 1.4 % to 8.9 %. The mechanical results show that the SCHOTT N-BK7® glass is viscoelastic near the glass transition temperature at 300 MPa of confining pressure. In order to elucidate the data, we incorporated both 1-element and 2-element generalized Maxwell viscoelastic models in an inversion approach, for which we provide MATLAB scrips. Results show that the 2-element Maxwell model fits the experimental data well. The stress decreases with increasing temperature at 300 MPa and the temperature dependence yields a similar activation energy (601±10 $kJ \cdot mol^{-1}$ or $\Delta H/R = 7.2 \times 10^4$ K) to a previously reported value at 1-atm (615 $kJ \cdot mol^{-1}$ or $\Delta H/R = 7.4 \times 10^4$ K). The SCHOTT N-BK7® glass shows a limited linear increase of viscosity with increasing pressure of ~0.1 $\log_{10}(Pa \cdot s)$/100 MPa, which is in agreement with the most recent two-internal-parameter relaxation model (which is also based on experiments).

Key words: Borosilicate glass; high pressure; high temperature; deformation experiment; viscosity; Maxwell model.

Cite as follow: Ding, L., Thieme, M., Demouchy, S., Kunisch, C., Kaus, B. (2018) Effect of pressure and temperature on viscosity of N-BK7 glass. Journal of the American Ceramic Society, doi: 10.1111/jace.15588.

Notes

Notes

Notes

Notes

Summary / Résumé

Convection in Earth's mantle is the major driving force behind the movement of tectonic plates. While the lower parts of the upper mantle deform in a ductile way, the plates themselves are rheologically more rigid than the asthenosphere beneath. To understand how convection yields tectonic plates, it is vital to quantify the viscous and frictional strength of the lithospheric mantle. Yet to date, the rheology of the uppermost mantle just below the Mohorovicic discontinuity is still poorly understood. Furthermore, the early stages of visco-plastic deformation at intermediate temperatures (600 – 1000 °C) relevant to the lithospheric mantle are not well documented or quantified. To provide accurate mechanical values for the lithospheric mantle, we need mechanical data but also a characterization of the associated microstructure to understand the deformation mechanisms at play during permanent deformation of olivine-rich rocks. In this thesis, I have performed deformation experiments in axial compression using a Paterson press (at Géosciences Montpellier, University of Montpellier, France) at high pressure and temperature (300 MPa, 1000 – 1200 °C) and in torsion using a low to high velocity rotary shear frictional testing machine (Rock Mechanics Laboratory, Durham University, UK) at room pressure and temperatures. The recovered samples were characterized using scanning electron microscopy, electron backscatter diffraction and transmission electron microscopy. After an introduction chapter where the state-of-the-art is detailed, and a chapter focusing on experimental and analytical methods used during scientific projects, the thesis is organized as three subsequent chapters, each of them corresponding to three scientific articles: one is published (1) Stress evolution and associated microstructure during transient creep of olivine at 1000-1200 °C (Phys. Earth Planet. Int., doi: 10.1016/j.pepi.2018.03.002.); and the two others are in preparation, (2) Disclination density in polycrystalline olivine experimentally deformed at 1000 °C and 1200 °C; and (3) Shear deformation of nano- and micro-crystalline olivine at seismic slip rates. Chapter III has shown that the observed mechanical hardening can not come from a simple increase in dislocation density (e.g., entanglement) and that other mechanisms must be at play to compensate for the limitations of dislocation slip. For the first time, in chapter IV the densities of geometrically necessary dislocations (GND, translational defects) and disclinations (rotational defects) are quantified on a series of rocks deformed at different temperatures, finite strains and stress levels. No correlation has been identified between disclination density and stress, strain or GND. The role of the disclinations will therefore be limited to migration at grain boundaries, which may be sufficient to unblock dislocations in the polycrystalline olivine aggregate. In chapter V, torsion experiments confirmed the negligible effect of grain size (olivine from 0.07 to 70 μm) on the drastic decrease of the coefficient of friction, but the characterization of the samples did permit to shed light on the main mechanism of deformation. Thanks to an experimental approach and up-to-date material characterization, this thesis permitted better characterization of the brittle-ductile transition of a fine-grained dunite-type rock subjected to permanent deformation at uppermost mantle temperatures.

La convection dans le manteau terrestre est la principale force motrice du mouvement des plaques tectoniques. Alors que les parties inférieures du manteau supérieur se déforment de manière ductile, les plaques tectoniques sont rhéologiquement plus rigides que l'asthénosphère sous-jacente. Pour comprendre le couplage entre la convection profonde et les plaques tectoniques à la surface de la Terre, il est essentiel de comprendre les mécanismes de déformation visqueuse et frictionnelle du manteau lithosphérique. Mais à ce jour, la rhéologie du manteau supérieur juste au-dessous de la discontinuité de Mohorovicic est encore mal comprise. De plus, les premiers stades de la déformation viscoplastique à des températures intermédiaires (600-1000 ° C) pertinentes pour le manteau lithosphérique, ne sont ni bien documentés ni quantifiés. Pour fournir des valeurs mécaniques précises pour le manteau lithosphérique, nous avons besoin de données mécaniques mais aussi de la caractérisation de la microstructure associée pour comprendre la physique des mécanismes en jeu lors de la déformation permanente des roches riches en olivine. Dans cette thèse, nous avons réalisé des expériences de déformation en compression axiale à l'aide d'une presse Paterson (Géosciences Montpellier, Université de Montpellier, France) à haute pression et température (300 MPa, 1000-12000 ° C) et en torsion ('rotary shear frictional testing machine' au laboratoire de mécanique des roches, université de Durham, Royaume-Uni) à pression et température ambiantes. Les échantillons ont été caractérisés par microscopie électronique à balayage, diffraction d' d'électrons rétrodiffusés et microscopie électronique en transmission. Après un chapitre d'introduction où l'état de l'art est détaillé et un chapitre consacré aux méthodes expérimentales et analytiques utilisées dans les projets scientifiques, la thèse s'organise en trois chapitres, chacun correspondant à trois articles scientifiques: le premier est publié (1) Évolution de la contrainte et des microstructures associées au fluage transitoire de l'olivine à 1000-1200 °C (Phys. Earth Planet. Int., doi: 10.1016/ j.pepi.2018.03.002. (https: //hal.archives- ouvertes.fr/hal-01746122) et les deux autres sont en préparation, (2) Densité de disclinaisons dans l'olivine polycristalline déformée expérimentalement à 1000 ° C et 1200 ° C (3) Déformation par cisaillement de l'olivine nano- et micro-cristalline. Le premier projet du chapitre III a montré que le durcissement mécanique observé ne peut pas provenir d'une simple augmentation de la densité de dislocations (e.g., la forêt) et que d'autres mécanismes doivent être mis en œuvre pour compenser les limites de glissements des dislocations. Dans le chapitre IV, les densités de dislocation géométriquement nécessaires (GND, défauts de translation) et les disclinaisons (défauts de rotation) sont quantifiées sur une série de roches déformées à différentes températures, déformations finies et niveaux de contrainte, mais aucune corrélation n'a été identifiée entre la densité de disclinaisons, et la contrainte, la déformation finie, ou la densité de GND. Le rôle des disclinaisons serait donc limité à la migration aux joints de grains, ce qui peut être suffisant pour débloquer les dislocations dans l'agrégat d'olivine polycristalline. Au chapitre V, les expériences de torsion ont confirmé l'effet négligeable de la taille du grain (olivine de 0,7 à 70 μm) sur la diminution drastique du coefficient de frottement, mais la caractérisation des échantillons n'a pas permis d'élucider le mécanisme principal de déformation. Cette thèse a permis de mieux caractériser la transition fragile-ductile d'une roche de type dunite à grains fins soumise à une déformation permanente aux températures du manteau sommitale.